



<https://theses.gla.ac.uk/>

Theses Digitisation:

<https://www.gla.ac.uk/myglasgow/research/enlighten/theses/digitisation/>

This is a digitised version of the original print thesis.

Copyright and moral rights for this work are retained by the author

A copy can be downloaded for personal non-commercial research or study,
without prior permission or charge

This work cannot be reproduced or quoted extensively from without first
obtaining permission in writing from the author

The content must not be changed in any way or sold commercially in any
format or medium without the formal permission of the author

When referring to this work, full bibliographic details including the author,
title, awarding institution and date of the thesis must be given

Enlighten: Theses

<https://theses.gla.ac.uk/>
research-enlighten@glasgow.ac.uk

**A LITHIUM NIOBATE
INTEGRATED OPTICAL
MODULATOR WITH A
NON-COPLANAR ELECTRODE
GEOMETRY.**

A Thesis
Submitted To The
Faculty Of Engineering
Of The University Of Glasgow
By
Scott M^cMeekin, MSc, BSc.

© Scott M^cMeekin (August 1989)

ProQuest Number: 10999280

All rights reserved

INFORMATION TO ALL USERS

The quality of this reproduction is dependent upon the quality of the copy submitted.

In the unlikely event that the author did not send a complete manuscript and there are missing pages, these will be noted. Also, if material had to be removed, a note will indicate the deletion.



ProQuest 10999280

Published by ProQuest LLC (2018). Copyright of the Dissertation is held by the Author.

All rights reserved.

This work is protected against unauthorized copying under Title 17, United States Code
Microform Edition © ProQuest LLC.

ProQuest LLC.
789 East Eisenhower Parkway
P.O. Box 1346
Ann Arbor, MI 48106 – 1346

INDEX

Chapter/Section.	Page.
<u>Thesis Outline</u>	1
<u>Chapter 1: Introduction.</u>	3
1.1 The crystal structure of lithium niobate	3
1.2 The electrooptic effect	7
1.3 Electrooptic devices fabricated in lithium niobate	10
1.3.1 The phase modulator	11
1.3.2 Intensity modulators	14
1.3.3 Polarisation matching devices and polarisation independent modulators	16
1.3.4 Lumped, standing- and travelling-wave electrodes.	18
1.4 Measurement of the electrooptic coefficients by means of the transverse electrooptic phase modulator	23
<u>References.</u>	25
<u>Chapter 2: Waveguide fabrication techniques.</u>	30
2.1 Out-diffusion	30
2.2 The titanium-indiffusion process	31
2.3 The proton-exchange process	39
<u>References.</u>	47

<u>Chapter 3.:Fabrication of the transverse electrooptic modulator</u>	53
3.1 Introduction	53
3.2 Waveguide fabrication	55
3.2.1 The fabrication of titanium indiffused guides	55
3.2.2 The fabrication of proton-exchanged guides	60
3.3 Buffer layer	63
3.4 Lower electrode fabrication	67
3.5 Supporting substrate	73
3.6 Substrate bonding	75
3.7 Edge polishing	77
3.8 Thinning	82
3.9 Contact to the lower electrodes	86
3.10 Top electrode	90
3.11 Device mounting	90
<u>References.</u>	93
<u>Chapter 4.:Theoretical modelling of the transverse electrooptic modulator</u>	94
4.1 Comparison of transmission line properties	94
4.1.1 Transmission line properties of transverse electrodes	94
4.1.2 Derivation for wide strips	101
4.1.3 Derivation for narrow strips	103
4.1.4 Transmission line properties of co-planar strip lines	105
4.1.5 Summary	107

4.2 Comparison of operating voltage and figure of merit	108
4.3 Comparison of bandwidth, figure of merit and microwave properties	114
4.3.1 Bandwidth	114
4.3.2 Figure of merit	118
4.3.3 Microwave properties	119
<u>References.</u>	120
<u>Chapter 5.:Experimental evaluation of the transverse electrooptic modulator</u>	121
5.1 Electrode capacitance and modulator bandwidth	121
5.2 Measurement of the operating voltage and electrooptic coefficients	124
5.2.1 Measurements using a Mach-Zehnder interferometer	124
5.2.2 Measurement using a heterodyne detection system	128
5.3 Results obtained using guides fabricated by titanium-indiffusion	133
5.4 Measurement of the R_{33} electrooptic coefficient in proton-exchanged waveguides	136
5.5 Evaluation of the photorefractive effect in proton-exchanged waveguides	137
5.5.1 Index instabilities in proton-exchanged guides and the mechanics of the photorefractive effect	137
5.5.2 Instabilities in proton-exchanged waveguides observed using a transverse electrooptic phase modulator	141
<u>References.</u>	147
<u>Chapter 6.:Summary, conclusions and future work.</u>	149

6.1 Summary	149
6.2 Conclusions	152
6.3 Future work	154
<u>References.</u>	158
<u>Appendix A. Evaluation of the transmission line properties of strips separated by a dielectric sheet by the use of conformal mapping</u>	159
A-1 Conformal mapping techniques	159
A-2 Wide strip derivation	164
A-3 Narrow strip derivation	171
<u>References.</u>	174
<u>Publications.</u>	175

Dedicated to Susan.

ACKNOWLEDGEMENTS.

I am extremely grateful to Professor John Lamb for the encouragement and support he has given me over the last three years and for the use of the facilities in the Department of Electrical and Electronic Engineering.

I would like to express my extreme gratitude to my academic supervisor and friend Professor Richard De La Rue for his extremely valuable help, encouragement and many useful discussions. I am greatly indebted to Max Robertson whose assistance far exceeded that required as my industrial supervisor at Logitech Ltd. A great deal of the credit for the completion of the Thesis must be attributed to both supervisors.

Special thanks go to Walter Johnston for supervision at Logitech Ltd. at the start of the work and his initial suggestion upon which the bulk of the work conducted in the Thesis is based.

The help and assistance of the members of the Mechanical and Electronic Workshops is gratefully appreciated. Many thanks go to Kas Piechowiak for his expert technical help, perseverance and advice in the polishing laboratory at Glasgow University. Special thanks also go to Robert Harkins, Lois Hobbs, Harry Anderson, George Boyle, Jimmy Young and Dave Clifton.

I would like to express my thanks to Gordon Graham of Logitech Ltd. for familiarising me with the techniques used in the lapping and polishing of crystals and for many useful discussions concerning the thinning process.

I would also like to express my gratitude to Israr Chaudry for the provision of and advice on computing facilities enabling the Thesis to be written with ease and comfort.

I would like to extend my gratitude to all my colleagues who made my stay at Glasgow University enjoyable.

Logitech Ltd. are to be thanked for both their financial support over the last three years and the provision of their polishing expertise and equipment.

Thesis Outline.

The object of this thesis is to establish a fabrication procedure for a novel electrode structure for use in conjunction with an electrooptic phase modulator and to evaluate the benefits achieved over standard electrode structures.

Chapter 1 gives a brief introduction to the properties of lithium niobate and, in particular, their relation to the electrooptic effect. An introduction is given to the novel electrode structure, termed transverse electrodes, where the electrodes are on opposite faces of the lithium niobate substrate and straddle the waveguide. A review of several devices fabricated on lithium niobate is given and the advantages that may be achieved by using transverse electrodes are described. An additional advantage of the transverse electrode structure to estimate accurately the electrooptic coefficients of waveguides is discussed.

Chapter 2 reviews several techniques that have been employed to fabricate strip waveguides in bulk lithium niobate. Special attention is paid to the titanium-indiffusion technique and the more novel technique of proton-exchange. The properties of waveguides fabricated using a novel proton-exchange technique will be investigated using the transverse electrode structure.

Chapter 3 is concerned with the development of a technique which enables a lithium niobate substrate to be thinned successfully to less than 20 μm with electrodes on opposite faces of the substrate. The need for a supporting substrate, during and after thinning is discussed and the problems in achieving a satisfactory bond between the lithium niobate and the glass substrate are described. The edges of the lithium niobate substrate are polished prior to substrate thinning enabling light to be coupled into the guide by an end-fire rig. A description is given of the stages involved in thinning the substrate to the desired thickness and the subsequent polishing of the substrate to remove surface damage. A method is described by which contact to the lower electrode, positioned between the lithium niobate substrate and the glass substrate with no point of exposure, was made by means of a via hole.

Chapter 4 describes the use of a conformal mapping technique to establish a relationship between the physical properties of the transverse electrodes and their transmission line properties. A comparison is made with the

transmission line properties of co-planar electrodes along with a description of the advantages gained in relation to the operating voltage and the figure of merit.

Chapter 5 presents the electrooptic coefficients of waveguides fabricated by titanium-indiffusion and measured at 0.633 μm and 1.15 μm using a Mach-Zehnder interferometer and at 0.633 μm using an heterodyne system. The electrooptic coefficients of guides fabricated by proton-exchange were measured at 0.633 μm using both the Mach-Zehnder interferometer and the heterodyne system. An unexpected degree of optical damage was monitored in the waveguides fabricated by proton-exchange, a technique normally associated with a low degree of optical damage, and a possible explanation for this is given.

Finally, in chapter 6, a summary of the thesis is presented, and suggestions for future work are given.

Chapter 1.

Introduction.

One of the major areas of research for establishing an optical communication or optical signal processing system has centred on the electrooptic interaction between a guided optical field and an applied electrical field. Much of the research into waveguide electrooptic modulators has concentrated on two particular types of electrooptic material, III-V semiconductors and certain ferroelectrics, in particular lithium niobate and lithium tantalate. Of these, perhaps the most important material in the development of the electrooptic interaction in waveguide devices to date has been lithium niobate, due to its high electrooptic coefficients and the relative ease of fabrication of low loss waveguides. It is on lithium niobate that the review of previously published work and the novel work contained in this thesis are concentrated. It has been possible to fabricate low-loss waveguides on lithium niobate using a variety of techniques, of which titanium-indiffusion and proton-exchange appear to be the most popular, and these techniques will be examined in the following chapter.

There have been numerous types of electrooptic device fabricated on lithium niobate, from simple phase modulators to multiplexers and demultiplexers, from directional couplers to analogue-to-digital converters. One important common feature of virtually all these devices is the use of electrodes mounted on the same face of the lithium niobate substrate to apply the electric field. A brief review of some of these devices will be made in this chapter, with the aim of outlining the main paths taken in the development of electrooptic devices.

Before introducing the topic of devices fabricated on lithium niobate, a brief explanation will be given of the crystal structure of lithium niobate, together with a brief review of the electrooptic effect.

1.1 The crystal structure of lithium niobate.

Lithium niobate is a man-made compound that does not occur naturally. The growth of lithium niobate by the Czochralski technique, see Fig. 1.1 was reported independently by Ballman¹ and Fedulov² in 1964 and since then this

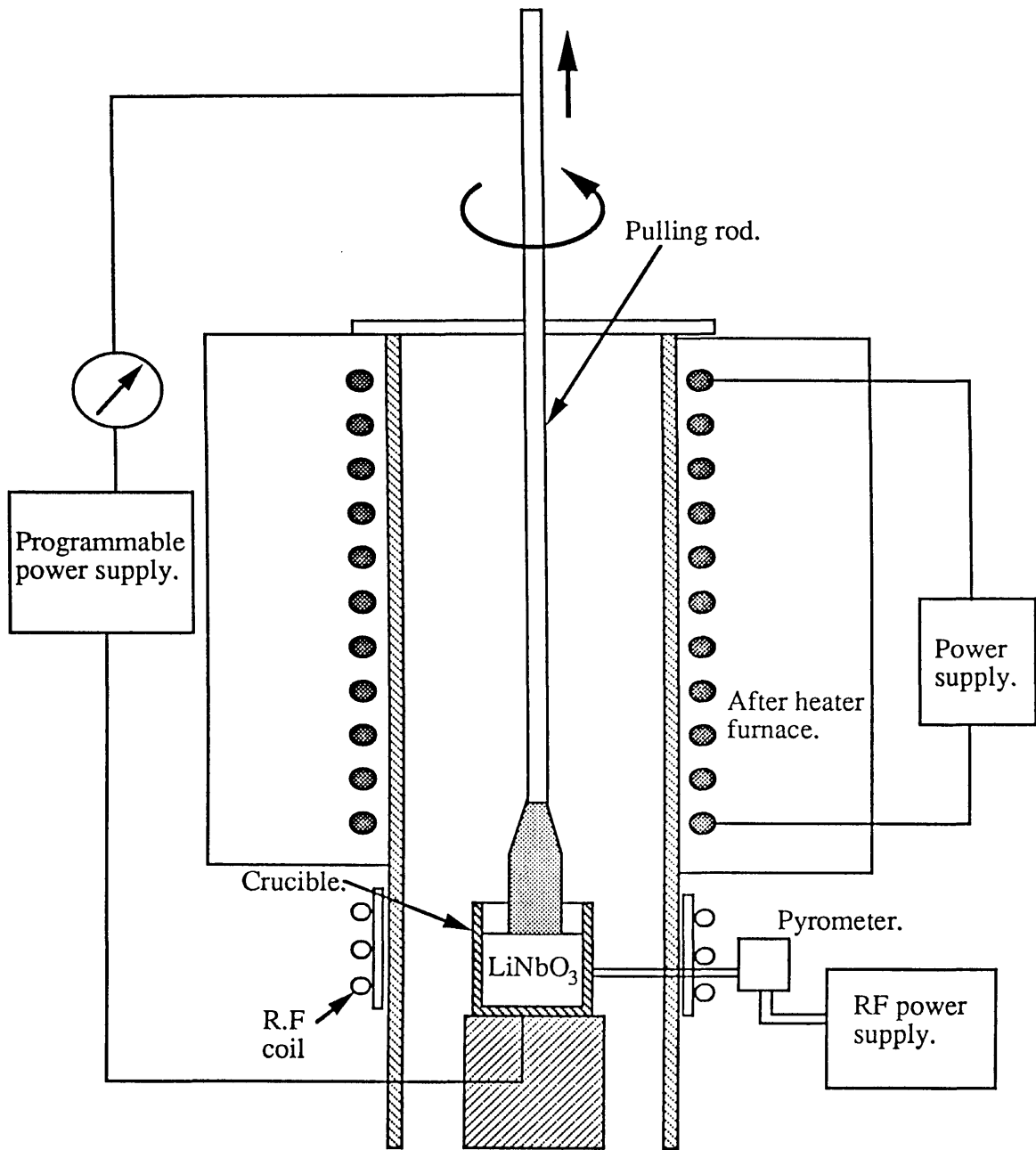


Figure 1.1. Growth of lithium niobate by the Czochralski technique.

technique has become the standard method for the commercial growth of lithium niobate. It is ferroelectric, with the trigonal crystal structure depicted in Fig. 1.2. It has a Curie temperature of 1140 °C, above which it transforms to a paraelectric phase. Below the Curie temperature the crystal structure consists, in part, of oxygen planes in a distorted hexagonal closed packed configuration. The octahedral interstices formed are one third filled by lithium atoms, one third filled by niobium ions and one third vacant¹⁴. In its paraelectric phase the lithium ions lie in the oxygen plane and the niobium ions lie centred between two oxygen planes as shown in Fig. 1.2 (a). Below the Curie temperature, in its ferroelectric phase both the lithium and niobium ions are displaced along the c-axis (see Fig. 1.2(b)) in either the positive or negative direction, forming multi-domains. To obtain single-domain material a lithium niobate crystal or boule section is poled with a strong D.C field along the c-axis¹⁵. The poling can be performed either during or after the growth of the lithium niobate boule. For poling during growth, the boule is maintained above 1000 °C by use of an after-heater after being pulled from the melt whilst a constant current of 2 mA.cm⁻² is passed through the lithium niobate boule. Alternatively the boule can be poled after growth by coating the c-faces with platinum paste electrodes. If the boule is not z-axis grown, flats have to be cut perpendicular to the z-axis to apply the electrodes. The boule is then heated to above the curie temperature and a constant current of approximately 2 mA.cm⁻² is passed through the boule for 30 to 60 minutes. Whilst the current is being passed the boule is slowly cooled to below the Curie temperature.

Lithium niobate possesses a three-fold rotational symmetry about the c-axis, making it a member of the trigonal crystal system. It also has mirror symmetry about three planes 60° apart rotating about the c-axis and is thus classified as a member of the $3m$ point group. Crystals which belong to the trigonal group can be structurally classified using either a hexagonal or a rhombohedral unit cell.

A full understanding of the physical processes occurring during the fabrication of waveguides in lithium niobate requires an accurate knowledge of the exact crystal structure and stoichiometry. Lithium niobate has been shown to have a large deviation in the stoichiometry dependent upon the growth conditions. The dependence of the stoichiometry upon the crystal growth conditions has been well studied by many workers^{3,4} as has the dependence of the optical and other properties upon the stoichiometry. An accurate method of

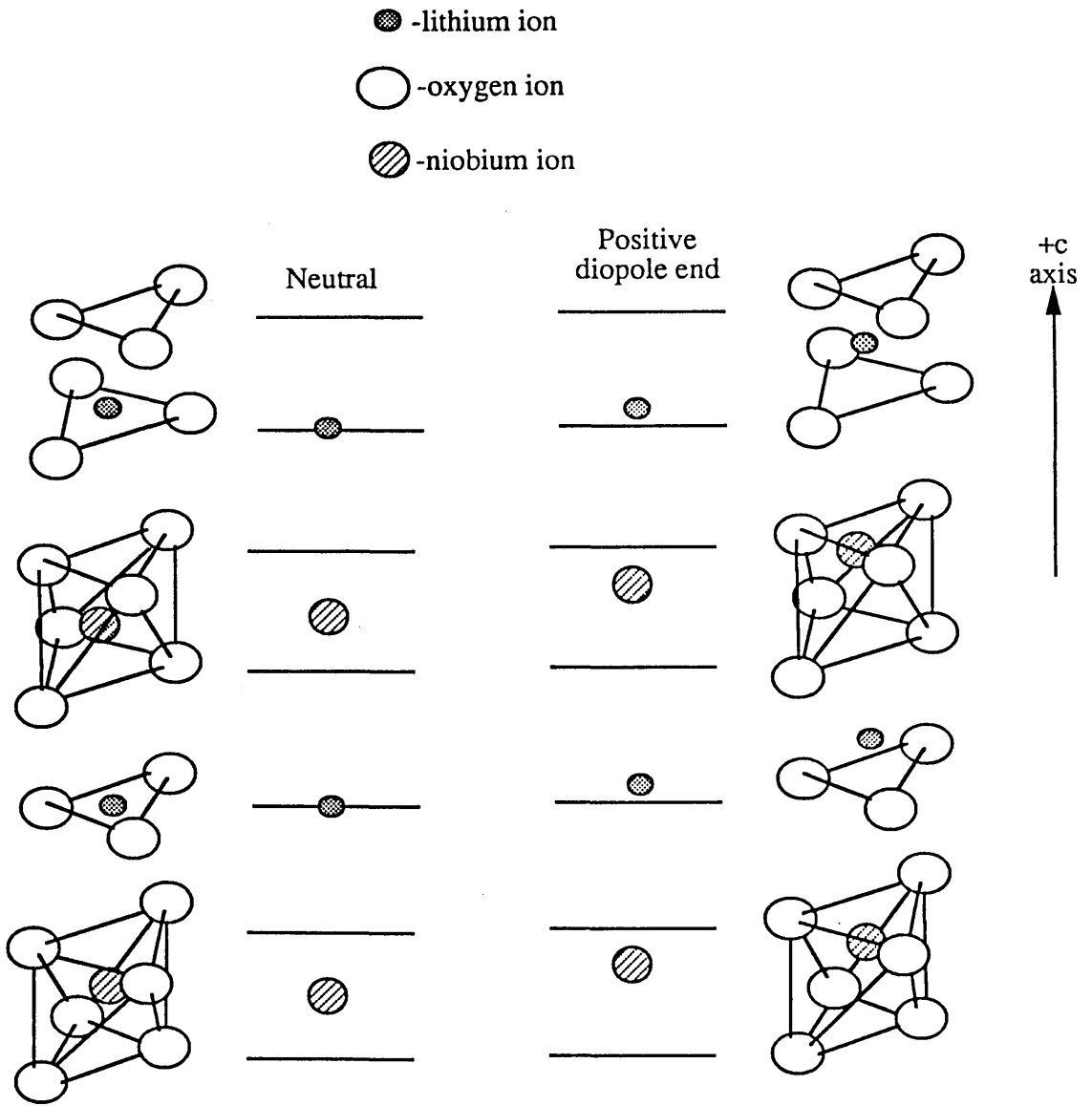


Figure 1.2(a) The paraelectric phase of lithium niobate as exists above the curie temperature of 1140 °C.

Figure 1.2(b) The ferroelectric phase of lithium niobate as exists below the curie temperature of 1140 °C.

determining the stoichiometry of the crystal is to measure the Curie temperature^{5,6}, which is strongly dependent upon the crystal composition. The birefringence is also strongly dependent upon the crystal composition^{5,6,7} whilst the electrooptic effect shows little variation and only the extra-ordinary refractive index is dependent upon the stoichiometry with the ordinary index showing much less variation⁸. The congruent melting composition is 48.6 mole% LiO₂.

For an in-depth study of the lithium niobate crystal structure a series of five papers by Nassau, Abrahams et al^{9,10,11,12,13} concerned with the growth, crystal structure and other material aspects published in 1966 are considered as an important piece of basic research. More up to date general reviews of the structure and properties of lithium niobate have been published by Weis and Rauber^{14,15}.

1.2 The electrooptic effect.

The electrooptic effect is a measure of the change in the permittivity of a crystal for a given applied bias field. This change in the permittivity can be explained by examining the relationship between the electric field strength E , the electric flux density D , and the permittivity ϵ . D can be expressed as a function of E by¹⁶

$$D = \epsilon^0 E + \alpha E^2 + \beta E^3 + \dots \quad (1.2.1)$$

where ϵ^0 , α and β are constants. The use of a scalar representation for the electric field helps to identify the important relationships between the electric field strength and the permittivity. The permittivity of the crystal is defined as the change in flux density for a given change in field strength and may be expressed as

$$\epsilon = dD/dE = \epsilon^0 + 2\alpha E + 3\beta E^2 + \dots \quad (1.2.2)$$

Similarly the refractive index, equal to the square root of ϵ/ϵ_0 , of any crystal in the presence of an electric field is described by:

$$n = n^0 + aE_0 + bE_0^2 + \dots \quad (1.2.3)$$

where n^0 is the refractive index in the absence of an applied field, E_0 is the applied field and a and b are constants relating an index change to the applied electric field. If the polarity of the electric field is reversed Eq. (1.2.3) becomes

$$n = n^0 - aE_0 + bE_0^2 - \dots \dots \quad (1.2.4)$$

If the crystal possesses a centre of symmetry, the change in the refractive index should be equal for either field orientation, implying $a=0$. If the crystal lacks a centre of symmetry, the refractive index change is dependent upon the sign of the applied electric field and $a \neq 0$. Hence, to have a linear electrooptic effect the crystal must lack a centre of symmetry.

The first order electrooptic effect or Pockels effect is described by

$$\Delta B_{ij} = \sum_{k=1}^3 R_{ijk} E_k, \quad i, j, k = 1, 2 \text{ or } 3 \quad (1.2.5)$$

where i, j and k describe the crystal axis, B is the dielectric impermeability and R_{ijk} is a third rank tensor describing the change in the permittivity of the crystal for an applied electric field along the k axis. R_{ijk} , being a third rank tensor, is described by a $3 \times 3 \times 3$ matrix with 27 coefficients. For example R_{123} implies a change in permittivity along the 1 and 2 axes for an applied field along the 3 axis. Fortunately it is possible to make use of the symmetry of the permittivity

$$\Delta \frac{\epsilon_0}{\epsilon_{ji}} = \Delta \frac{\epsilon_0}{\epsilon_{ij}} = \Delta B_{ij} = \Delta B_{ji} = \Delta B_m, \quad m = 1 \dots 6 \quad (1.2.6)$$

where $11=1, 22=2, 33=3, 23=32=4, 13=31=5, 12=21=6$.

which enables the replacement of the third rank tensor by a reduced tensor representation.

$$\Delta B_m = \sum_{k=1}^3 R_{mk} E_k \quad (1.2.7)$$

This can be rewritten as:

$$\begin{pmatrix} \Delta B_1 \\ \Delta B_2 \\ \Delta B_3 \\ \Delta B_4 \\ \Delta B_5 \\ \Delta B_6 \end{pmatrix} = \begin{pmatrix} R_{11} & R_{12} & R_{13} \\ R_{21} & R_{22} & R_{23} \\ R_{31} & R_{32} & R_{33} \\ R_{41} & R_{42} & R_{43} \\ R_{51} & R_{52} & R_{53} \\ R_{61} & R_{62} & R_{63} \end{pmatrix} \cdot \begin{pmatrix} E_1 \\ E_2 \\ E_3 \end{pmatrix} \quad (1.2.8)$$

Since there will be no electrooptic effect if the crystal possesses a centre of symmetry in the direction of the applied field, some of the components of the electrooptic tensor will be equal to zero or equal in magnitude to other coefficients of the tensor depending on the symmetry class of the crystal. For example for a crystal with 3m symmetry, i.e lithium niobate, the matrix is reduced to

$$\begin{pmatrix} 0 & -R_{22} & R_{13} \\ 0 & R_{22} & R_{13} \\ 0 & 0 & R_{33} \\ 0 & R_{42} & 0 \\ R_{42} & 0 & 0 \\ -R_{22} & 0 & 0 \end{pmatrix} \quad (1.2.9)$$

Expressing the electrooptic effect in this way shows that only particular combinations of applied field will result in the desired change in the refractive index.

Rewriting Eq. (1.2.7) in reduced tensor notation and simplifying to a non-rigorous scalar representation gives

$$\Delta \frac{1}{n^2} = R_{mk} E_k = -2 \frac{\Delta n}{n_{o,e}^3} \quad (1.2.10)$$

therefore

$$\Delta n = -\frac{1}{2} R_{mk} n_{o,e}^3 E_k \quad (1.2.11)$$

where $n_{o,e}$ is the appropriate ordinary or extraordinary refractive index.

This implies a change in the refractive index, Δn , for an applied electric field parallel to the k axis. The corresponding phase change for light propagating through the crystal is equal to :

$$\Delta\phi = \frac{2L\pi\Delta n}{\lambda} = - \frac{L\pi R_{mk} n_{o,e}^3 E_k}{\lambda} \quad (1.2.12)$$

where L is the interaction length and λ is the wavelength of the light.

Although the main interest for this thesis lies in the electrooptic effect it is impossible to consider the net effect without briefly taking the photoelastic effect into account. The photoelastic effect describes the change in the refractive index for an applied stress to the crystal structure. If the crystal is free, an applied static field will produce a strain in the crystal through the piezoelectric effect, which will in turn produce a change in the refractive index via the photoelastic effect. The resulting electrooptic effect is therefore a combination of the electrooptic and photoelastic effects. For an applied field at high frequencies the crystal strains are very small and only the primary electrooptic effect is observed. Two different sets of values for the electrooptic coefficients are therefore involved and the appropriate set of values chosen depend on the operating frequency of the applied voltage.

To summarise: by applying an electric field to a crystal which lacks a centre of symmetry there will be a resulting change in the refractive index as defined by Eq. (1.2.7). The particular terms which contribute to the change depend solely on the symmetry class of the crystal.

1.3 Electrooptic devices fabricated in lithium niobate.

The objective of the work contained in this thesis was to examine an alternative electrode structure to the “standard” co-planar electrode structure employed in the modulators described below. The term “co-planar electrodes” refers to an electrode structure where all electrodes are in the same plane; namely, on the top surface of the dielectric substrate, while “co-planar modulator” refers to an electrooptic modulator employing co-planar electrodes. The electrode structure described in this thesis is described as being a “transverse electrode structure” and refers to electrodes lying in separate planes, parallel to

each other and separated by a dielectric sheet, in this case made up of single-crystal lithium niobate, the term “transverse modulator” refers to an electrooptic modulator employing transverse electrodes. A schematic diagram of the basic transverse modulator is shown in Fig. 1.3.

A review of electrooptic modulators and other electrooptic devices developed to date is given below. This review concentrates only on guided wave modulators fabricated in lithium niobate. With few exceptions, the guided wave modulators fabricated to date on ferroelectrics have all used a co-planar electrode structure to apply the electric field to the guided optical field, see Fig. 1.4. This has been necessary to keep the applied modulating field to within practical limits for conveniently low operating voltages. As will be explained in detail in chapter 4, the co-planar electrode structure result in a reduced electrooptic effect since the electric field will contain both a parallel and a perpendicular component, one being in the desired orientation and the other being redundant. By using electrodes on opposite faces of the lithium niobate substrate, i.e. the transverse electrode structure, the electric field will be orientated almost purely along the appropriate perpendicular axis, see Fig. 1.3 and the operating voltage for the modulator will therefore be reduced. Since it is practically very difficult to drop the electric field across a localised area of the lithium niobate substrate it is necessary to remove most of the substrate from the non-guiding region. The full advantages or disadvantages of replacing the standard co-planar electrode structure by a transverse electrode structure on a thinned substrate will be given in chapter 4. The following electrooptic devices are an example of those that could be realised with transverse electrodes to form an integrated optical circuit on a thinned substrate. Firstly, one of the most basic electrooptic devices, the phase modulator, will be reviewed.

1.3.1 The phase modulator.

The simple phase modulator uses an applied electric field to alter the refractive index of the crystal and hence the phase of light being transmitted. One use of the phase modulator is as an optical-frequency translator based on the serrodyne principle¹⁷, which has applications in heterodyne detection and coherent optical communication systems. Kaminow et al¹⁸ demonstrated one of first electrooptic modulators using a planar guide on lithium niobate, although there were demonstrations of electrooptic modulators using bulk optics more than 10 years previous to this. A planar guide was fabricated by the out diffusion

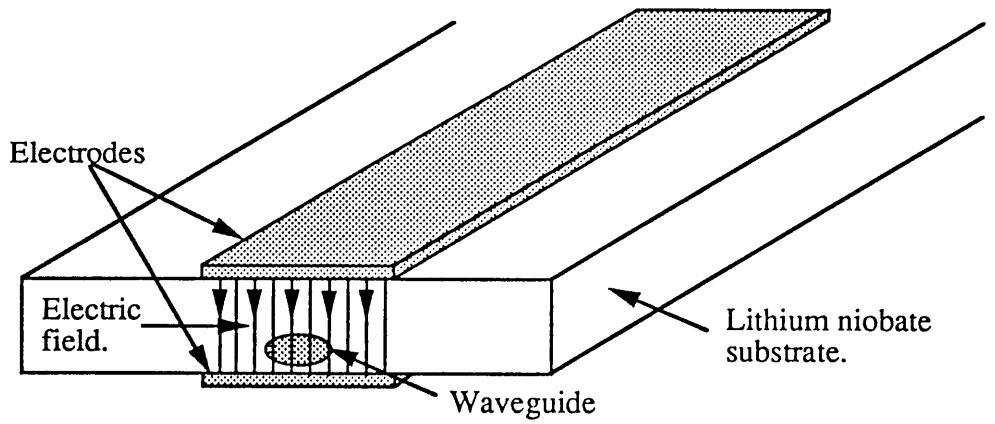


Fig. 1.3. Electrooptic modulator with transverse electrodes..

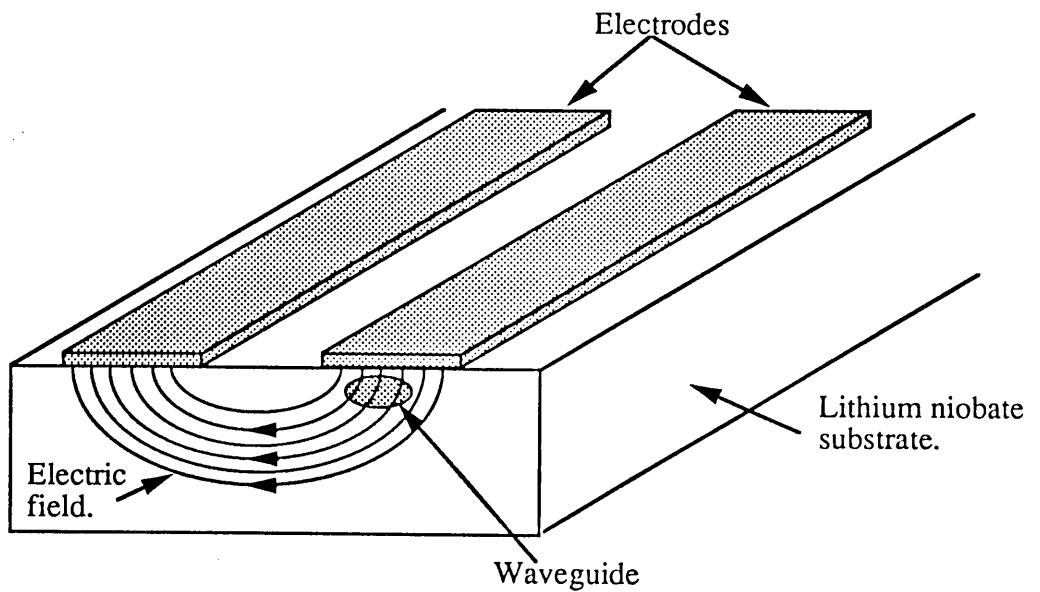


Fig. 1.4. Electrooptic modulator with co-planar electrodes..

of Li₂O from the substrate surface, see section 2.2, the strip electrodes were separated by 57 μm and the light was launched between them using prism coupling. An improvement on this modulator was obtained by replacing the planar guide by a ridge guide with electrodes on opposite walls of the ridge¹⁹. This improved the efficiency of the modulator by reducing the electrode separation and increasing the confinement of the light. After first producing a planar guide using out-diffusion to limit diffraction in the transverse direction, a ridge was formed, limiting diffraction in the lateral plane, by ion-beam etching with a square quartz fibre used as the mask. This resulted in a guide 19 μm wide, 7.5 μm high and 11.5 mm long with an operating voltage, defined as the voltage required for a radian phase shift, of 1.175 V/Rad. The development of titanium indiffused stripe guides made it possible to reduce the electrode spacing to less than 10 μm²⁰. Although the electrode gap was more than halved there was only a 33% reduction in the operating voltage. This was due to a reduction in the uniformity of overlap between the electric and optical fields. The modulator had an operating voltage of 0.3 V/Rad for 30 mm long electrodes.

The advantages of using transverse electrodes can be established by studying Eq. (1.2.12). The electric field produced by co-planar electrodes will not be orientated along a unique crystal axis. To establish the true phase shift induced from the applied electric field, a factor called the overlap integral is introduced. This is a measure of the degree of overlap between the optical field and the electric field oriented along the desired crystal axis. The overlap integral, Γ , has a value equal to or less than one and modifies Eq. (1.2.12) to

$$\Delta\phi = - \frac{\Gamma L \pi R_{mk} n_m^3 E_k}{\lambda} \quad (1.3.1)$$

The use of transverse electrodes provides an electric field with a single component orientated along the perpendicular axis. Provided that the transverse electrodes are wide enough to prevent fringe effects from the edges of the electrodes reducing the effect of the electric field over the area of the optical field, there is a uniform overlap between the electrical and optical fields and therefore the overlap integral is equal to one. The increase in the width between the electrodes and the guide required to prevent fringe effects affecting the electric field at the waveguide will be dependent upon the electrode width to separation ratio and the 1/e width of the guided mode, see chapter 4. The measure of the overlap integral for co-planar electrodes is dependent upon the dimensions of the

electrodes, the optical mode width and the relative position of the electrodes to the waveguide. The overlap integral will be studied in more detail in chapter 4. By using transverse electrodes, the improvement obtained in the electrooptic interaction can increase the phase shift by 100% for given electrode dimensions.

1.3.2 Intensity modulators.

Up to the present, the simplest form of binary digital amplitude modulation has been predominant in communications systems. Phase or frequency modulation have not been used because of their very much more severe demands on the stability of the source frequency. Various electrooptic modulators have been demonstrated which would satisfy the requirements of an amplitude digital communication system, with possibly the most popular type being the Mach-Zehnder waveguide interferometer. In principle the Mach-Zehnder device operates by using a 3dB Y-junction to split the guided light into two identical guides, sufficiently separated to prevent evanescent coupling between the guides. If the two components travel an identical path and there is no induced phase shift, the light from the guides will recombine in phase at a second 3dB Y-junction and constructively interfere and excite the lowest order mode. For an induced phase-shift between the two guides of π the guided modes will recombine to excite the first antisymmetric mode, which is cut-off and rapidly radiates into the substrate. A typical Mach-Zehnder modulator would have a bandwidth in the order of 2-3 GHz and an operating voltage, the voltage required to switch the output from a maximum to a minimum, of approximately 4 V for an electrode length of 4 mm²¹.

Other amplitude modulators suitable for digital communications include the cut-off modulator^{22,23,24} and the directional coupler^{25,26}. In the cut-off modulator, Fig. 1.5, an applied voltage lowers the effective index of a section of the guide until the guided mode is no longer supported and light propagates into the substrate. Neyer²² reported a high-speed cut-off modulator with a bandwidth of 5.3 GHz and an operating voltage of 11 V for 70% extinction. A directional coupler²⁵, Fig. 1.6, uses two guides closely spaced over a length L such that the evanescent fields of the two guided modes overlap. Light couples between the guides with a coupling coefficient per unit length κ , which is dependent upon the waveguide parameters, wavelength, and inter-waveguide separation. For an appropriate length all the light from one guide will be coupled into the other. By applying an electrical field to the guides an index difference between the two

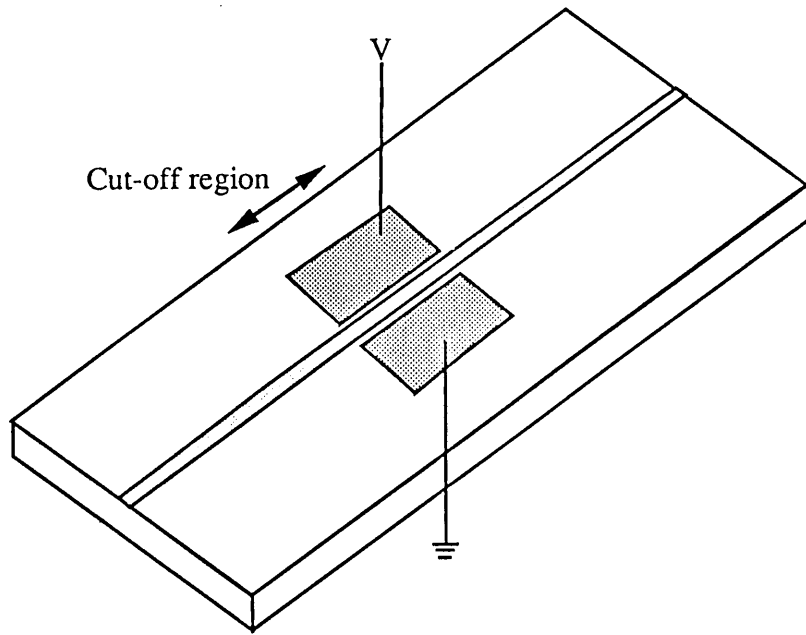


Figure 1.5 Cut-off modulator

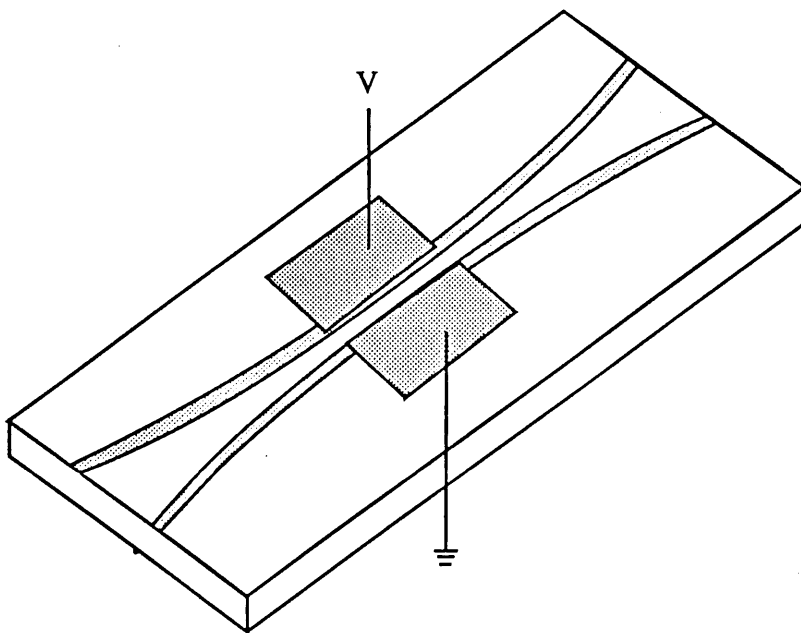


Figure 1.6 Directional coupler

guides can be created. The light which now couples from one guide to the other at different points along the directional coupler will no longer be in phase and the net coupling efficiency can be made zero. Schmitt et al²⁷ recently reported a 3x3-coupler on lithium niobate with a wide range of possible applications, besides its use as a simple amplitude modulator, including a power transfer or power splitter device. 3x3-couplers have several advantages over 2x2-couplers, especially for use in fibre optic sensors since active components are not required for signal processing and they have a high dynamic range.

An alternative to the directional coupler is the X-switch or the total internal reflection (TIR) modulator^{28,29}, see Fig 1.7. An applied field causes the incident light from the top left waveguide to be reflected into the top right waveguide. For zero applied field the light will be guided into the lower right guide. Similarly, light incident in the lower left guide will be reflected into the lower right guide for the appropriate applied field. The operating voltage required for switching is largely independent of electrode length. This allows the bandwidth to be increased independently of the operating voltage. A modulator using a combination of the Mach-Zehnder and the X-switch has been reported by Pohlman et al²⁸. With this device a bandwidth of 6.5 GHz was achieved for an operating voltage of 7 V.

1.3.3 Polarisation matching devices and polarisation independent modulators.

One important type of device still to be examined has possibly more relevance at the detector end of a coherent communication system than at the modulation end. Polarisation matching devices such as polarisation controllers, polarisation diversity circuits, and 90°-hybrids for phase-diversity reception are required in coherent systems due to the limitations imposed by the variations in state-of-polarisation in standard single mode fibres. The use of polarisation maintaining fibres (PMF) would solve the problem but they are expensive and will probably not become a standard fibre for long distance communications. The use of the various other options has been reviewed by Hoffman et al³⁰. Polarisation controllers have complicated control requirements and complex electrooptical behavior which may limit their application to areas of coherent communication where the receiver sensitivity is critical, i.e long-haul transmission systems. The polarisation diversity scheme requires twice the optoelectronic effort at the detector side than a SOP-control scheme and as yet, although suggested in theory, the fabrication of such a scheme on lithium niobate

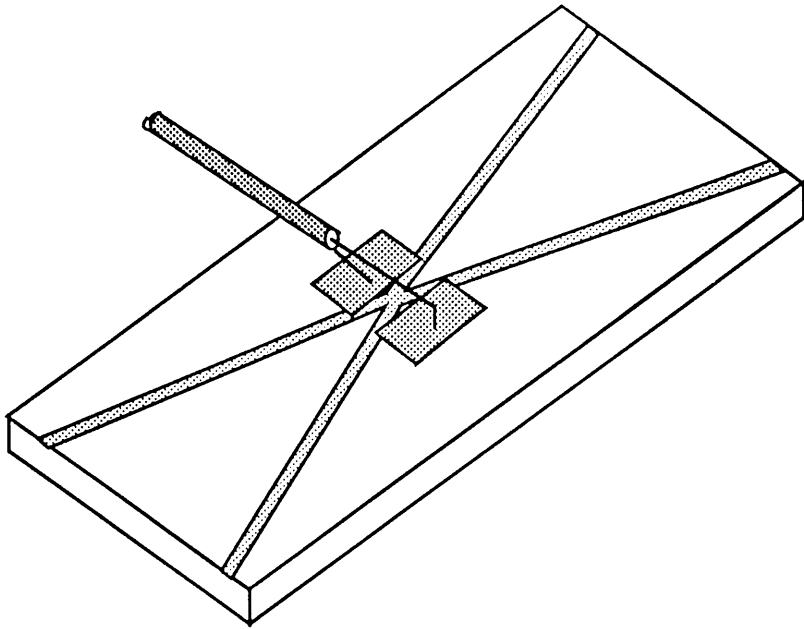


Figure 1.7 The x-switch or Total Internal Reflection Modulator

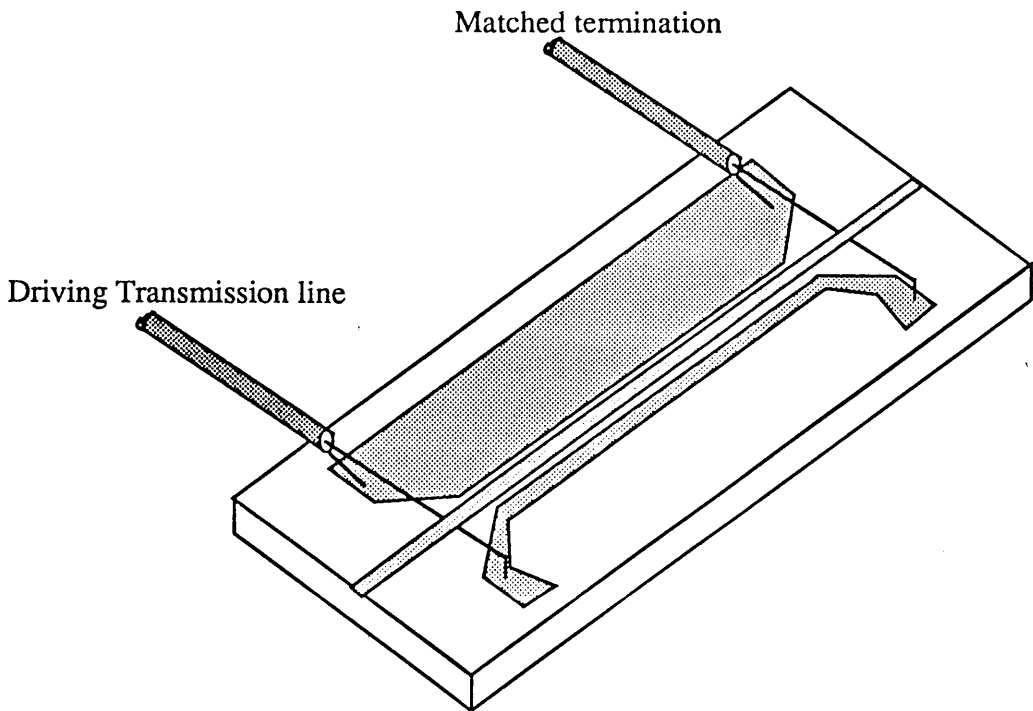


Figure 1.8 Travelling wave electrodes.

has not yet been reported. An alternative is the use of polarisation scrambling (PSC) which, although requiring a PSC device with at least twice the transmitted bit rate, is especially attractive for distribution networks since it has only to be realised once per channel at the distribution point. The use of phase diversity receivers in phase shift keying (PSK) homodyne systems is promising as it allows optimum use of the local oscillator power and suppression of the local oscillator intensity noise as well as baseband detection.

A possible alternative to controlling the state-of-polarisation is to use polarisation independent modulators. Several alternative methods have been demonstrated that provide switching independent of the state of polarisation³¹. The most popular technique is the use of directional couplers for which there is a limited range where the L/l_c ratios of the TE and TM modes will allow a good cross-state result. Problems resulting from the polarisation independent switches due to DC drift and temperature drift can be overcome by using feedback from the output. Crosstalk levels below -30dB have been achieved with a control system continuously adjusting the electrode voltage³².

1.3.4 Lumped, standing- and travelling-wave electrodes.

Two types of electrode arrangement are commonly used in modulators and other devices: lumped electrodes and travelling-wave electrodes. Lumped electrodes, where the electrode length is less than a quarter of the microwave wavelength, have a bandwidth limited by the electrode charging time which is determined by the electrode capacitance, C , in turn determined primarily by the physical dimensions of the modulator, and the terminating impedance, R , required to match the modulator to the characteristic impedance of the drive source. The bandwidth-length product for a lumped modulator is therefore given by :

$$\Delta f \cdot L = \frac{1}{\pi RC} \quad (1.3.2)$$

where C is the capacitance per unit length and R is the terminating impedance of the modulator which will be matched to the characteristic impedance of the drive source.

The easiest way to increase the bandwidth is to make a trade-off with the operating voltage or power by reducing the length of the electrodes, see Eq. (1.2.12), or by increasing the electrode gap and thereby reducing the capacitance. For most situations the characteristic impedance of the modulator will be set at 50Ω in order to match the source impedance although this may be made smaller or larger for specific applications. The dependence of the bandwidth on the physical dimensions of the modulator will be looked at in more detail in chapter 4. For a practical operating voltage the bandwidth of the typical lumped electrode modulator is limited to approximately 4 GHz. By using travelling wave electrodes the bandwidth is limited by the difference in transit time along the electrode length between the modulating RF field and the optical field. The travelling wave electrode structure should appear as an identical extension of the driving transmission line and must therefore have the same characteristic impedance as the source and cable. Care is also required for the coupling to the electrodes as well as the termination of the electrodes. The basic design for the travelling wave electrode structure is shown in Fig 1.8. The asymmetrical electrodes provide low electrical propagation loss and easy coupling to the drive source³³. A measure of the difference between the velocities of the optical and microwave fields is given by the velocity mismatch, $\partial = 1 - n_o/n_m$, where n_o and n_m are the optical and microwave indices. The bandwidth-length product for an asymmetrical travelling wave electrode structure can be calculated from :

$$\Delta f \cdot L = \frac{2c}{\pi n_m \partial} \quad (1.3.3)$$

where L is the electrode length and c is the velocity of light. Gee et al³⁴ has reported a travelling wave modulator with a bandwidth of 17 GHz for an electrode length of 6 mm. A recently reported travelling wave modulator³⁵ design uses an air gap between the electrodes to reduce the effective microwave index to equal the optical index and increase the bandwidth to the limits imposed by practical losses in the system but the feasibility of fabrication has still to be demonstrated.

The walkoff between the optical and electrical signals which limits the bandwidth for a travelling wave modulator can be overcome by using phase-reversal electrodes³⁶, Fig 1.9, which artificially match the velocities of the optical and microwave fields. The phase-reversal modulator works around a

selected centre frequency, as opposed to the baseband operation of the travelling wave modulator. After an interaction length L_i , the electrodes are switched so as to reverse the polarity of the applied field. The length L_i is chosen so that the reversed field exactly compensates for the polarity reversal created by the walkoff between the two signals at the design frequency, f_d . At frequencies other than the design frequency, the induced field reversal does not match the walkoff-induced polarity reversal, resulting in no effective velocity matching. The effective velocity-match condition is given by

$$\frac{2\pi n_m}{c} f_d L_i \partial = \pi \quad (1.3.4)$$

The induced phase shift for each of the reversed sections shown in Fig. 1.9 adds in phase. Since each section is effectively phase-locked, the total interaction length, determined by the number of reversal sections, can, in the absence of loss, be made arbitrarily long. The required drive-voltage can therefore be reduced without a reduction in centre frequency.

An extension of the phase reversal electrodes is the use of electrode patterns based on Barker sequences. Dolfi et al³⁷ reported a modulator with an electrode structure representing a 13 bit Barker sequence capable of a bandwidth in excess of 100 GHz. Due to limitations in the microwave packaging, the modulator was limited to approximately 50 GHz for an operating voltage of 7.5 V.

In contrast to the travelling wave modulator, the standing wave modulator³⁸ exhibits a narrow bandwidth of a few gigahertz centred at a high frequency (approximately 10 GHz.). The electrode structure for the standing wave modulator is shown Fig. 1.10. The resonant section is modelled by the frequency response of two shorted transmission lines of unequal length connected in parallel. The overall length of the combined structures is approximately equal to half a guide wavelength at the desired frequency. Thus the total length is dependent upon the desired operating frequency, which is dependent upon the propagation constant, the waveguide geometry and the dielectric constant of the substrate material. The key advantage of the standing wave modulator over the lumped or travelling wave modulators is the enhanced voltage arising from its resonant mode of operation. The maximum voltage along

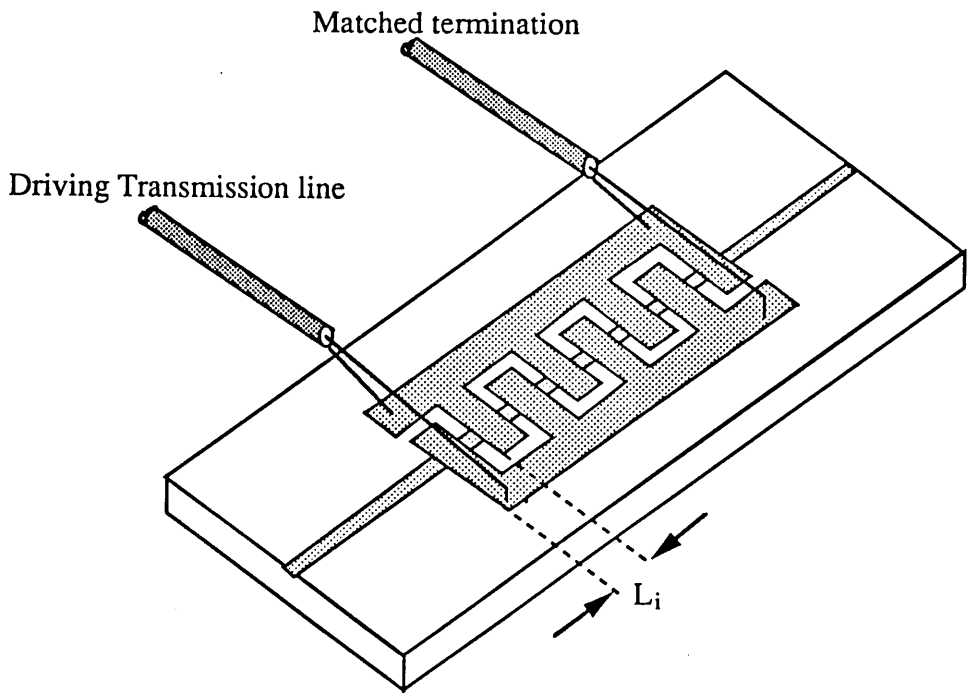


Figure 1.9 Travelling wave modulator with periodic phase reversal electrodes.

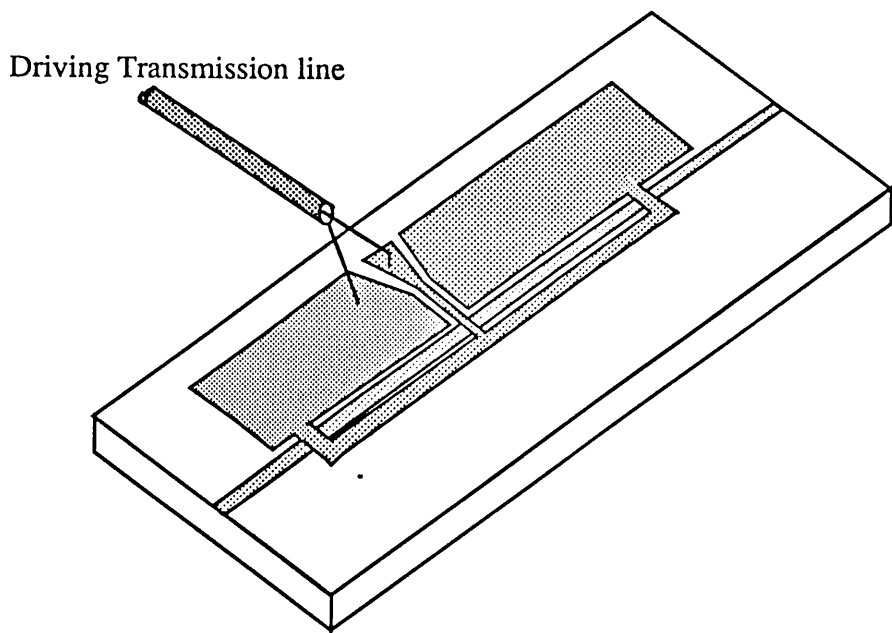


Figure 1.10 Standing wave electrodes.

the line can be considerably greater than the driving voltage and thereby increase the electrooptic phase shift.

1.4 Measurement of the electrooptic coefficients by means of the transverse electrooptic phase modulator.

Besides the use of co-planar electrodes to fabricate modulators for use in communications, signal processing and other applications, they are also used to estimate the electrooptic coefficients of waveguides fabricated by existing or novel techniques. By measuring the electrooptically induced phase-shift for a given applied voltage the electrooptic coefficients can be calculated but, as previously mentioned, the use of co-planar electrodes reduces the effect of the applied electric field by a factor called the overlap integral which, as will be explained in detail in section 4.2, is a measure of the uniformity of the electric field over the optical field. In order to calculate the overlap integral an accurate knowledge is required of both the optical and electrical field profiles. The electrical field distribution from co-planar electrodes^{39,40} can be accurately calculated for a given electrode separation and width. The refractive index profile and optical field profile are strongly dependent upon the fabrication parameters under investigation and must therefore be found by either direct measurement of the output optical field profile using an end-fire arrangement or the refractive index profile can be calculated by the inverse WKB method from the effective mode-indices measured using prism-coupling. Inaccuracies in the determination of either field profile will lead directly to inaccuracies in the measured electrooptic coefficients.

By using a transverse electrode structure straddling the waveguides under investigation, it can be assumed that there is a nearly uniform distribution of the electric field through the optical field and the overlap integral is therefore equal to unity. It should be borne in mind that any changes in the resistivity of the lithium niobate that may be induced by the guide fabrication will create a non-uniform field which may decrease or increase the local electrooptic effect. It would be extremely hard to allow accurately for these localised changes in the resistivity and the measured electrooptic coefficient should therefore be considered the true value for the guide.

Part of the objective of the thesis was to demonstrate the use of a transverse electrode structure to measure the electrooptic coefficients of titanium-

indiffused guides and its subsequent use to investigate the electrooptic coefficients of proton-exchange guides fabricated using a novel technique developed by Loni et al⁴¹ and described in section 2.4.

References.

1. Ballman A.A., "Growth of piezo-electric and ferroelectric materials by the Czochralski technique", J. Amer. Ceram. Soc. **48**. Feb. 1965. pp 112-113.
2. Fedulov S.A and Shapiro Z.I., "The growth of crystals of LiNbO_3 , LiTaO_3 and NaNbO_3 by the Czochralski method," P.B. Ladyzhinskii, Sov. Phys. Cryst. **10**. March 1965. pp 218-220.
3. Svaasand L. O., Eriksrud M., Nakken G. and Grale A. P. "Solid-solution range of lithium niobate", J. Cryst. Growth. **22**. 1974. pp 239.
4. Carruthers J. R., Peterson G. E., Grasso M. and Bridenbaugh P. M. "Nonstoichiometry and crystal growth of LiNbO_3 ", J. Appl. Phys. **42**. 1971. pp 1846-1851
5. Bergman J. G., Ashkin A., Ballman A. A., Dziedzic J. M., Levinstein H. J. and Smith R. G. "Curie temperature, birefringence, and phase-matching temperature variations as functions of melt stoichiometry", Appl. Phys. Lett. **12**. February 1968. pp 92-94.
6. Byer R. L., Young J. F. and Feigelson R. S. "Growth of high-quality lithium niobate crystals from the congruent melt", J. Appl. Phys. **41**. May 1970 pp 2320-2325.
7. Midwinter J. E. "Lithium niobate: effects of composition on the refractive indices & optical second harmonic generation", J. Appl. Phys. **39**. June 1968. pp 3033-3038
8. Turner E. H., Nash F. R. and Bridenbaugh P. M. "Dependance of linear electrooptic effect & dielectric constants on melt composition in lithium niobate", J. Appl. Phys. **41**. 1970. pp 5278-5281.

9. Nassau K., Levinstein H. J. and Loiacono G. M. "Ferroelectric lithium niobate 1: growth, domain structure, dislocations, & etching", *J. Phys. Chem. Solids.* **27.** 1966. pp 983-988.
10. Nassau K., Levinstein H. J. and Loiacono G. M. "Ferroelectric lithium niobate 2: preparation of single domain crystals", *J. Phys. Chem. Solids.* **27.** 1966. pp 989-996.
11. Abrahams S. C., Reddy J. M. and Bernstein J. L. "Ferroelectric lithium niobate 3: single-crystal x-ray diffraction study at 24 °C", *J. Phys. Chem. Solids.* **27.** 1966. pp 997-1012.
12. Abrahams S. C., Hamilton W. C. and Reddy J. M. "Ferroelectric lithium niobate 4: single-crystal neutron diffraction study at 24 °C", *J. Phys. Chem. Solids.* **27.** 1966. pp 1013-1018.
13. Abrahams S. C., Levinstein H. J. and Reddy J. M. "Ferroelectric lithium niobate 5: polycrystal x-ray diffraction study between 24 °C and 1200 °C", *J. Phys. Chem. Solids.* **27.** 1966. pp 1019-1026.
14. Weis R. S. and Gaylord T. K. "Lithium niobate: Summary of physical properties and crystal structure", *Appl. Phys. A* **37.** 1985 pp 191-203.
15. Rauber A. "Chemistry and physics of lithium niobate", *Current Topics in Materials Science*, **1.** Ed. E. Kaldis, North-Holland 1978.
16. Nye J. F. "Physical properties of crystals." Oxford University Press, London 1957. pp 241-249.
17. Wong K. K., De La Rue R. M. and Wright S. "Electro-optic-waveguide frequency translator in LiNbO₃ fabricated by proton exchange", *Opt. Lett.* **7.** November 1982. pp 546-548.

18. Kaminow I. P., Carruthers J. R., Turner E. H. and Stulz L. W. "Thin-film lithium niobate electro-optic light modulator ", Appl. Phys. Lett. **22**. May 1973 pp 540-542.
19. Kaminow I. P., Ramaswamy V., Schmidt R. V. and Turner E. H. "Lithium niobate ridge waveguide modulator ", Appl. Phys. Lett. **24**. June 1974 pp 555-557.
20. Kaminow I. P., Stulz L. W. and Turner E. H. "Efficient strip-waveguide modulator", Appl. Phys. Lett. **27**. November 1975 pp 555-557.
21. Becker R. A. "Broad-band guided-wave electrooptic modulators", IEEE J. Quantum Electron. **QE-20**. July 1984. pp 723-727.
22. Neyer A. and Sohler W. "High-speed cut-off modulator using a Ti-diffused LiNbO₃ channel waveguide", Appl. Phys. Lett. **35**. August 1979. pp 256-258.
23. Ashley P. R. and Chang W. S. C. "Improved mode extinction modulator using a Ti in-diffused LiNbO₃ channel waveguide", Appl. Phys. Lett. **45**. October 1984 pp 840-842.
24. Chen R. and Tsai C. S. "Thermally annealed single-mode proton-exchanged channel-waveguide cut-off modulator", Optic. Lett. **11**. August 1986. pp 546-548.
25. Alferness R. C. "Optical directional couplers with weighted coupling", Appl. Phys. Lett. **35**. August 1979. pp 260-262.
26. Bozhevol'nyl S. I., Buritskil K. S., Zolotov E. M., Prokhorov A. M. and Chernykh V. A. "Investigation of an electrooptic modulator formed from coupled channel diffused waveguides LiNbO₃", Sov. J. Quantum Electron. **12**. September 1982. pp 1165-1169.

27. Schmitt G., Wenzel W. and Dolde K. "Integrated optical 3x3-coupler on LiNbO₃: comparison between theory and experimental", 5th European Conference on Integrated Optics. April 26-28th 1989. Paper 1141.13.
28. Pohlman T., Neyer A. and Voges E. "Ti:LiNbO₃ interferometric activated X-switch for high-speed applications : IAX", Elec. Lett. **24**. April 1988 pp 530-531.
29. Yariv A. "Coupled-mode theory for guided wave optics", IEEE J. Quantum Electron. **QE-9**. 1973. pp 919-934.
30. Hoffman D. and Heidrich H. "LiNbO₃ devices for coherent communication applications." 5th European Conference on Integrated Optics. April 26-28th 1989. Paper 1141.12.
31. Granstrand P. "Polarization independent switches in Ti:LiNbO₃, critical review of the solutions and their applications.", 5th European Conference on Integrated Optics. April 26-28th 1989. Paper 1141.39.
32. Djupsjobacka A., Granstrand P., Lagerstrom B., Svenson P. and Thylen L. "Stability of polarisation-independent LiNbO₃ switches", 5th European Conference on Integrated Optics. April 26-28th 1989. Paper 1141.42.
33. Alferness R. C. "Waveguide electrooptic modulator." IEEE Trans. Microwave Theory and Tech. **MTT-30**. August 1982. pp 1121-1136.
34. Gee C. M., Thurmond G. D. and Yen H. W. "17-GHz bandwidth electro-optic modulator", Appl. Phys. Lett. **43**. December 1983. pp 998-1000.
35. Minakata M. et al. "Design of a broad-band travelling wave optical modulator based on velocity matching", Second Optoelectronics Conference (OEC '88) **3C**. October 1988 pp 164-165.
36. Alferness R. C. Korotky S. K. and Marcatili E. A. J. "Velocity matching techniques for integrated optic travelling wave switch/modulators", IEEE J. Quantum Electron. **QE-20**. March 1984. pp 301-309.

37. Dolfi D. et al. "40 GHz electro-optic modulator with 7.5 V drive voltage", *Elec. Lett.* **24**. April 1988. pp 528-529.
38. Clark D. F. "High frequency electro-optic modulators for integrated optics", PhD. Thesis, Glasgow University, 1986.
39. Marcuse D. "Optimum electrode design for integrated optics modulators", *J. Quantum Electron.* **QE-18**. March 1982. pp 393-398.
40. Vandebulcke P. and Lagasse P. "Static field analysis of thin film electrooptic light modulators and switches." *Wave Electron.* **1**. 1976. pp 295-308.
41. Loni A., De La Rue R. M. and Winfield J. M. "Very low loss proton-exchange waveguides with a substantially restored electrooptic effect." Paper MD-3, Topical meeting on Integrated and guided wave optics, March 28-30, New Mexico, 1988, Opt. Soc. America (Washington).

Chapter 2.

Waveguide fabrication technique.

Optical waveguides may be fabricated in lithium niobate using several different methods; the out-diffusion of Li_2O from the crystal surface¹, the indiffusion of metals², ion-implantation³ and ion- or proton-exchange⁴. The two most widely used methods are titanium-indiffusion and proton-exchange in benzoic acid. The ideal waveguide technology gives low loss, small scattering, a high index change for low losses associated with bends etc, an index profile that will match optical fibres and high electrooptic coefficients. A review of the basic fabrication techniques of titanium-indiffused and proton-exchanged waveguides and the chemical interactions which occur during fabrication will be presented in the following sections with a brief discussion of out-diffusion. The titanium-indiffused and proton-exchanged techniques were employed in fabrication of the transverse electrooptic modulator whilst the out-diffusion, although not employed in this thesis as a waveguide fabrication technique, is relevant as it frequently accompanies titanium-indiffusion.

2.1 Out-diffusion.

Kaminow et al¹ first demonstrated the fabrication of waveguides by the out-diffusion of Li_2O from the LiNbO_3 crystal surface. The out-diffusion typically takes place between 1000 and 1100 °C for several hours in a vacuum or oxidising atmosphere. LiNbO_3 crystallises into the non-stoichiometric form $(\text{Li}_2\text{O})_y(\text{Nb}_2\text{O}_5)_{1-y}$. It has been shown that the ordinary index, n_o , is independent of crystal stoichiometry whilst the extraordinary index, n_e , increases linearly as y decreases in the range $0.48 < y < 0.50$ ($y = 0.50$ corresponds to LiNbO_3). The low activation energy and high mobility of the lithium ions results in the easy out-diffusion of Li_2O , a problem for waveguides fabricated with titanium-indiffusion. The resulting guide has only an increased extraordinary index with a maximum at the surface and a depth profile which can be mathematically modelled by the complementary error function.

Holman et al⁵ has demonstrated control of the stoichiometry of the crystal using either out- or indiffusion of Li_2O to form the guides in the LiNbO_3 . Out-diffusion in a wet O_2 atmosphere results in guides with a reduced susceptibility to the photorefractive effect. This can possibly be attributed to the indiffusion of

protons from the water vapour which will increase the conductivity of the guiding region and decrease the effect of the optically induced electric field from the photorefractive effect. The out-diffusion of Li_2O can also affect other waveguide fabrication techniques in a detrimental manner, as will be discussed in the following sections.

2.2 The titanium-indiffusion process.

The indiffusion of certain metal atoms into LiNbO_3 produces alterations in optical properties and specifically in the refractive index. The substitutional site for the metal atoms depends on whether the atom is divalent, trivalent or tetravalent. Titanium, being tetravalent, is substitutional for Nb in the LiNbO_3 crystal lattice and has proved to be the most attractive of the metals for indiffusion. Titanium-indiffusion increases both the ordinary ($\Delta n_o < 0.04$) and extraordinary ($\Delta n_e < 0.02$) refractive indices allowing both TE and TM polarised light to be guided. The exact mechanism by which the indiffusion of titanium increases the refractive index is not yet fully understood but it appears to be due to several complex interactions^{6,7}. The difference in the ionic radius of the Ti^{4+} (0.605 Å) and Nb^{5+} ions (0.64 Å) is considered possibly to create an increase in the refractive index through the photoelastic effect while also changing ionic polarisability⁶. Other possible sources of the increase in the refractive indices are a change in the spontaneous polarisation through the Kerr effect, which changes the electronic distribution within the oxygen sublattice which possibly has a large effect on the extraordinary index, and a change in ion polarisability due to impurity ions.

The standard method for fabricating titanium indiffused waveguides commences with deposition of a titanium film onto the LiNbO_3 substrate by means of electron-beam evaporation, sputtering or thermal sublimation. Film thicknesses typically in the region of 200 to 1000 Å have been used. This enables the fabrication of either planar or, by the use of lithography, stripe guides. The indiffusion of the titanium takes place between 900 and 1150 °C, with diffusion times between 0.5 and 30 hours. The scattering is dependent upon the diffusion time, with the optimum time increasing with the titanium film thickness. For a film thickness of 250 Å, a diffusion time of 10 hours at 1000 °C is used to minimise the scattering. The scattering can be attributed to three main causes, firstly the non-uniformities which occur during the titanium diffusion will create refractive index irregularities in the guide and at the surface, secondly

the roughness left on the surface after diffusion and thirdly the crystal strains and defects induced by the titanium ions in the guiding region.

The indiffusion process can be broken down into several stages^{8,9,10}:

- 1) firstly the titanium oxidises to form TiO_2 during the furnace heat up period at approximately 500 °C.
- 2) In the absence of a wet atmosphere during diffusion the LiNb_3O_8 crystalline phase appears at 600 °C and rapidly disappears after reaching a maximum at 800 °C. A wet atmosphere inhibits the formation of LiNb_3O_8 .
- 3) The TiO_2 layer forms an intermediate rutile structure initially suspected to be $\text{Ti}_{0.65}\text{Nb}_{0.35}\text{O}_2$ ⁸ but later shown to be more likely $(\text{Li}_{0.25}\text{Nb}_{0.75}\text{O}_2)_{0.42}(\text{TiO}_2)_{0.58}$ ⁷. This intermediate phase is consistent with the known phase relationships in the $\text{Li}_2\text{O}:\text{Nb}_2\text{O}_5$ and the $\text{TiO}_2:\text{LiNbO}_3$ systems. It is this rutile compound that is the real source for the subsequent titanium-indiffusion into the LiNbO_3 .
- 4) At temperatures usually as high as 1000 °C the titanium diffuses from the surface layer into the substrate until the $(\text{Li}_{0.25}\text{Nb}_{0.75}\text{O}_2)_{0.42}(\text{TiO}_2)_{0.58}$ is completely depleted and disappears. Just before the process is complete, investigation of the surface layer by scanning electron microscopy has revealed islands of the mixed oxide. This reveals the non-uniform nature of the indiffusion process that is responsible for the refractive index inhomogeneities which create in-plane scattering. Increasing the diffusion time reduces the surface roughness and decreases the inhomogeneities in the index.

Although the surface roughness and index homogeneities are reduced by increasing the diffusion time, the in-plane scattering increases. This can be explained by the increase in crystal strain and defects induced in the guiding region. The difference in the ionic radius of the Ti^{4+} ions and the Nb^{5+} ions whose lattice sites they tend to occupy creates a negative strain with a magnitude in the region of $-\Delta a/a = 2 \times 10^{-3}$ to 5×10^{-4} , which is dependent upon the titanium concentration and therefore the diffusion time⁹. Transmission electron microscopy and X-ray topography have been used⁹ to study the formation of the

crystalline defects. The results showed that the defects are induced by the diffusion process and that the density of the defects increases with increasing diffusion time. It is this increase in the defect density that limits the amount to which the in-plane scattering can be reduced by increasing the diffusion time. Twigg et al¹¹ has recently attributed these defects to lithium sites which are randomly occupied by niobium ions and the consequent existence of vacant niobium sites.

It is important to be able to calculate accurately the titanium concentration profile and refractive index profile for given fabrication parameters. The overlap integral, discussed briefly in section 1.3 and in more detail in chapter 4, the coupling length for a directional coupler and efficient matching to an optical fibre are all dependent upon an accurate knowledge of the guided mode profile. Although several reported values show that the diffusion of the Ti⁴⁺ ions into the LiNbO₃ substrate is anisotropic, with a diffusion coefficient in the z-direction 50% greater than that in the x-direction^{12,13}, other reported values indicate no anisotropy with a value of 1.1×10^{-12} cm²/s at 1050 °C¹⁴ and a strong dependence of the diffusion coefficient upon the stoichiometry of the crystal. The diffused titanium concentration has been shown to be closely modelled by a Gaussian profile in the depth direction and an error function in the lateral direction¹⁵ and can be described by the following approximation:

$$C(x, y) = C_0 \left[\exp \left[- \left[\frac{y}{2\sqrt{(D_x t)}} \right]^2 \right] \cdot \frac{1}{2} \cdot \left[\operatorname{erf} \left[\frac{w + 2z}{4\sqrt{(D_z t)}} \right] + \operatorname{erf} \left[\frac{w - 2z}{4\sqrt{(D_z t)}} \right] \right] \right] \quad (2.2.1)$$

where D_x and D_z are the diffusion coefficients along the x and z directions, 9.7×10^{-13} and 1.4×10^{-12} cm²/sec respectively¹³, t is the indiffusion time, W is the titanium strip width and C_0 is a parameter related to the total titanium ion concentration along the guide, $C_0 = \tau / (a \cdot D_x)$ where τ is the film thickness and $a = 1.57 \times 10^{-23}$ cm³.

The modification in the extraordinary index is linearly proportional to the titanium concentration, while the ordinary index can be well-defined with a sublinear relationship with the titanium concentration¹⁶. The increases in the indices are related to the titanium concentration by :

$$\Delta n_e = \frac{0.839 (\lambda / \mu\text{m})^2}{(\lambda / \mu\text{m})^2 - 0.0645} \cdot 1.2 \times 10^{-23} \cdot C(x, y) \quad (2.2.2)$$

$$\Delta n_o = \frac{0.67 (\lambda / \mu\text{m})^2}{(\lambda / \mu\text{m})^2 - 0.13} \cdot (1.3 \times 10^{-25} \cdot C(x, y))^{0.55} \quad (2.2.3)$$

Figure 2.1 shows the change in the ordinary and extraordinary indices produced by a strip of titanium 300 Å thick and 7 μm wide indiffused at 1050 °C for 8 hours.

Strake et al¹⁶ has compared the two main methods for the calculation of optical mode profiles, the scalar finite-element method (FEM) and the effective-refractive-index method (ERI). Although the ERI method is not mathematically rigorous it is almost completely analytical and, except for weakly guiding modes, provides a reasonable accurate measure of the fundamental mode field maximum and propagation constant. For problems requiring an exact numerical solution of the wave equation, techniques such as the FEM technique must be used. The FEM is able to compute the mode profile for guides with an arbitrary index profile but can require long computations while the ERI method uses an approximation of the index profile given and therefore leads to very fast computations.

While the titanium is diffusing into the LiNbO₃ substrate, there is an out-diffusion of Li₂O from the surface of the LiNbO₃. Lithium has a low activation energy and therefore diffuses very rapidly compared to the niobium or oxygen. Where a stripe guide is to be produced this may result in a slab guide at the surface of the LiNbO₃, in addition to the stripe guide. One method, reported by Chen et al, to suppress the out-diffusion¹⁷ places the LiNbO₃ substrate in a lithium rich atmosphere. This atmosphere is created by annealing the samples packed in high-purity LiNbO₃ powder at 900 °C in a flowing oxygen environment for 1 h or more. Since the LiNbO₃ powder has a larger ratio of surface area to volume than the LiNbO₃ substrate the Li₂O outgassed from the powder may be sufficient to create a Li₂O rich environment and hence suppress the Li₂O out-diffusing from the substrate. The LiNbO₃ powder treatment can be carried out either before or simultaneously with the titanium-indiffusion process.

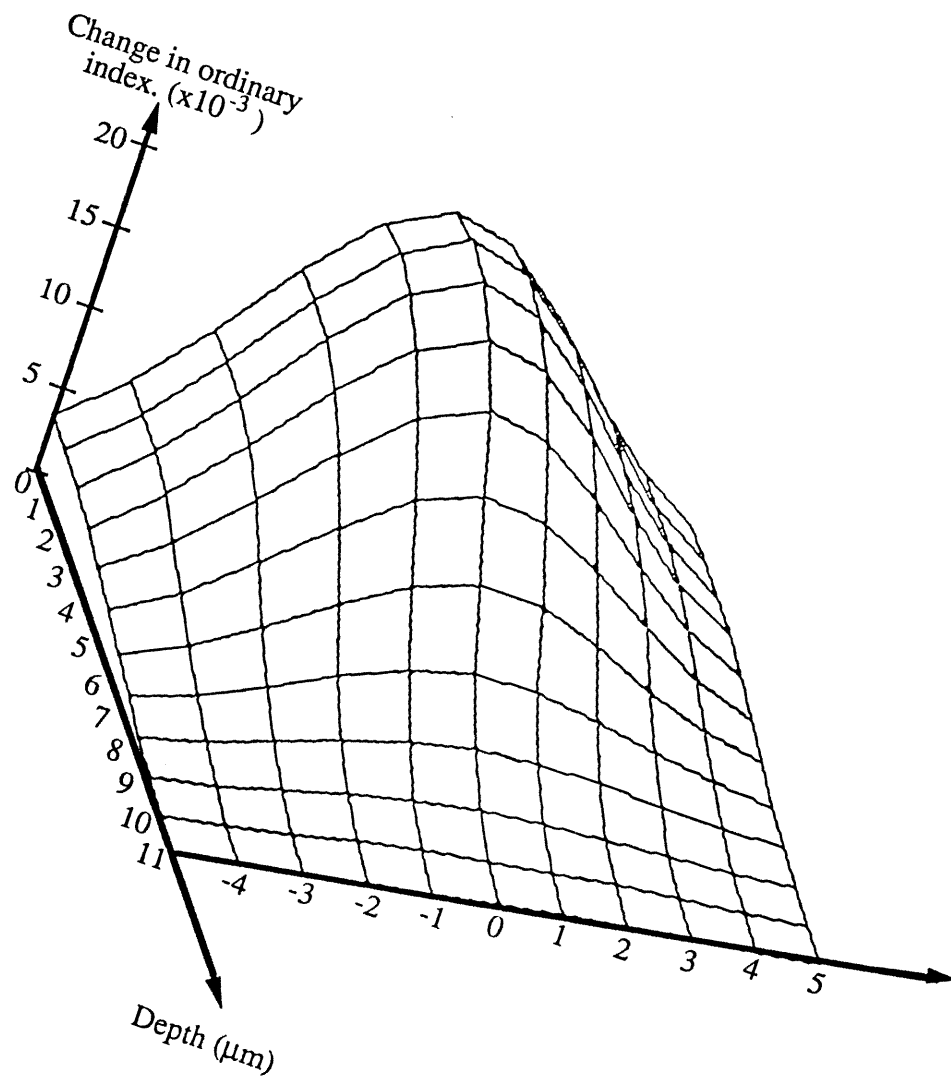


Fig. 2.1(a). Change in the ordinary index from a $7 \mu\text{m}$ wide, 300 \AA thick titanium strip indiffused at 1050°C for 8 hours.

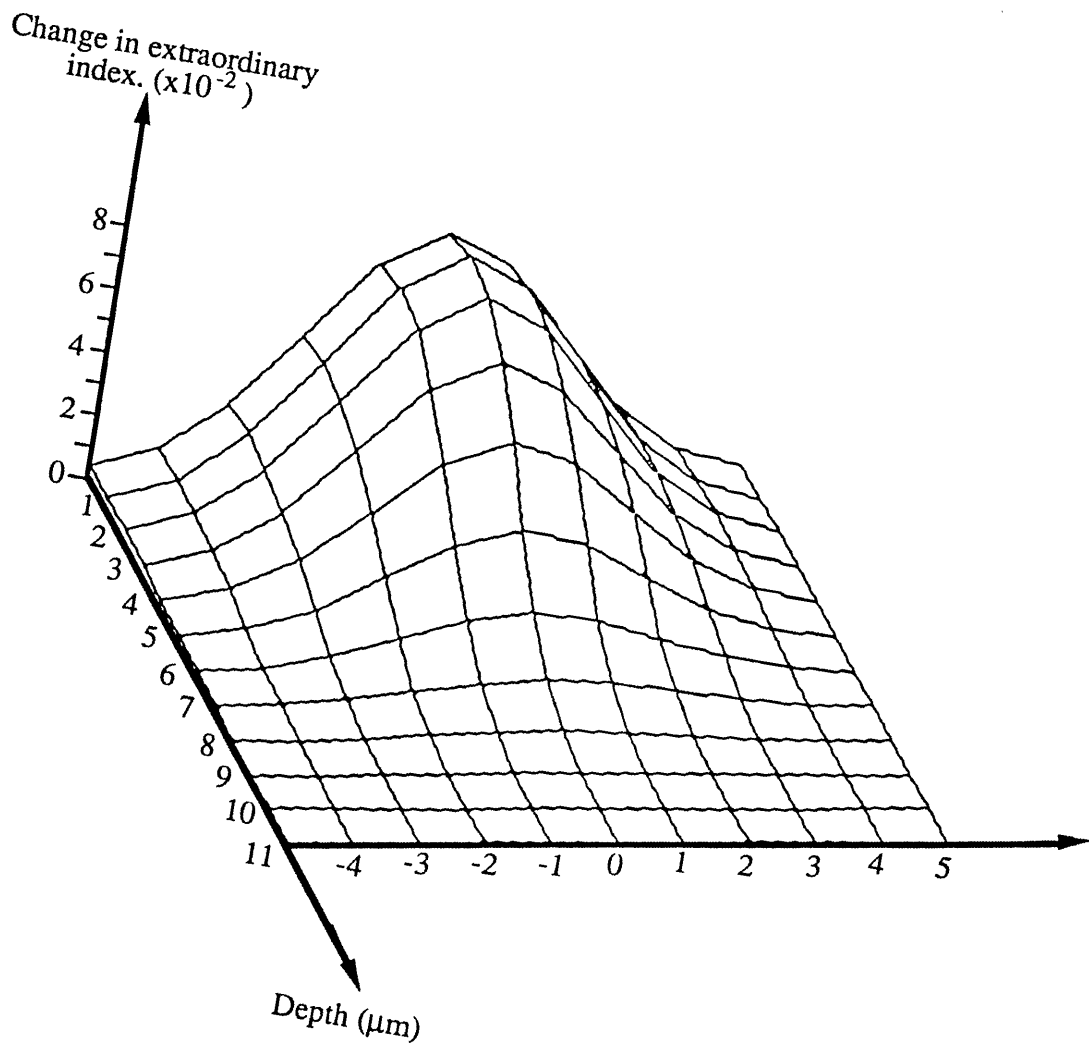


Fig. 2.1(b). Change in the extraordinary index from a $7 \mu\text{m}$ wide, 300 \AA thick titanium strip indiffused at $1050 \text{ }^\circ\text{C}$ for 8 hours.

Esdaile¹⁰ suggested the alternative of annealing the samples in a closed tube. The inclusion of LiNbO₃ powder in the tube was felt to be undesirable since it tends to sinter on to the LiNbO₃ substrate surface, while an equilibrium vapor pressure of Li₂O over the LiNbO₃ substrate was rapidly attained with a negligible loss of Li₂O from the substrate. This approach prevented the lithium rich atmosphere from being carried away by the flowing gas. Since the diffusion took place using ambient air in the closed tube, there was a reduced possibility of the optical damage which has been found to occur for samples annealed in an Ar atmosphere. One established method used at Glasgow University involves indiffusion with wet oxygen (pure oxygen flowing through water preheated to 70 °C) flowing over LiNbO₃ powder placed before the sample. This combines the method reported by Chen with the observation of Jackel et al¹⁸ that indiffusion in a water vapour atmosphere eliminates the outdiffusion of Li₂O by inhibiting the LiNb₃O₈ phase. The presence of the wet O₂ vapour has also been found to reduce the amount of optical damage due to an indiffusion of protons¹⁸. Good quality waveguides can now be routinely fabricated, using titanium-indiffusion, with losses well under 1dB/cm. The exact mechanisms by which the various methods work are not yet fully understood and the development of an understanding has evolved through trial and error, with only a limited amount of exact scientific understanding.

The effect of titanium-indiffusion upon the optical damage or photorefractive effect has been studied by several workers^{19,20,21}. The photorefractive effect can be split into two components, the photovoltaic effect and the photoconductive effect. The photovoltaic effect describes an optically induced change in the refractive index in the absence of an electric field, while the photoconductive effect describes an optically induced change in the refractive index in the presence of an electric field. The physical nature by which the change in the refractive index is optically induced will be discussed in detail later in chapter 5. The photorefractive effect in bulk LiNbO₃²² is normally dominated by the photovoltaic effect within the range of applied field strengths consistent with those of a modulator. Following titanium-indiffusion Becker et al²³ reported no increase in the photovoltaic effect from that observed in bulk LiNbO₃ for a Mach-Zehnder structure formed on x-cut LiNbO₃. The photoconductive effect showed a substantial increase to become the dominant photorefractive effect for a field strength of 5×10^3 V/cm. Schmidt et al²⁰ reported similar effects, using a directional coupler on z-cut LiNbO₃, or a field strength of 10^4 V/cm, with the magnitude of the effect decreasing very strongly with increasing

wavelength. Harvey²¹ has made a comparison between both Mach-Zehnder devices and directional couplers fabricated on z-cut LiNbO₃. The directional coupler showed an effect in agreement with Schmidt et al²⁰ while little effect was observed in the Mach-Zehnder. Harvey used a biasing field strength of 10³ V/cm, at which level the degree of damage due to the photoconductive effect is reduced enough for the photovoltaic effect to be dominant. For a perfect match in the optical profile between both arms of the Mach-Zehnder, the photovoltaic effect should have no effect on the output, assuming the optical power density is not enough to alter the guide profile on the output arm.

A study of the thermal stability or pyroelectric effect of titanium indiffused waveguides has been made by Bulmer²⁴. On z-cut LiNbO₃ Mach-Zehnder devices showed very large instabilities for small temperature changes and the voltage generated between the z-faces was measured at 274 V/°C, while Mach-Zehnder devices fabricated on x-cut LiNbO₃ showed much better thermal stability. Directional couplers fabricated on z-cut LiNbO₃ were less sensitive to pyroelectric instabilities than Mach-Zehnder devices and in general showed good stability. The decay in the coupler switching voltage and change in the interferometer phase bias indicated that the conductivity of LiNbO₃ was field-dependent.

$$\sigma = \sigma_0 + \sigma_1 E_0 \quad (2.2.4)$$

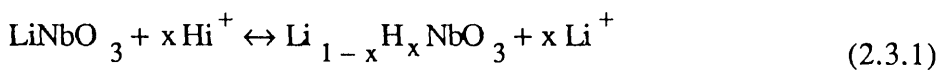
where σ_0 is the conductivity in the absence of an applied field, E_0 is the initial applied field and σ_1 is the field dependent component of the conductivity. The values of σ_1 for both x- and z-cut LiNbO₃ were determined to be range of 0 to 5x10⁻¹⁸ (ΩV)⁻¹.

Optical losses in slab guides have been attributed to in-plane scattering²⁵ from refractive index inhomogeneities, surface roughness and possibly strain and dislocations induced in the crystal during the indiffusion¹¹. Singh et al²⁵ has shown that the surface roughness is inversely proportional to the square root of the diffusion time, while the in-plane scattering initially decreases and then increases, with the optimum diffusion time being dependent upon the film thickness. The in-plane scattering from guides fabricated with short diffusion times or a thick initial titanium film thickness where a significant oxide layer will be left on the surface can be reduced by polishing the surface of the substrate.

2.3 The proton-exchange process.

Proton-exchange using benzoic acid was first demonstrated by Jackel et al²⁶ in 1982 and has since received much attention as an alternative method to titanium-indiffusion for fabricating waveguides. Proton-exchange developed from earlier work on ion exchange involving AgNO₃²⁷ and TlNO₃²⁸ melts. The ion-exchange process resulted in generally unreproducible high index guides and this was initially believed to be due to an exchange between the lithium ions and Ag or Tl ions. The index change was later recognised to be due to an exchange process between hydrogen ions (protons) from water impurities in the molten salts and the lithium ions²⁹. A number of acids have been used as a source for the hydrogen in the proton-exchange process, benzoic acid (C₆H₅CO₂H) being the most widely used since it has a large working temperature range, low toxicity and is inexpensive. The large working temperature range of benzoic acid, with a melting point of 122°C and a boiling point of 249°C, allows for easy control of the extent of the exchange and of the profile of the exchanged region, which are dependent upon both time and temperature.

During the exchange process, some or all of the lithium ions in the substrate are exchanged for protons (hydrogen ions from the acid). The hydrogen ions occupying the substitutional site of the lithium ions result in the partial formation of HNbO₃, which has a cubic perovskite crystal structure. The proton-exchange process can be described as :



The extent of the transformation of the crystal structure from rhombohedral to the cubic is apparently dependent upon several factors including the form of the LiNbO₃, i.e. whether it is a single crystal substrate or powder³⁰ and possibly the acid used, i.e. ortho- or pyrophosphoric acid have recently been researched as an alternative to benzoic acid³¹. This transformation results in a waveguiding region with a nearly step-index profile and with an increase in the extraordinary index, $\Delta n_e \approx 0.12$, and a slight decrease in the ordinary index, $\Delta n_o \approx -0.02$. In a comparison with titanium-indiffused waveguides, Becker reported a reduction in the photorefractive effect for the proton-exchange waveguides with no observed photovoltaic effect¹⁹. From comparisons of crystal composition of proton-exchanged lithium niobate powder and index

profiles for exchanged layers, Jackel et al³² has suggested that Δn_e is not linearly dependent upon x in $\text{Li}_{1-x}\text{H}_x\text{NbO}_3$ except for small values of x and saturates for $x=0.30$.

A number of problems have been associated with the use of pure benzoic acid including:

- A) observed index instabilities by Yi-Yan³³. It was suggested that the evolution of the magnitude of the waveguide index with time may be attributed to a continuous migration of the protons within the exchanged region.
- B) a DC extinction effect observed by Wong et al³⁴ who speculated that the effect is associated with ionic conductivity by the low-mass protons in the exchanged region.
- C) a reduced electrooptic effect was observed by Becker whilst comparing interferometric modulators fabricated by titanium-indiffusion and proton-exchange³⁵.
- D) severe etching of the substrate faces on Y-cut LiNbO_3 was reported by De Micheli³⁶.

Some of these problems can be overcome by post-annealing or by reducing the rate of proton-exchange, which is dependent upon the concentration of solvated protons available at the LiNbO_3 surface and the rate of diffusion into the melt of lithium ions³⁷. The use of post-annealing increases the depth and alters the refractive index profile of the waveguiding region from the step-index profile to a graded-index profile. The change in profile is dependent upon the annealing temperature, the time and the atmosphere in which the annealing is conducted^{38,47}. The change in profile from a very shallow step index to a deeper graded index is required to prevent field mis-match between the guides and single mode fibres. Post-annealing also reduces the index instabilities³⁹ reported by Yi-Yan. There has also been a considerable increase reported in the electrooptic efficiency of proton-exchange guides after annealing^{40,41}. The results of Rutherford back-scattering spectrometry (RBS) experiments on proton-exchanged waveguides reveal a relaxation in the lattice strain⁴² in the exchanged region which may account for much of the improvements reported above.

The simplest and most popular method to reduce the net rate of exchange is by introducing extra lithium ions into the protonic source. Lithium benzoate has been extensively used as a dilutant for benzoic acid. The percentage that the benzoic acid is diluted by the addition of the lithium benzoate is defined by

$$X = \frac{\text{No. of moles of lithium benzoate}}{\text{No. of moles of benzoic acid} + \text{No. of moles of lithium benzoate}} \times 100\% \quad (2.3.2)$$

Jackel et al³² reported no etching damage on y-cut LiNbO₃ which had been proton-exchanged in a 1% dilute melt for 1 hour at 220 °C and suggested that the etching may therefore be concluded to be due to a high concentration of hydrogen near the surface of the substrate, resulting in large changes in lattice dimensions. Loni et al⁴¹ reported waveguides with a substantially restored electrooptic effect ($R_{33}=24 \times 10^{-12}$ m/V) and very low-losses (0.2 dB/cm) fabricated using both a dilute melt and post-annealing. Rottschalk et al⁴³ also reported a substantial increase in the electrooptic coefficient of waveguides fabricated in 1% dilute benzoic acid but only after annealing, when the figure increases from 2.0×10^{-12} m/V to 19.8×10^{-12} m/V. De Micheli et al⁴⁴ used a double proton-exchange process where the same area was proton-exchanged twice with different exchange conditions. The superposition process results in low-loss guides (0.3 dB/cm) with very low inter-mode coupling but, being strongly multi-moded, the guides are not suitable for all purposes, i.e directional couplers, Mach-Zehnders, coupling to single mode fibres etc. The double proton-exchange process can also be used to form a quasi-embedded guide. An alternative method reported by De Micheli et al⁴⁵ used proton-exchange in benzoic acid diluted with lithium benzoate at high temperatures (300 °C) to fabricate the guides. In order to carry out proton-exchange at temperatures above the boiling point of benzoic acid, the LiNbO₃ crystal and the acid were sealed inside an hourglass-shaped phial. The shape of the phial allowed the sample to be kept separate from the acid until the exchange temperature had been reached, although it was still exposed to the acidic vapour which may have resulted in partial proton-exchange before the sample was immersed in the acid. The high temperature exchange has been found to reduce the in-plane scattering. Rutherford backscattering spectroscopy showed a reduction in the crystalline disorder with increasing exchange temperature and also showed that proton-exchange at 300 °C results in the same backscattering spectrum as for

unexchanged samples. A trend of increasing stability with increasing lithium benzoate concentrations in the melt was also observed.

Several methods have been used to characterise the exact structural changes which occur during the exchange and post-annealing processes. Although optical measurements are useful for characterising the stability and profile of the exchanged region, other analytical techniques are required to understand the origin of the index change leading to waveguiding and the effect that annealing or different dilutions of benzoic acid have on the proton-exchanged region. Canali et al⁴⁶ used Rutherford backscattering spectrometry (RBS), nuclear reactions, secondary ion mass spectrometry, scanning electron microscopy and x-ray diffraction to measure the atomic composition profiles and lattice distortions on substrates which had been proton-exchanged in pure benzoic acid. They established from the ion beam techniques and the x-ray diffraction methods that the hydrogen depth-profile typically had a step-like profile, in agreement with the refractive index profile. The hydrogen concentration was estimated to lie between 1.1 and 1.3×10^{22} atoms/cm³, corresponding to an exchange of about 65-75 % of the lithium atoms. Loni et al⁴⁷ used infrared spectroscopy to monitor the isotopic exchange of [¹H] and [²H] and atomic absorption spectroscopy to establish the concentration of lithium present in the molten benzoic acid after exchange with z-cut LiNbO₃. The lithium concentrations measured agreed with the expected concentrations of hydrogen in the exchanged region. It was concluded from the infrared spectroscopy work that the uptake of hydrogen as hydroxyl groups merely provides a means of charge compensation, while the lithium depletion determines the refractive index, but no other experimental evidence has appeared so far to prove conclusively that this is the case. The use of infrared absorption has also shown the presence of a broad unpolarised peak shifted towards lower frequency from a sharp polarised peak at 3510 cm^{-1} which corresponds to the free OH group. This broad peak is due to the presence of a hydrogen-bonded OH group⁴⁸, a hydrogen ion sharing its bond with two oxygen ions. Rice et al used x-ray diffraction on LiNbO₃ powder that had been proton-exchanged to establish three distinct rhombohedral phases in $\text{Li}_{1-x}\text{H}_x\text{NbO}_3$ for $x \leq 0.75$. Since LiNbO₃ powder was used in the proton-exchange, the results could be very different from those which would have resulted from a LiNbO₃ substrate. The hydrogen content of the powders was determined by measuring the weight change due to water loss when the materials were heated to 800-1000°C. Samples with $0.65 < x < 0.75$ were found to have a reversible transition between different rhombohedral phases at

approximately 150 °C, explaining why samples exchanged in pure benzoic acid were susceptible to index instabilities before annealing. Minakata³⁰ used x-ray rocking curve analysis to measure lattice constants on z-cut LiNbO₃ exchanged in dilute benzoic acid. He was able to conclude that the strain $\Delta c/c$ was extremely large, +0.45%, and had little dependence upon the proton-exchange conditions, while the strain $\Delta a/a$ was negligible. X-ray diffractometry on x-cut LiNbO₃ substrates indicated that the proton-exchanged region had undergone a positive lattice strain $\Delta a/a$ of about 0.8%. Campari et al⁴⁹ used x-ray diffraction rocking curve analysis on y-cut LiNbO₃, where a $\Delta a/a$ strain as large as 1.56% was measured and considered to be responsible for the surface damage observed in proton-exchanged y-cut LiNbO₃. Canali et al⁴⁶ have pointed out that the lattice strain observed is a function of the substrate orientation and will strain in the direction of the crystal cut.

Proton-exchange has also been used in combination with titanium-indiffusion to produce waveguides that are capable of supporting both TE and TM modes. The waveguide is fabricated by proton-exchange on top of a planar or strip waveguide fabricated by titanium-indiffusion on the LiNbO₃ substrate^{36,50}. The resulting guides are referred to as TIPE guides and have several potential advantages over either of the individual methods. Since proton-exchange decreases the ordinary refractive index, buried titanium diffused waveguides can be fabricated on a z-cut LiNbO₃ substrate for TE polarisation or on a x- or y-cut LiNbO₃ substrate for TM polarisation. The surface damage associated with the proton-exchange of y-cut LiNbO₃ is remedied by firstly titanium indiffusing the surface although the use of annealing is more effective. The combination of the two processes also allows tailoring of the waveguide birefringence. Li et al⁵¹ have also reported a similar device combining double proton-exchange with titanium-indiffusion (Titanium-Indiffusion Double Exchange, TIDE) to produce waveguides with lower loss than TIPE guides fabricated with a single exchange.

Although a great deal of work is still required before the nature of the proton-exchange process is fully understood, the benefits of a relatively large Δn_e and little optical damage have already been well exploited, but still mainly at the research level. There has been a considerable reported number of active and passive devices fabricated using proton-exchange. The high index change makes proton-exchange ideal for various types of gratings and planar lenses^{52,53,54,55}. The decrease in the ordinary refractive index has been exploited to fabricate

polarisers⁵⁶, see Fig. 2.2. A titanium indiffused guide is fabricated with a gap in the guide. The guide is then joined by a section of proton-exchanged guide. On z-cut LiNbO₃, both the TE and the TM modes will be guided by the titanium indiffused guide but only the TM mode will be guided by the proton-exchanged region. A TE polariser can be fabricated on x-cut LiNbO₃ in the same manner. Findakly reported a polariser fabricated using this method with an extinction ratio of 32 dB and an excess loss of 0.8 dB.

Active devices fabricated using proton-exchanged waveguides include phase-modulators^{34,30}, a Mach Zehnder interferometer³⁵, acousto-optic devices⁵⁷, an interferometric temperature sensor⁵⁸ and an acousto-optic TM-TE mode convertor fabricated with a TIPE waveguide⁵⁰. There has also been a recent increase in interest in the use of proton-exchanged guides for second harmonic generation (SHG). Arvidsson et al⁵⁹ have used proton-exchanged guides to achieve efficient second harmonic generation in the form of Cerenkov radiation of 0.84 μm radiation and 1.06 μm radiation, see Fig. 2.3. The conversion efficiency for Cerenkov SHG is dependent upon the field overlap between the fundamental and the harmonic modes, which is relatively well satisfied using the tight optical confinement achieved by proton-exchange. Keys et al⁶⁰ used a Q-switched Nd:YAG laser to characterise the proton-exchanged waveguides for SHG by making use of the high peak powers whilst the low average powers meant that optical damage was not a problem.

Alternative acids to benzoic acid are available that are capable of fabricating guides by proton-exchange. Of these pyrophosphoric⁶¹ and orthophosphoric³¹ acid have recently received increasing interest.

In conclusion, the various methods available for fabricating waveguides have not yet yielded one distinctive method which can be considered superior to the others in all respects. Titanium-indiffusion provides guides with no significant reduction in the electrooptic efficiency but only a small change in both the extraordinary and ordinary refractive index, while also increasing the susceptibility to optical damage via the photoconductive effect. Proton-exchange provides guides with a large change in the extra-ordinary refractive index and a significant decrease in the degree of optical damage, but large reductions in the electrooptic efficiency have been reported. Recently reported proton-exchange techniques led to a substantial restoration of the electrooptic coefficients whilst maintaining the advantages normally associated with proton-exchanged

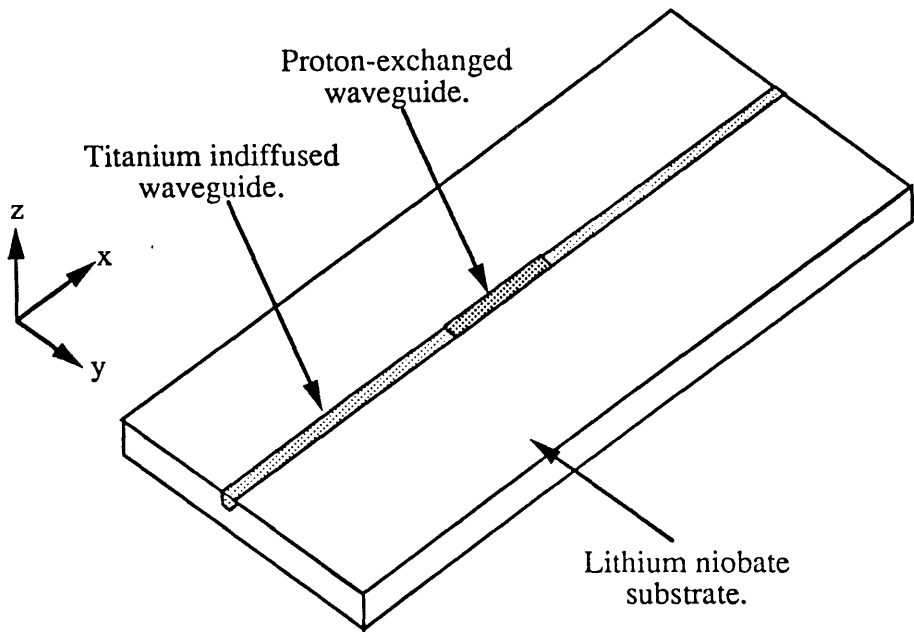


Fig. 2.2. TE extinction polariser fabricated on a z-cut lithium niobate substrate. A TM extinction polariser would be fabricated on x- or y-cut lithium niobate

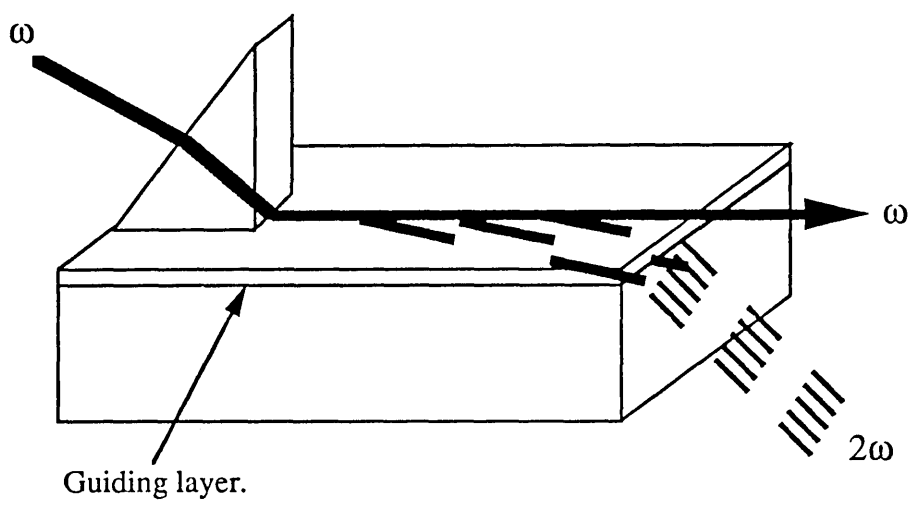


Fig. 2.3. Second harmonic generation.

waveguides. Both the titanium-indiffusion and the proton-exchange techniques were used in the fabrication of the transverse electrooptic phase modulator. The specific fabrication procedures used are described in detail in chapter 3.

References.

1. Kaminow I. P. and Carruthers J. R. "Optical waveguiding layer in LiNbO_3 and LiTaO_3 ." *Appl. Phys. Lett.* **22**. April 1973. pp 326-328.
2. Schmidt R. V. and Kaminow I. P. "Metal-diffused optical waveguides in lithium niobate", *Appl. Phys. Lett.* **24**. 1974. pp 458-460.
3. Destefanis G. M., Gailliard J. P., Ligeon E. L., Vallette S., Farmery B.W, Townsend P. D. and Perez A. "The formation of waveguides and modulators in LiNbO_3 by ion implantation", *J. Appl. Phys.* **50**. 1979 pp 7898-7905.
4. Jackel J. L., Rice C. E. and Veselka J.J. "Proton-exchange for high-index waveguides in LiNbO_3 ", *Appl. Phys. Lett.* **41**. October 1982. pp 607-608.
5. Holman R. L., Cressman P. J. and Revelli J. F. "Chemical control of optical damage in lithium niobate", *Appl. Phys. Lett.* **32**. 1978. pp 280-283.
6. McLachlan A. D., "Theoretical and experimental investigations of titanium diffused lithium niobate optical waveguides", PhD. Thesis. 1981. Glasgow University.
7. Rice C. E. and Holmes R. J. "A new rutile structure solid-solution phase in the LiNb_3O_8 - TiO_2 system, and it's role in Ti diffusion into LiNbO_3 ", *J. Appl. Phys.* **60**. December 1986. pp 3836-3839.
8. Armenise M. N., Canali C., De Sario M., Carnera A., Mazzoldi P., and Celotti G. "Characterization of TiO_2 , LiNb_3O_8 and $(\text{Ti}_{0.65}\text{Nb}_{0.35})\text{O}_2$ compound growth observed during $\text{Ti}:\text{LiNbO}_3$ optical waveguide fabrication", *J. Appl. Phys.* **54**. November 1983 pp 6223-6231.
9. Canali C., Carnera A., Mazzoldi P. and De La Rue R. M. " LiNbO_3 optical waveguide fabrication by Ti indiffusion and proton exchange : process, performances and stability", *SPIE Proc.* **517**. 1984 pp 119-127.

10. Esdaile R. J. "Titanium-doped LiNbO₃ for electrooptic devices." Ph.D Thesis, University of Glasgow. 1979.
11. Twigg M. E., Maher D. M., Nakahara S., Sheng T. T and Holmes R. J. "Study of structural faults in Ti-diffused lithium niobate", Appl. Phys. Lett. **50**. March 1987. pp 501-503.
12. Ctyroky J., Hofman M., Janta J. and Schrofel J. "3-D analysis of Ti:LiNbO₃ channel waveguides and directional couplers", IEEE J. Quantum Electron. **QE-20**. April 1984. pp 400-409.
13. Burns W. K., Klein P. H., West E. J. and Plew L. E.. "Ti diffusion in Ti:LiNbO₃ planar and channel optical waveguides", J. Appl. Phys. **50**. October 1979. pp 6175-6182.
14. Holmes R. J. and Smyth D. M. "Titanium diffusion into LiNbO₃ as a function of stoichiometry", J. Appl. Phys. **55**. May 1984. pp 3531-3535.
15. Hocker G. B. and Burns W. K. "Mode dispersion in diffused channel waveguides by the effective index method", Appl. Opt. **16**. January 1977. pp 113-118.
16. Strake E., Bava G. P. and Montrosset I. "Guided modes of Ti:LiNbO₃ channel waveguides: A novel quasi-analytical technique in comparison with the scalar finite-element method", J. Lightwave Tech. **6**. June 1988. pp 1126-1135.
17. Chen B. and Pastor A. C. "Elimination of LiO₂ out-diffusion waveguide in LiNbO₃ and LiTaO₃", Appl. Phys. Lett. **30**. June 1977 pp 570-571.
18. Jackel J. L., Glass A. M., Peterson G. E., Rice C. E., Olson D. H. and Veselka J. J. "Damage resistant LiNbO₃ waveguides", J. Appl. Phys. **55**. January 1984. pp 269-270.
19. Becker R. A. "Methods of characterizing photorefractive susceptibility of LiNbO₃ waveguides", SPIE Proc. **578**. 1985. pp 12-18.

20. Schmidt R. V., Cross P. S. and Glass A. M. "Optically induced crosstalk in LiNbO₃ waveguide switches." J. Appl. Phys. **51**. January 1980. pp 90-93.
21. Harvey G. T. "The photorefractive effect in directional coupler and Mach-Zehnder LiNbO₃ optical modulators at a wavelength of 1.3 μm", J. Lightwave Tech. **6**. June 1988. pp 872-876.
22. Ashkin A., Boyd G. D., Dziedzic J. M., Smith R. G., Ballman A. A., Levinstein J. J. and Nassau K. "Optically induced refractive index inhomogeneities in LiNbO₃ and LiTaO₃." Appl. Phys. Lett. **9**. July 1966. pp 72-74.
23. Becker R. A. and Williamson R. C. "Photorefractive effects in LiNbO₃ channel waveguides: Model and experimental verification", Appl. Phys. Lett. **47**. November 1985. pp 1024-1026.
24. Bulmer C. H. "Pyroelectric effects in LiNbO₃ channel-waveguide devices", Appl. Phys. Lett. **48**. April 1986. pp 1036-1038.
25. Singh J. and De La Rue R. M. "An experimental study of in plane scattering in titanium diffused y-cut LiNbO₃ optical waveguides", J. Lightwave Tech. **LT-3**. February 1985. pp 67-76.
26. Jackel J. L., Rice C. E. and Veselka J.J. "Proton exchange for high-index waveguides in LiNbO₃", Appl. Phys. Lett. **47**. October 1982. pp 607-608.
27. Shah M. L. "Optical waveguides in LiNbO₃ by ion exchange technique", Appl. Phys. Lett. **26**. June 1975. pp 652-653.
28. Jackel J. "High-Δn optical waveguides in LiNbO₃: Thallium-lithium ion exchange", Appl. Phys. Lett. **37**. October 1980. pp 739-741.
29. Jackel J. L. and Rice C. E. "Variation in waveguides fabricated by immersion of LiNbO₃ in AgNO₃ and TlNO₃: the role of hydrogen", Appl. Phys. Lett. **41**. September 1982. pp 508-510.

30. Minakata M., Kumagi K. and Kawakami S. "Lattice constant changes and electrooptic effects in proton-exchanged LiNbO₃ optical waveguides", *Appl. Phys. Lett.* **49**. October 1986. pp 992-994.
31. Loni A., Keys R. W., De La Rue R. M., Foad M. A. and Winfield J. M. "An optical characterisation of z-cut proton-exchanged LiNbO₃ waveguides fabricated using orthophosphoric and pyrophosphoric acid." submitted for publication.
32. Jackel J. L., Rice C. E. and Veselka J. J. "Composition control in proton-exchanged LiNbO₃", *Electron. Lett.* **19**. May 1983. pp 387-388.
33. Yi-Yan A. "Index instabilities in proton-exchanged LiNbO₃ waveguides", *Appl. Phys. Lett.*, **42**. April 1983. pp 633-635.
34. Wong K. K. and De La Rue R. M. "Electro-optic-waveguide frequency translator in LiNbO₃ fabricated by proton exchange", *Opt. Lett.* **7**. November 1982. pp 546-548.
35. Becker R. A. "A comparison of guided-wave interferometric modulators fabricated on LiNbO₃ via Ti indiffusion and proton exchange." *Appl. Phys. Lett.* **43**. July 1983. pp 131-133.
36. De Micheli M., Botineau J., Sibillot P., Ostrowsky D. B. and Papuchon M. "Fabrication and characterization of titanium indiffused proton exchanged (TIPE) waveguides in lithium niobate", *Opt. Comm.* **42**. June 1982. pp 101-103.
37. Wong K.K "An experimental study of dilute melt proton exchange waveguides in X- and Z-cut lithium niobate", *GEC J. Research.* **3**. 1985. pp 243- 249.
38. De Micheli M., Botineau J., Neveu S., Sibillot P. and Ostrowsky D. B. "Independent control of index and profiles in proton-exchanged lithium niobate guides", *Opt. Lett.* **8**. February 1983. pp 114-115.

39. Jackel J. L. and Rice C. E. "Short- & long-term stability in proton-exchanged lithium niobate waveguides", SPIE Proc. **460**. Guided wave and optoelectronic materials, 1964. pp 43-48.
40. Suchoski P. G., Findakly T. K. and Leonberger F. J. "Stable low-loss proton exchanged LiNbO₃ waveguide devices with no electrooptic degradation", Opt. Lett. **13**. November 1988. pp 1050-1052.
41. Loni A., De La Rue R. M. and Winfield J. M. "Very low loss proton-exchange waveguides with a substantially restored electrooptic effect." Paper MD-3, Topical meeting on Integrated and guided wave optics, March 28-30, New Mexico, 1988, Opt. Soc. America (Washington).
42. Al-Shukri S. M., Dawar A. L., De La Rue R. M., Nutt A. C. G., Taylor M. R. S. and Tobin J. R. "Analysis of annealed proton-exchanged waveguides on Lithium Niobate by optical waveguide measurements and microanalytical techniques", Proc. 7th Topical Meeting on Integrated and Guided Optics, Florida, 24-26 April 1984, PD7/1.
43. Rottschalk M., Rasch A. and Karthe W. "Electrooptic behaviour of proton exchanged LiNbO₃ optical waveguides." J. Opt. Commun. **9**. 1988 pp 19-23.
44. De Micheli M., Li M. J., Ostrowsky D. B. and Papuchon M. "The double proton exchange in LiNbO₃ : low loss and quasi-embedded waveguides", Proc 4th European Conference on Integrated Optics (Glasgow) May 1987. pp 62-65.
45. De Micheli M., Ostrowsky D. B., Barety J. P., Canali C., Carnera A., Mazzi G. and Papuchon M. "Crystalline and optical quality of proton exchanged waveguides", J. Lightwave Tech. **LT-4**. July 1986. pp 743-745.
46. Canali C., Carnera A., Della Mea G., Mazzoldi P., Al Shukri S. M., Nutt A. C. G. and De La Rue R. M. "Structural characterization of proton

exchanged LiNbO₃ optical waveguides”, J. Appl. Phys. **59**. April 1986 pp 2643-2649.

47. Loni A., De La Rue R. M. and Winfield J. M. “Proton-exchanged, lithium niobate planar-optical waveguides: Chemical and optical properties and room-temperature hydrogen isotopic exchange reactions”, J. Appl. Phys. **61**. January 1987. pp 64-67.
48. Loni A., Hay G., De La Rue R. M. and Winfield J. M. “Proton-exchanged LiNbO₃ waveguides: The effects of post-exchange annealing and buffered melts as determined by infrared spectroscopy, optical waveguide measurements, and hydrogen isotopic exchange reactions.” J. Lightwave Tech. **7**. June 1989. pp 911-919.
49. Campari A., Ferrari C., Mazzi G., Summonte C., Al-Shukri S. M., Dawar A., De La Rue R. M. and Nutt A. C. G. “Strain and surface damage induced by proton exchange in y-cut LiNbO₃.” J. Appl. Phys. **58**. Dec. 1985. pp 4521-4524.
50. Hinkov V. P. “Collinear acoustooptical TM-TE mode conversion in proton exchanged Ti:LiNbO₃ waveguide structures”, J. Lightwave Technol. **6**. June 1988. pp 903-908.
51. Li M. J., De Micheli M., Ostrowsky D. B. and Papuchon M. “High index low loss LiNbO₃ waveguides”, Opt. Comm. **62**. April 1987. pp 17-20.
52. Warren C. “Double ion-exchanged chirp grating lens in lithium niobate waveguides”, Appl. Phys. Lett. **43**. 1983. pp 424-426.
53. Suhara T., Fujiwara S. and Nishihara H. “Proton-exchanged fresnel lenses in Ti:LiNbO₃ waveguides”, Appl. Opt. **25**. October 1986. pp 3379-3383.
54. Zang D. Y. and Tsai C. S. “Titanium-indiffused proton-exchanged waveguide lenses in LiNbO₃ for optical information processing”, Appl. Opt. **25**. 1983. pp 2264-2271.

55. Yu Z. D. "Waveguide optical planar lenses in lithium niobate- theory and experiments", *Opt. Commun.* **47**. Sept. 1983. pp 248-250.
56. Findalky T. and Chen B. "Single-mode transmission selective integrated-optical polarisers in LiNbO₃ ", *Elec. Lett.* **20**. February 1984. pp 128-129.
57. Duffy J. F., Al-Shukri S. M. and De La Rue R. M. "Guided-wave acousto-optic interaction on proton-exchanged lithium tantalate", *Elec. Lett.* **23**. July 1987. pp 849-850.
58. Haruna M. "Optical π -arc waveguide interferometer for temperature sensing", *Appl. Opt.* **24**. 1985. pp 2483-2484.
59. Arvidsson G., Laurell F., Jaskorzynska B., Webjorn J., Loni A., Keys R. W. and De La Rue R. M. "Influence of annealing on the conversion efficiency for SHG by Cerenkov radiation from proton-exchanged LiNbO₃ waveguides." Paper TuA3, Topical meeting on Nonlinear guided wave phenomenon: Physics and Applications, Houston, Texas, Feb. 1989, Opt. Soc. America (Washington).
60. Keys R. W., Loni A. and De La Rue R. M. "Characterisation of proton-exchanged waveguides for second harmonic generation using Q-switched Nd:YAG laser pulses." *IEE Appl. of Ultrashort Pulses for Optoelectronics*. Digest No. 1989/87. May 1989. pp 1-4.
61. Goto N. and Yip G. L. "Characterisation of proton-exchanged and annealed LiNbO₃ waveguides with pyrophosphoric acid. " *Appl. Opts.* **28** Jan. 1989 pp 60-65.

Chapter 3

Fabrication of the transverse electrooptic modulator.

3.1 Introduction.

The fabrication of the transverse electrooptic modulator required the development of a novel technique based on existing photolithographical and polishing techniques. The central problem was the fabrication of a thin wafer of LiNbO_3 , less than twenty micrometres thick, with a strip waveguide and a pair of electrodes on opposite faces of the LiNbO_3 substrate and straddling the waveguide. Due to the fragility of the LiNbO_3 wafer after it had been thinned to thicknesses of less than a couple of hundred micrometres and the subsequent difficulty in handling the sample during any fabrication steps, it was necessary to carry out most of the photolithography before substrate thinning. A glass substrate was used to support the LiNbO_3 substrate during and after thinning. Ion-driven techniques, such as reactive ion etching and ion beam milling, have been used to fabricate structures in LiNbO_3 , e.g. grooves for fibre-guide alignment¹, fresnel lenses² and ridge waveguides³ but the typical etch rates of 0.01-0.1 $\mu\text{m}/\text{min}$ prevents the use of such techniques to thin a 1 mm substrate to less than 20 μm . A recently reported technique uses laser-driven chemical reactions⁴ to achieve an etch rate greater than 10 $\mu\text{m}/\text{min}$, but difficulty in the control of the etching still prevents this technique being used in the present problem. Therefore, the use of mechanical lapping and polishing was the only apparent method by which the substrate could be thinned to the required thickness. The finished device must also allow efficient launching of light into the waveguide and contact to be made to both electrodes.

The use of a transverse electric field, together with the electrooptic coefficients of LiNbO_3 , determined the use of z-cut material to obtain the maximum electrooptic effect through the R_{33} coefficient.

It was necessary firstly to establish an order for the fabrication steps. Ideally the sample wafer would firstly be thinned to the desired thickness, followed by electrode and waveguide fabrication. Since thinning was expected to be the hardest stage to develop and the electrode and waveguide fabrication could be regarded as standard, it would be desirable to avoid extensive fabrication till after the sample was thinned. A simpler alternative to the modulator structure

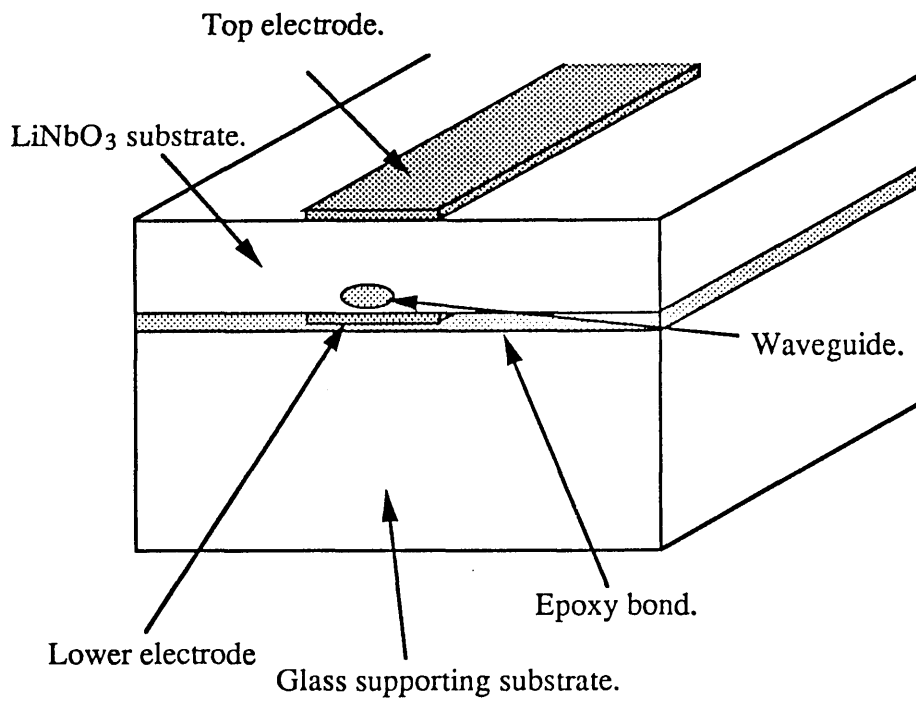


Fig. 3.1 The transverse electrooptic modulator.

shown in Fig. 3.1 could have been provided by fabricating a planar electrode on the supporting glass substrate and the fabrication of a waveguide and electrode on the top surface of the LiNbO₃ substrate after thinning, see Fig. 3.2. Unfortunately due to the high temperature involved in titanium indiffusion and the acidic medium used for proton-exchange, both waveguide fabrication techniques would almost certainly have destroyed the bond between the LiNbO₃ and the glass substrate. Alternatively the sample could be removed, following thinning, to allow fabrication of the waveguides and electrodes. This was attempted using both pink dental wax and several different epoxies to bond the sample during thinning. Although the sample wafers were thinned successfully it was not possible to remove any of the samples from the supporting substrate without destroying them. It was therefore necessary to fabricate the waveguide and lower electrode before thinning. This meant that the waveguide would have to be fabricated on the face which would be bonded to the supporting glass substrate and hence lie below the top surface of the finished device.

3.2 Waveguide fabrication.

Two methods for waveguide fabrication routinely used in the Electrical and Electronic Engineering Department at Glasgow University are titanium indiffusion and proton-exchange. Titanium indiffusion is relatively well established and documented whereas proton-exchange is still a major area of research in its own right. An important objective of the investigation was the measurement of the electrooptic coefficients of both titanium indiffused waveguides, fabricated by a standard technique, and proton-exchange waveguides fabricated by a technique described by Loni et al⁵ using dilute melt benzoic acid and annealing. It has been shown that this method of proton-exchange substantially restores the electrooptic effect and reduces the scattering normally associated with proton-exchange (see section 2.4).

3.2.1 The fabrication of titanium indiffused guides.

The fabrication steps for the titanium indiffused waveguides are shown schematically in Fig. 3.3. Before deposition of the titanium the substrates were thoroughly cleaned and coated with photoresist, which was photolithographically patterned. The substrate was cleaned using the following well established procedure:

1. Clean the substrate using soap and reverse osmosis (RO) water.

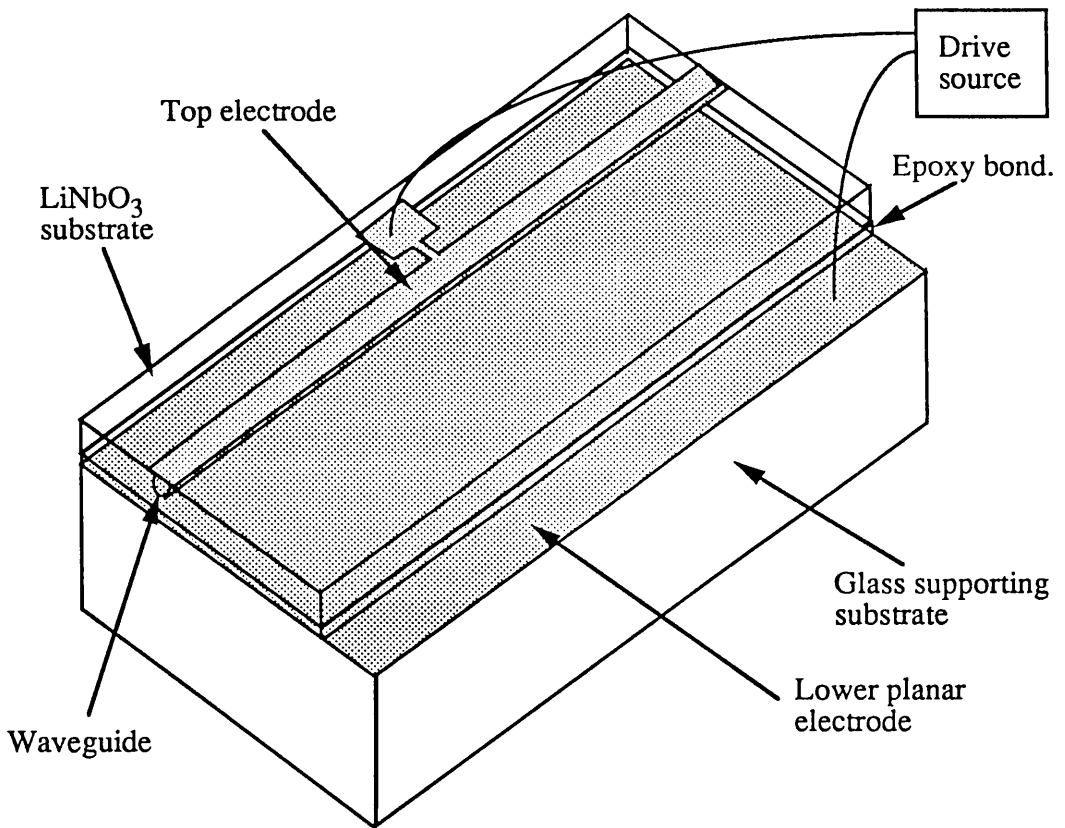


Figure 3.2. Alternative transverse electrooptic modulator with waveguide fabricated after thinning.

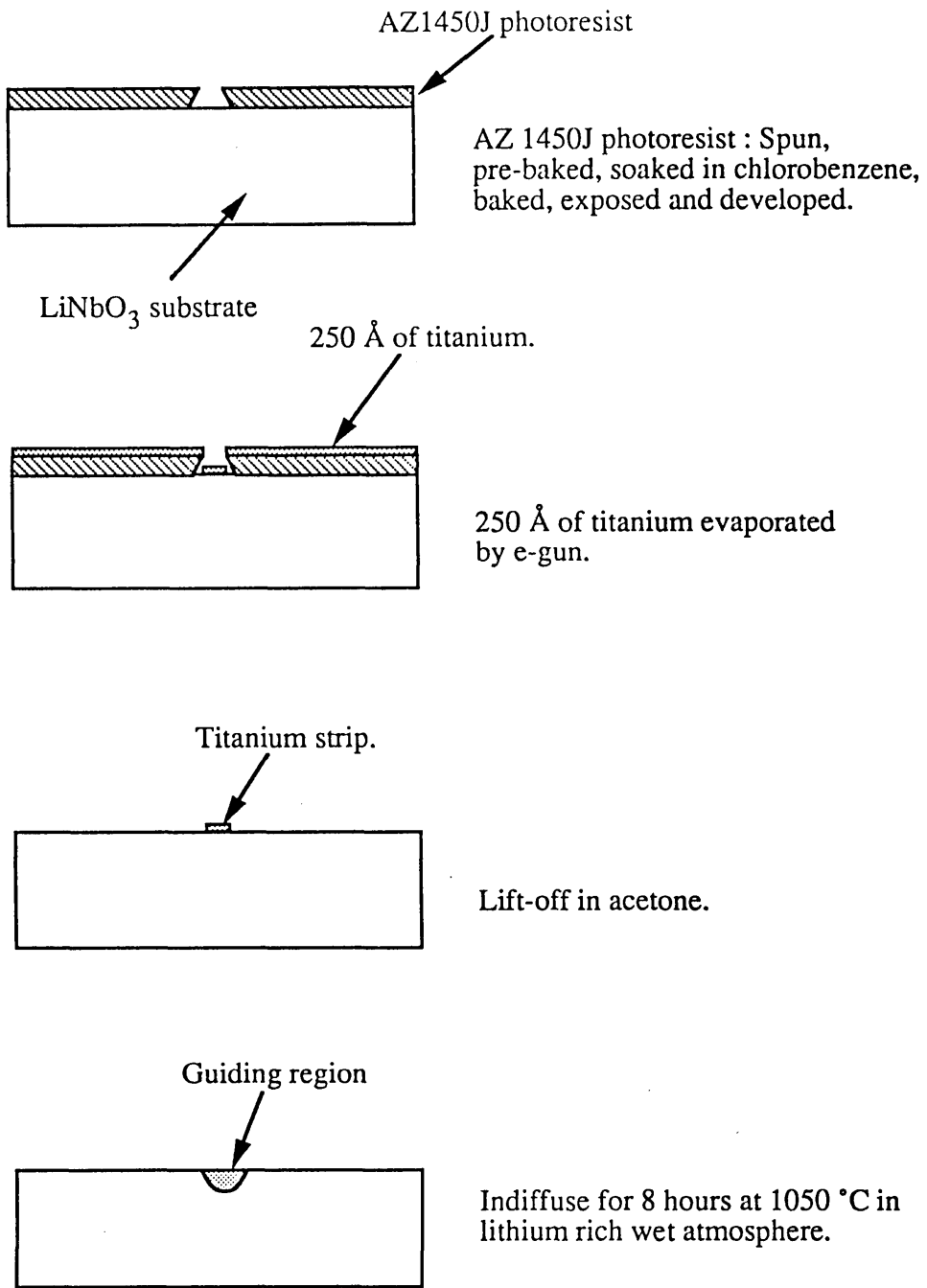


Fig. 3.3 Titanium indiffusion.

2. Place the substrate in a beaker of trichloroethanol and agitate in an ultrasonic bath for 5 minutes.
3. Transfer to a beaker of methanol and agitate in an ultrasonic bath for 5 minutes.
4. Repeat with a beaker of acetone.
5. Rinse the substrate in a beaker of RO water.
6. Remove excess water from the substrate with an air gun and place on a hot plate to dry completely.

The ferroelectric nature of LiNbO_3 implied the need for care during the cleaning procedure to avoid the electrostatic attraction of dust particles.

The photoresist was deposited onto the substrate using a syringe with a $0.3\ \mu\text{m}$ filter and the substrate was spun at 4000 rpm for 1 minute, leaving a $0.1\ \mu\text{m}$ thick layer of photoresist. Initially Shipley AZ1350J photoresist was used but this was later replaced by AZ1450J photoresist, which gave layers with fewer striations and left a smaller ridge of photoresist at the edges of the substrate after spinning. To harden the photoresist for exposure the substrate was baked for 30 minutes at $90\ ^\circ\text{C}$. Problems in achieving good and reproducible straight edges for the titanium strips following lift-off were resolved by soaking the substrate in chlorobenzene. The substrate was baked at $90\ ^\circ\text{C}$ for 15 minutes, removed, soaked in chlorobenzene for 15 minutes and then baked again at $90\ ^\circ\text{C}$ for a further 15 minutes. Soaking the substrate in the chlorobenzene created a harder layer of photoresist at the surface which caused it to be undercut at the edge of the developed strip. This greatly increased the ease with which the titanium on top of the photoresist was removed during lift-off and improved the quality of the titanium strip edges. Once the photoresist was baked it was patterned using a chrome mask, shown schematically in Fig. 3.4. This exposed strips of photoresist from 4 to $7\ \mu\text{m}$ wide and $10\ \text{mm}$ long. The complete pattern was $0.5\ \text{cm}$ wide, enabling five sets of guides to be produced on the one substrate. The strips of photoresist were removed on developing.

A nominal titanium thickness of between 25 and $30\ \text{nm}$ was evaporated using an electron-gun onto the negative face of z-cut LiNbO_3 . The thickness during evaporation was monitored using a quartz crystal thickness monitor and checked afterwards using a Talystep surface profile instrument. Since stripe waveguides were required a dark field mask was used so that, following lift-off, strips from 4 to $7\ \mu\text{m}$ wide of titanium were left. The titanium strips were indiffused for eight hours at $1050\ ^\circ\text{C}$ in a wet, lithium-rich, atmosphere. To

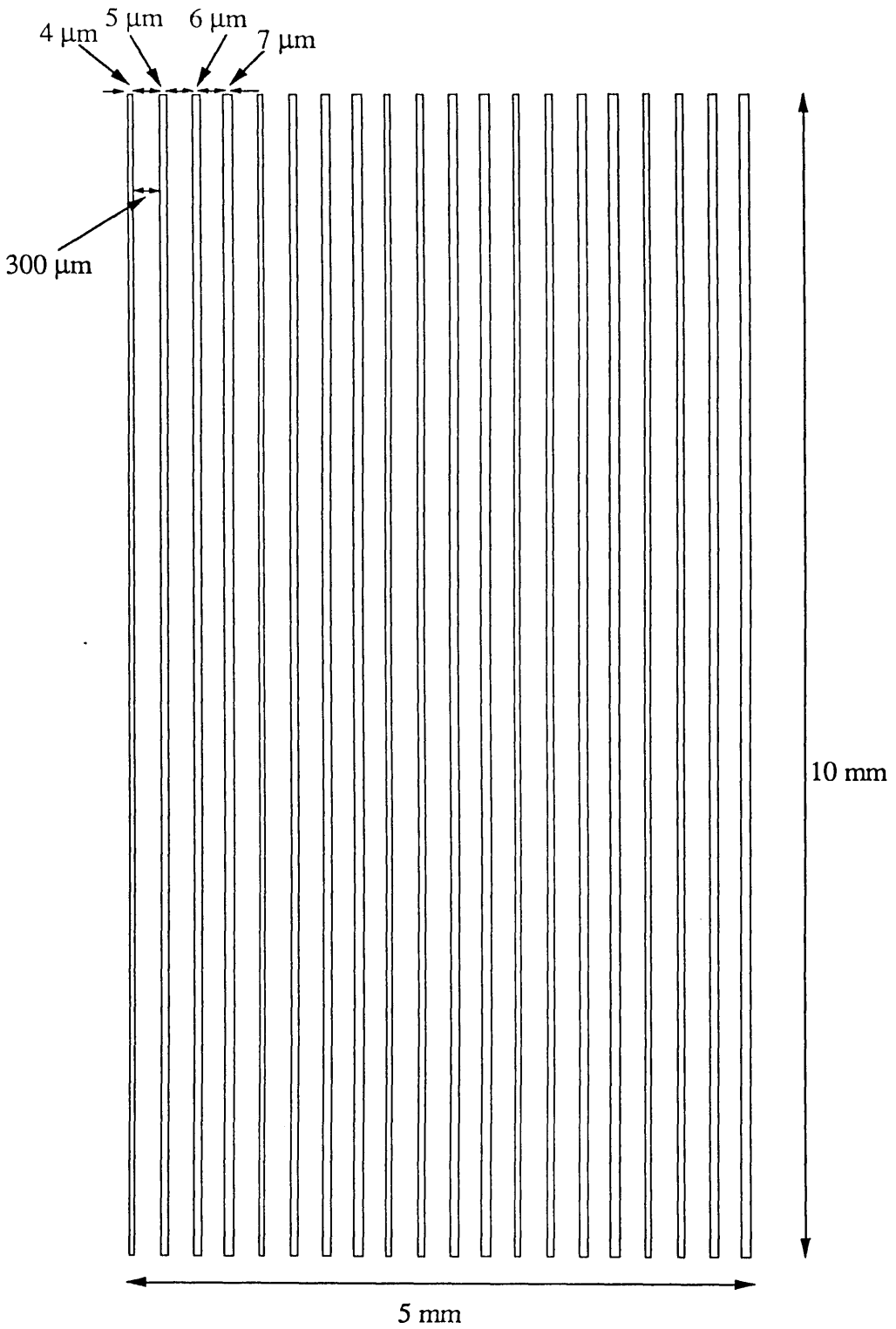
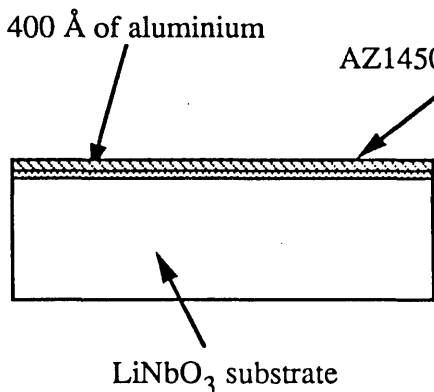


Fig. 3.4 Photolithographic mask used for titanium indiffused and proton exchange waveguides.

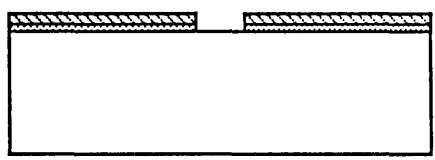
achieve this atmosphere, oxygen was bubbled through water at 50 °C before passing along the furnace tube over LiNbO₃ powder placed in front of the LiNbO₃ substrate. The substrate and the LiNbO₃ powder sat on platinum foil on top of a quartz boat. The foil material holding the substrate needed to be inert at very high temperatures (1050 °C) to ensure that there was no contamination of the substrate from the indiffusion of the foil material. The temperature profile of the furnace used had a relatively small hot spot, the length over which the maximum temperature is constant (less than ± 2 °C over 4 cm), this restricted the number of substrates that could be indiffused at one time. The temperature along the furnace had to be measured carefully so that the substrates could be placed accurately in the centre of the hot spot. A temperature variation of a few degrees could alter the refractive index profile of the indiffused waveguide along the length of the substrate.

3.2.2 The fabrication of proton-exchanged guides.

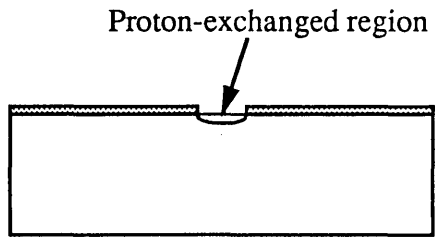
The fabrication steps for the proton-exchanged waveguides are shown schematically in Fig. 3.5. Proton-exchanged stripe waveguides were fabricated by masking the substrate with aluminium and then etching stripes in the aluminium mask to expose the region for proton-exchange. The substrates were cleaned using the method described above and then immediately placed in a thermal evaporator where they were coated with 40 nm of aluminium. The thickness of the mask was dependent upon the exchange time, a safe ratio to prevent proton-exchange of the surrounding substrate was found to be approximately 10 nm/min. After the substrates had been coated with aluminium they were coated with AZ1450J photoresist. The photoresist was exposed and developed using the same photolithographic mask that was used for the titanium indiffused waveguides. Stripe windows were formed in the aluminium by etching, while in the previous case stripes of titanium were formed by lift-off. The windows which defined the waveguides were etched by placing the substrate in a dish of aluminium etch, 16:1:3 of phosphoric acid : nitric acid : water, until all the aluminium had been removed from the developed stripe, approximately 5 minutes. The substrates were proton-exchanged by immersing in 1% dilute melt benzoic acid at 235 °C for 4 mins. The acid was prepared by carefully mixing pure benzoic acid with 1% molar weight lithium benzoate, this corresponds to an actual weight ratio of 94.78:1 of benzoic acid:lithium benzoate. Once the acid has been heated to 235 °C the substrates, held in PTFE holders, were immersed in quartz beakers containing the benzoic acid. To



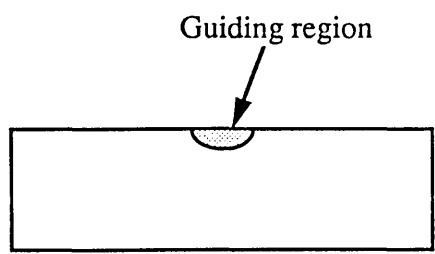
Evaporation of 400Å aluminium followed by the deposition of AZ1450J photoresist.



Exposure and development of the photoresist followed by immersion in aluminium etch.



Removal of photoresist followed by immersion in 1% dilute benzoic acid at 235 °C for 4 min.



Removal of aluminium mask followed by annealing at 375 °C for 45 min.

Fig. 3.5. Schematic representation of the fabrication steps involved in the fabrication of proton-exchanged waveguides.

prevent thermal shock damaging the substrates, they were held just above the acid for 15 seconds before being immersed. The benzoic acid was heated using an oil bath with the oil around the beakers being heated to 245 °C to compensate for a 10 °C temperature drop between the oil and the acid. On removal the substrates were allowed to cool for a short time before being rinsed in warm water and cleaned in acetone to remove any traces of the acid. The acid apparently continued to etch the aluminium mask even after cooling which would have prevented the alignment of the electrodes to the waveguides.

A problem with proton-exchanged waveguide device fabrication is that once the mask has been removed in the aluminium etch and the substrate has been cleaned thoroughly there is no evidence as to the position of the waveguides when the substrate is viewed through a standard microscope. Since no alignment marks were used, the uniform appearance of the LiNbO₃ sample surface created a severe problem when aligning the mask for the electrodes. Several different approaches were tried where the mask was not removed immediately after the proton-exchange, see section 3.4. Regardless of the method used to assist in the alignment of the electrode mask, the proton-exchanged region was not capable of guiding until the substrate had been annealed because of the particular choice of initial fabrication conditions.

In the proton-exchange method described by Loni et al⁵ the substrates were annealed in several stages in order to monitor how the guide properties, attenuation and electrooptic coefficients altered with time and temperature. Immediately following proton-exchange the substrates were unable to support any guiding. The substrates were then annealed for 30 min at 275 °C, after which there was little change in the guiding. A second anneal at 375 °C for 15 min produced a substantial reduction in propagation loss and improvement in the electrooptic coefficients. Initial guides for characterisation using the transverse electrooptic modulator were fabricated using exactly the same sequence of steps as described by Loni⁵. It soon became obvious that it was mainly the high temperature annealing that was responsible for the improvement in the propagation losses and electrooptic coefficients. The first low temperature annealing stage was therefore dropped. Annealing for 30 min at 375 °C provided guides with very poor confinement of the light, although showing an improvement from the 30 min. anneal at 275 °C, while guides with good confinement resulted from annealing at 375 °C for 45 min. The substrates were introduced and removed from the furnace by slowly moving along the furnace

tube (1 min for 16 cm) to prevent thermal shock. The temperature controller for the annealing furnace was calibrated for the central hot spot. To ensure the correct diffusion temperature, with the given size of the hot spot, meant that not more than two substrates could be annealed at a time. To reduce the effect of any optical damage on the waveguides they were annealed in a wet oxygen atmosphere. Pure O₂ was passed along the furnace tube after bubbling through water heated to 70 °C.

3.3 Buffer layer.

In order to prevent the substantial attenuation of TM polarised light associated with a metal boundary⁶ a buffer layer of silicon dioxide was deposited prior to the aluminium electrodes. A buffer layer thickness of 200 nm was used to prevent the evanescent tail of the TM field reaching the metal boundary. The thickness of the buffer layer chosen was based upon attenuation measurements by Bristow⁶ for titanium indiffused waveguides with different thicknesses of the buffer layer. Problems due to both the adhesion of the SiO₂ to the LiNbO₃ and reduction of oxygen from the SiO₂ during evaporation led to several methods of deposition of the SiO₂ being tried. The final method used for the fabrication steps of the buffer layer and lower electrodes is shown schematically in Fig 3.6.

Initially attempts were made using thermal evaporation from a standard evaporator with a six inch diffusion pump and a resistive heat source. Due to the considerable outgassing of oxygen from the SiO₂ source during evaporation, the deposited buffer layer was oxygen deficient, resulting in SiO_x where $1 < x < 2$. Although no refractive index or dielectric constant measurements were conducted, the dark appearance of both the SiO₂ source and the SiO_x deposited onto the LiNbO₃ substrate were indicative of oxygen deficiency. The evaporator was pumped down to a pressure of less than 4×10^{-5} Torr before starting evaporation. Due to the outgassing, the evaporator was unable to maintain a sufficient vacuum for evaporation and the pressure rose to higher than 6×10^{-5} Torr before the deposition of 40 nm of SiO₂ onto the LiNbO₃ substrate. The evaporation was therefore a slow process with the outgassing problem becoming worse after each evaporation attempt. Problems were also encountered with the resistive heat sources, which were in the form of small tantalum boats which were only just capable of melting the SiO₂ and often broke during evaporation. The 60 Amp auto transformer was not able to supply enough current for a larger boat to be used.

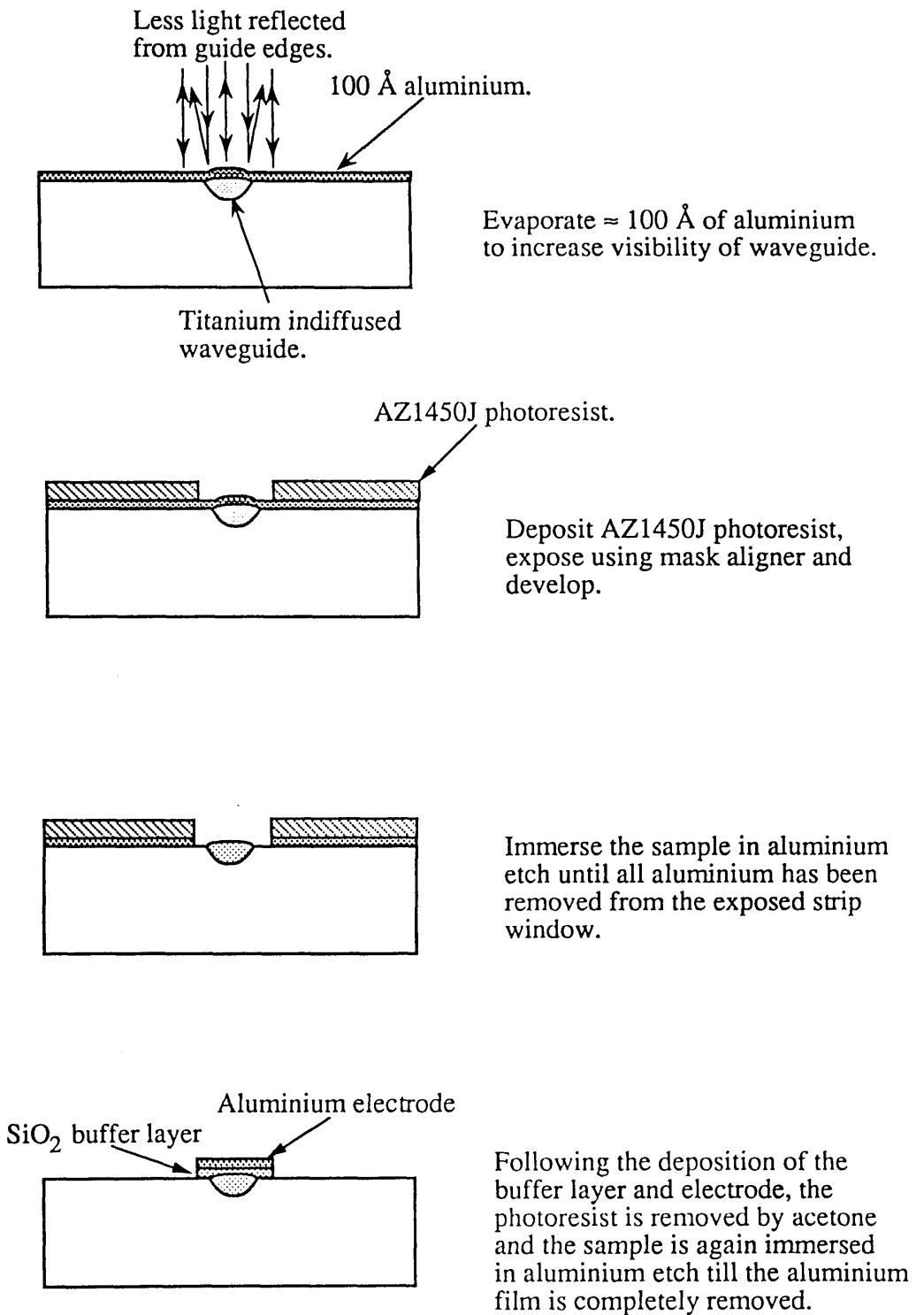
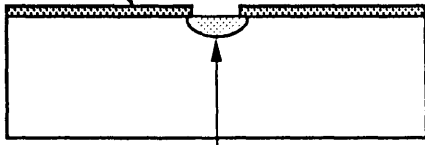


Fig. 3.6 (a). Schematic representation of the steps involved in the fabrication of the lower electrode in conjunction with titanium indiffused waveguides.

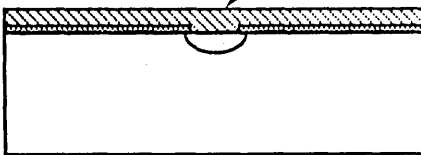
Aluminium mask left after waveguide fabrication.



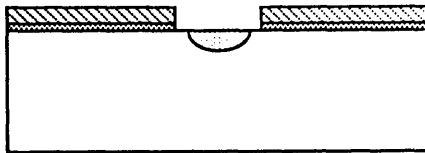
Proton exchanged waveguide.

Following waveguide fabrication the sample is thoroughly cleaned to remove grease and dirt.

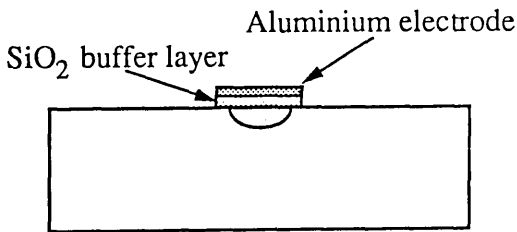
AZ1450J photoresist.



Sample is placed in aluminium etch till approximately 50 Å of aluminium remains followed by the deposition of AZ1450J photoresist.



After the photoresist has been exposed and developed, the sample is immersed again in the aluminium etch till all aluminium has been removed from the strip window.



Following the deposition of the buffer layer and electrode, the photoresist is removed by acetone and the sample is again immersed in aluminium etch till the mask is completely removed

Fig. 3.6 (b). Schematic representation of the steps involved in the fabrication of the lower electrode inconjunction with proton exchange waveguides.

Chemical Vapour Deposition (CVD) was also tried, but this prevented the use of lift-off since the high temperature that the substrate reached ($\sim 300^\circ\text{C}$) during deposition caused the destruction of the photoresist pattern. A planar buffer layer could have been deposited using CVD and strip electrodes photolithographically fabricated on top, but the use of a planar layer would have weakened the bond between the supporting substrate and the LiNbO_3 substrate. During initial attempts at fabricating the transverse modulator, planar electrodes with a planar buffer layer were used. Cracking along the SiO_2 layer was observed on all substrates and this also resulted in the LiNbO_3 substrate cracking. Alternatively a planar layer could have been deposited and etching used to form a strip buffer layer over the waveguides. It was felt that an alternative method should be found to provide an adequate buffer layer strip by lift-off, without the need for the extra stages involved in etching. Evaporation of the SiO_2 using an electron gun was also tried but, although standard practice elsewhere, due to the nature of the electron gun used it was not capable of melting the SiO_2 in a uniform manner. Before the SiO_2 was melted completely, the electron gun used would short circuit.

It was therefore decided to try and achieve a satisfactory evaporation from a resistive heat source with an improved evaporator. The evaporator used was fitted with a twelve inch diffusion pump in order to maintain a vacuum below 5×10^{-6} torr during evaporation. This enabled the required buffer layer thickness of 200 nm to be deposited in one evaporation, which partially prevented the reduction of oxygen from the deposited SiO_2 layer. A 120 Amp transformer was also fitted so that a larger tantalum boat could be used during evaporation. The larger boat was capable of evaporating at a higher temperature, which allowed a faster evaporation rate to be used. In order to reduce further the outgassing of oxygen from the SiO_2 a large (0.5 cm^3) fresh piece of SiO_2 was used for each evaporation. A maximum evaporation rate of approximately 20 nm/min was achieved. Whilst the evaporator was being pumped out an RF field was applied to the bell jar and a pressure of approximately 1×10^{-2} Torr was maintained by a supply of oxygen. The RF field ionised the oxygen to create a plasma. The plasma cleaned the surface of the LiNbO_3 substrate by ion bombardment and this improved the adhesion of the SiO_2 to the LiNbO_3 . Due to the high temperatures involved in the evaporation, the LiNbO_3 substrate was left to cool for one hour under vacuum before being removed for aluminium evaporation. Since the main criterion for the SiO_2 buffer layer was to allow a

successful fabrication procedure to be established, and the subsequent measurement of the electrooptic effect, no evaluation of the reduction in the attenuation associated with the SiO₂ buffer layer was made.

3.4 Lower electrode fabrication.

The lower electrode, which was to lie adjacent to the waveguide, presented several problems during fabrication. The location of the lower electrodes created a problem in making contact to them once the device had been fabricated. Three different methods of overcoming this problem were considered. Firstly a planar electrode deposited on the waveguide surface of the LiNbO₃ substrate was considered, with contact made via a conductive epoxy from the glass substrate, see Fig. 3.7 (a). This would have enabled contact to have been made easily to the lower electrodes from a conductive strip on the glass substrate. Secondly, the electrode could be fabricated on the glass slide with either a conductive epoxy used to drop the voltage across the substrate or a non-conductive epoxy and the voltage dropped across both the substrate and the epoxy, see Fig. 3.7 (b). Problems with the strength of the bond achieved prevented the use of conductive epoxies (see section 3.6) while the thickness of the epoxy bond layer, measured optically at approximately 1 μm, would have increased the operating voltage requirements by 10 % for a 10 μm thick substrate. Thirdly planar or strip electrodes could be fabricated on the waveguide surface of the LiNbO₃ substrate and contact made through the substrate from the top surface, see Fig. 3.7 (c). It was this third option that finally proved successful.

For planar electrodes, 25 nm of titanium was evaporated by e-beam. Titanium was used since aluminium, although more conductive, was softer and more easily removed from the LiNbO₃ surface by scratching which might have weakened the bond between the LiNbO₃ substrate and the glass substrate. Since initial attempts were mainly concerned with developing a fabrication procedure the waveguide attenuation was unimportant and, for ease of fabrication, no buffer layer was used. Before starting fabrication of the electrodes the substrates were again thoroughly cleaned using the process described in section 3.2.1. Two main problems prevented the use of planar electrodes. The conductive epoxies used to make contact from the glass substrate were not suitable due to small gas bubbles which were outgassed from the epoxy on curing. The gas bubbles created a weak spot in the bond which resulted in the LiNbO₃ substrate

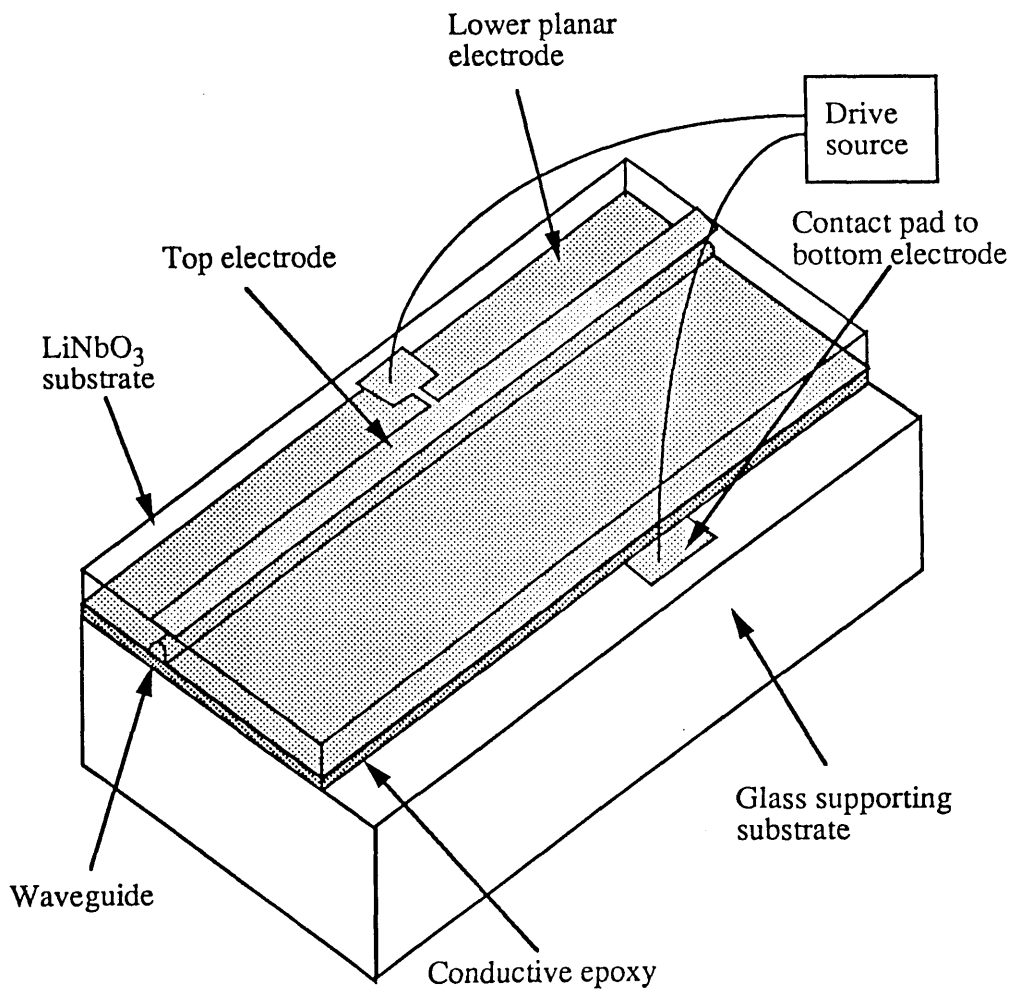


Figure 3.7 (a). Contact to the lower planar electrode via a conductive epoxy.

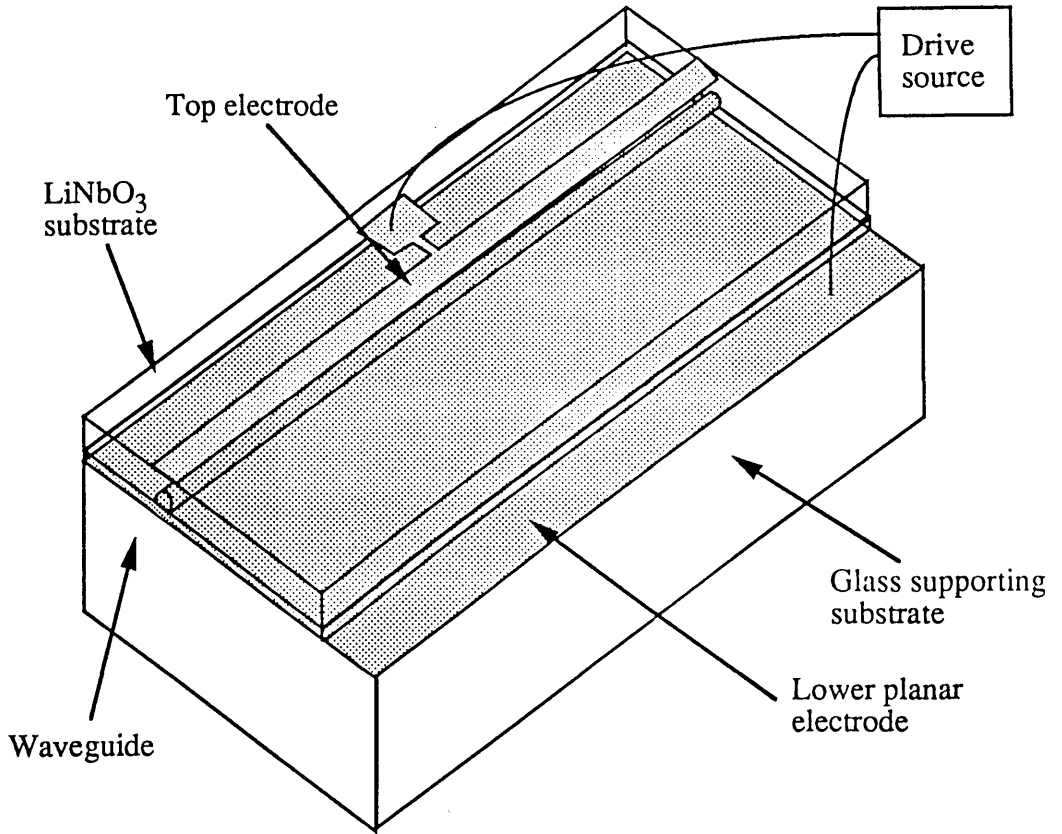


Figure 3.7 (b). Potential dropped across the substrate and bond from a planar electrode on the glass substrate.

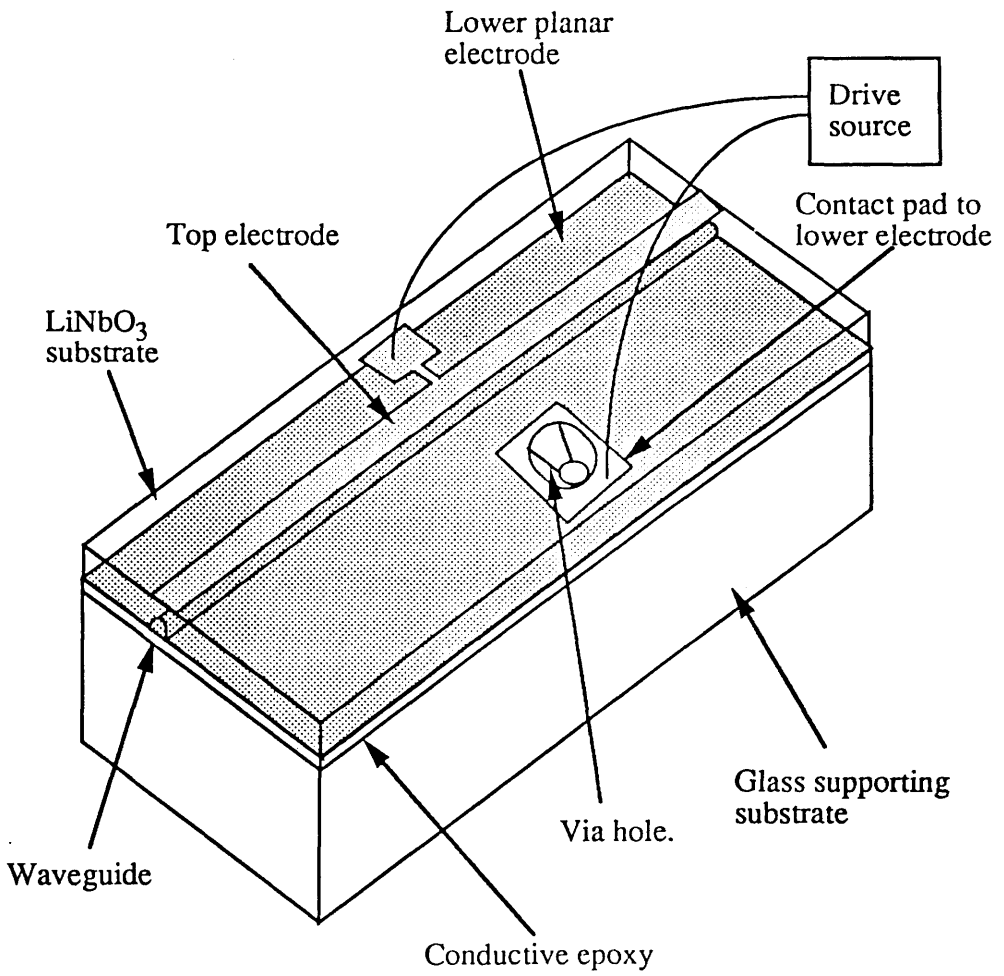


Figure 3.7 (c). Contact to the lower planar electrode from a top contact pad and a via hole etched in the substrate.

cracking during thinning. Secondly, when a planar SiO₂ buffer layer was deposited as well as the planar electrodes, cracking along the SiO₂ layer was observed and this resulted in the LiNbO₃ substrate cracking during thinning. Since the sample had to be heated during several subsequent stages when being bonded for edge-polishing or thinning, the cracking of the SiO₂ layer may have been caused by either the difference in thermal expansion of the different layers or forces exerted on the sample during the thinning.

The strip electrodes and buffer layer were patterned photolithographically from the mask shown in Fig. 3.8. AZ 1350J photoresist was used initially, before being replaced with AZ 1450J, which typically showed fewer striations after baking. This photoresist improved lift-off, especially at the edges of the substrate where the photoresist tended to be thicker.

To align the photolithographic mask with the waveguides a mask aligner was used. A small ridge was left in the LiNbO₃ during the indiffusion of the titanium waveguide which was faintly visible under the mask aligner. To increase the visibility of this ridge, 10 nm of aluminium was evaporated prior to deposition of the photoresist. Less light was reflected back up the microscope from the edges of the ridge so that a dark strip was clearly visible marking the edge of the indiffused strip, see Fig. 3.6(a). Once the centre of the waveguide was aligned with the centre of the electrode strip the photoresist was exposed and then developed. If a buffer layer was required the substrate was immersed in an aluminium etch, 16 : 1 : 3 of Phosphoric acid : Nitric acid : water. This etched a window in the aluminium, enabling the SiO₂ buffer layer to be deposited directly onto the LiNbO₃. Care was required to ensure that all the aluminium was removed from the exposed area or the SiO₂ would fail to adhere properly to the LiNbO₃ surface. Following the evaporation of the buffer layer 200 nm of aluminium, later increased to 500 nm to improve the contact from the opposite surface, was evaporated for the lower electrodes. After deposition of the electrodes the thin aluminium film was removed by wet etching in the aluminium etch, which also removed a negligible 10 nm of aluminium from the electrodes.

Proton-exchanged waveguides left no trace on the surface after the substrate had been thoroughly cleaned. The aluminium mask used to define the strip guides during proton-exchange was therefore also used to align the electrodes, see Fig. 3.6 (b). The mask, 40 nm thick, was immersed in an aluminium etch to reduce the thickness before the photoresist was deposited.

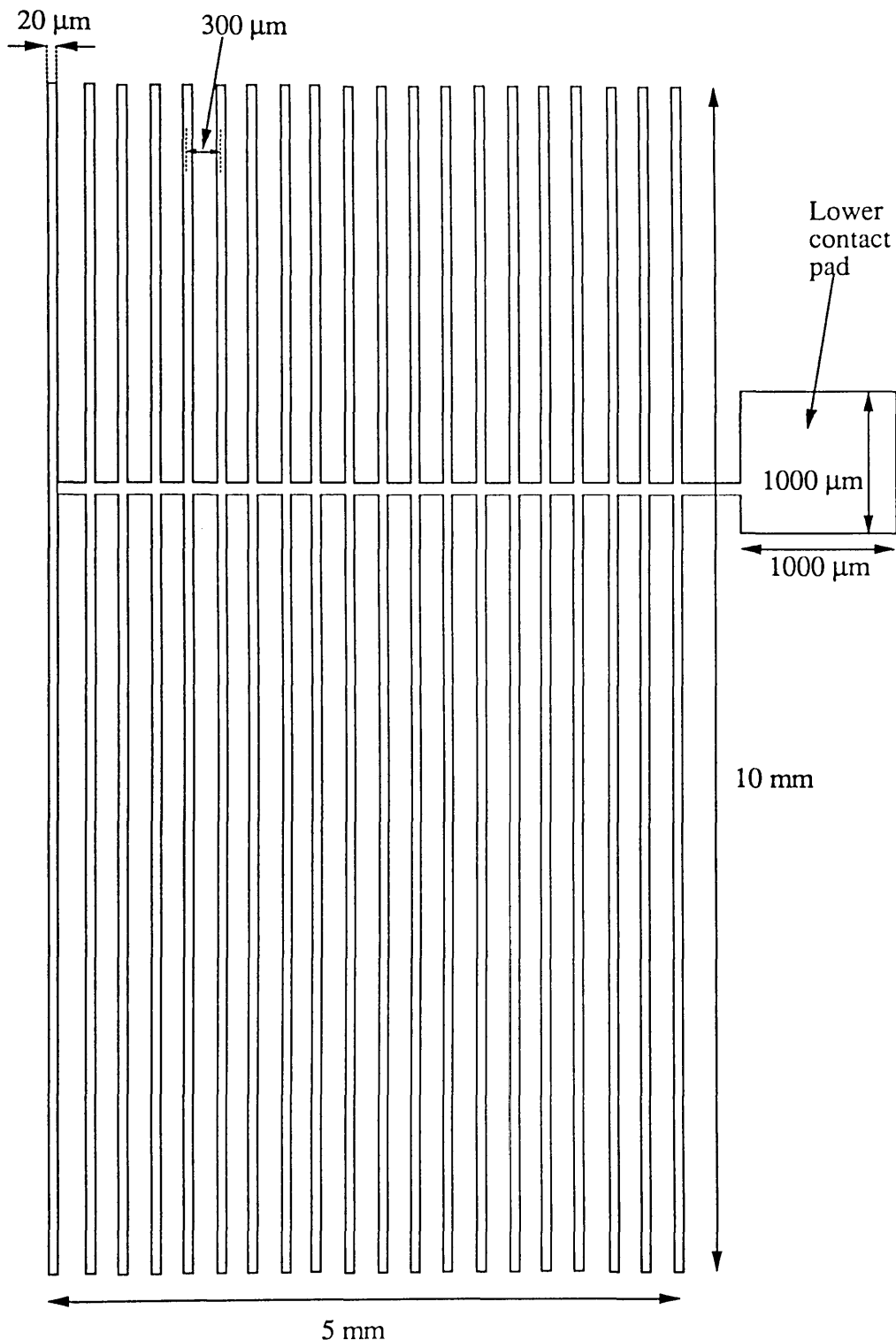


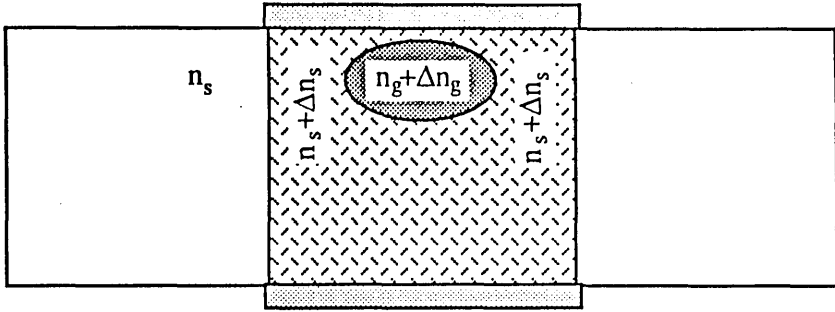
Fig. 3.8. Photolithographic mask used for lower electrodes

Large areas of the mask were resistant to the etch and showed no signs of etching after the rest of the mask was removed. This may have been caused by either heavy oxidation of the aluminium mask or the formation of an aluminium compound during the proton-exchange process. If the waveguides were annealed before the mask was etched, more of the aluminium surface appeared to be affected and the etch rate was further decreased. It has been found that, by first immersing the substrate in warm sulphuric acid for 5 minutes, the aluminium would etch at a uniform rate when immersed in the aluminium etch. The aluminium was etched until the aluminium mask was only faintly visible for alignment. After the photoresist had been exposed and developed the substrate was once again immersed in the aluminium etch to remove the aluminium from the exposed electrode strip before the deposition of the buffer layer. After both the buffer layer and the electrode had been fabricated, the LiNbO_3 substrate was once more immersed in the aluminium etch to remove the remains of the aluminium mask and this also removes a negligible amount of aluminium from the electrodes.

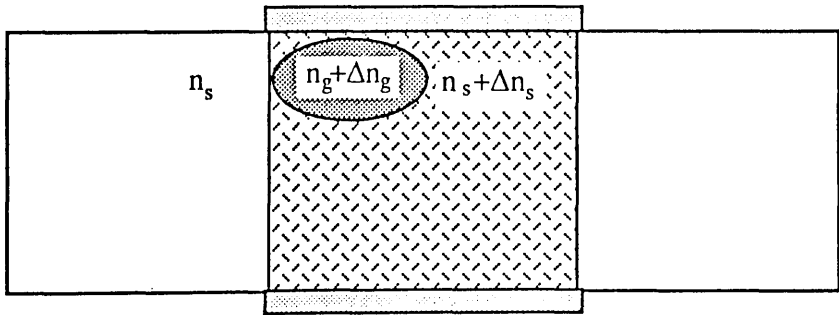
It was important to ensure that the waveguides were aligned with the centre of the electrodes. The effective index of the waveguide was dependent on the refractive index of both the waveguide and the surrounding substrate, see Fig. 3.9. If the waveguide were situated below the centre of the electrode there would be an equal change in refractive index in the waveguide and the surrounding substrate and only an electrooptical change in the effective refractive index would be present. If the waveguide were positioned nearer to one edge of the electrode there could be an unequal change in the refractive index of the waveguide and the substrate to one side of the waveguide when an electric field was applied. The new difference in the refractive index between the waveguide and the surrounding substrate would have resulted in an additional change in the effective refractive index, leading to an unwanted phase shift. In addition there would also be a shift in the position of the optical field profile which could have led to some amplitude modulation.

3.5 Supporting substrate.

In order to support the LiNbO_3 substrate whilst thinning, and during the remaining fabrication steps, it was necessary to bond the substrate to a supporting substrate. The supporting substrate was required to have a coefficient of thermal expansion close to that of LiNbO_3 and be of comparable hardness to



n_{eff} is dependent on $(n_s + \Delta n_s)$ and $(n_g + \Delta n_g)$ only.



n_{eff} is dependent on $(n_s + \Delta n_s)$, $(n_g + \Delta n_g)$ and n_s .

Fig. 3.9 Effect of off-centre alignment between the electrodes and the guide on the effective index of the guide.

LiNbO₃. Since the sample had to be heated to approximately 80 °C when it was wax-bonded for edge-polishing or thinning, a large difference in the coefficient of thermal expansion between the glass substrate and the LiNbO₃ substrate would have led to the bond between the two substrates being destroyed. If the supporting substrate were harder or softer than the LiNbO₃ substrate, the two materials would polish at different rates during edge polishing which would have resulted in the rounding of the waveguide edge. The two obvious materials for use as a supporting substrate were glass and LiNbO₃. The use of LiNbO₃ as the supporting substrate would appear to be the natural choice since there will be no difference in thermal expansion or in the polishing rate. Several samples were tried with a LiNbO₃ supporting substrate but due to their brittle nature, such substrates were prone to damage throughout the rest of the process, especially to chipping during edge-polishing.

Glass microscope slides were used for the supporting substrate in all successful devices. The supporting substrate had to be flat to ensure that the thickness of the thinned substrate, and therefore the electric field across the substrate, would be uniform. The tolerance for the thickness of the slide was set at $\pm 0.5 \mu\text{m}$ over an area of 1.5 cm^2 . The slides were not polished to the required tolerances but were selected from standard microscope slides and checked using a Linear Voltage Differential Transformer (LVDT) which had an accuracy of $0.1 \mu\text{m}$. The glass slides, supplied by Chance Propper Ltd, had a mean linear coefficient of thermal expansion which was 7.87×10^{-6} per °C, compared with 16.7×10^{-6} per °C for the LiNbO₃ substrate, and so care was still required whilst heating and cooling the substrate.

3.6 Substrate bonding.

Before commencing fabrication of the modulator the feasibility of thinning a LiNbO₃ substrate to $10 \mu\text{m}$ was demonstrated. Three LiNbO₃ substrates were bonded to a glass slide using an ultra violet curing (U.V) epoxy. This was successful for all three substrates. The problems with cracking associated with the bonding layer appeared to be introduced when either a conductive epoxy was used or additional planar layers, such as the planar buffer layer, were introduced between the glass substrate and the LiNbO₃ substrate.

The feasibility of using a conductive epoxy to enable contact to be made to the lower electrodes was studied in section 3.4. The use of both conductive

epoxies and non-conductive epoxies as a bonding agent between the LiNbO₃ and glass substrates will now be discussed. Silver epoxies were available with low resistivity ($\sim 0.3 \text{ ohm/m}^2$) and high bond strengths. Several of these epoxies were tried, with the best being A-1751 single-part silver epoxy from Johnson Matthey Chemicals Ltd. All other silver epoxies that were tried outgassed on curing, creating small air bubbles in the bond. The nature of the gas was not known but its source was likely to be from solvents in the epoxy. The gas bubbles formed may have been prevented by curing in a vacuum. Once the LiNbO₃ substrate had been thinned, cracks originated at the air bubbles due to the lack of support. Although the manufacturers claimed no outgassing with A-1751, on many occasions very small gas bubbles were observed to form during curing. The bubbles were typically only 5-10 μm wide but were still large enough to create problems and cracks on several samples were observed to originate from the bubbles. In total, only one substrate was successfully thinned using a conducting epoxy and, although badly cracked, it was still capable of guiding light.

The use of a conductive epoxy was abandoned on two accounts, firstly the difficulty in achieving a satisfactory bond capable of supporting the LiNbO₃ during thinning and secondly the eventual use of strip electrodes would require the contact to be made at a specific location as opposed to the whole face. The use of either a two part epoxy or a U.V curing epoxy eliminated outgassing since no heating was required to cure the epoxy (although some chemical heating could be present in the two part epoxies). A non-conductive epoxy also tended to provide a much thinner, smoother bond than a conductive epoxy. The silver particles present in the A-1751 had a mean size of 10 μm and maximum size of 40 μm . The bond would therefore be at least 10 μm thick, possibly much thicker, while the bond obtained from a non-conducting epoxy was less than 2 μm . Since the remaining epoxies were not conductive, contact to the bottom electrodes would have to be made by etching through the LiNbO₃ to a contact pad attached to the lower electrodes, see section 3.9.

The first non-conductive epoxy used in the fabrication of the modulator was Loctite 365 U.V epoxy, as this had already been used to demonstrate the feasibility of thinning a LiNbO₃ substrate to 10 μm . The epoxy was cured by exposure to light from a 150 watt mercury-xenon lamp with a high ultra violet spectrum for 1/2 hour. Although no outgassing occurred with this epoxy during or after curing, the bond was severely weakened when the sample was heated

during wax bonding for edge-polishing and thinning. The U.V epoxy appeared to expand much more upon heating than either the LiNbO_3 substrate or the glass substrate. This caused the U.V epoxy to break away from the LiNbO_3 substrate and the glass substrate in places; once again cracks appeared in the LiNbO_3 substrate during thinning. An alternative epoxy, Logitech 301, had a coefficient of thermal expansion close to that of glass and similar refractive index and had already been used by Logitech for the thinning of geological rock samples. Logitech 301 was a two part epoxy which cured in 24 hours at room temperature. A perfect bond was obtained with this epoxy and, providing care was taken that the temperature when heating the sample did not exceed 90°C , the bond was maintained throughout the whole process.

As well as the supporting substrate being required to be of uniform thickness, the bond between the LiNbO_3 device substrate and the supporting glass substrate must also be of uniform thickness. Any variation in the thickness of the bond would, assuming the thickness of the glass substrate to be uniform, be transferred to the thickness of the thinned LiNbO_3 substrate. For example if the bond were $1\ \mu\text{m}$ thinner at one end than the other, the LiNbO_3 substrate would have been $1\ \mu\text{m}$ thicker at that end. The effect of an uneven bond on the final substrate thickness is shown in Fig. 3.10(a). The thickness of the bond was checked by measuring the substrate thickness in the middle and at the four corners, both before and after bonding, using a Linear Voltage Differential Transformer (LVDT). A bonding jig, shown in Fig. 3.10(b), was used to improve the uniformity of the bond. A PTFE block, centred over the LiNbO_3 substrate, pivoted about the end of a spring loaded pin providing an even force over the surface of the substrate. The jig tended to exert too much force on the LiNbO_3 substrate, occasionally causing it to bevel and in general proved to be more bother than it was worth.

3.7 Edge polishing.

In order to allow efficient launching of light into a stripe waveguide by either endfire coupling with microscope objectives or butt jointing of fibres, the edge of the LiNbO_3 substrate was cut perpendicular to the waveguide axis before it was polished to remove chips, scratches and roll-off at the edges.

When the substrate had been thinned to less than $50\ \mu\text{m}$, the edges of the substrate were liable to chipping and scratching from the abrasive. It was

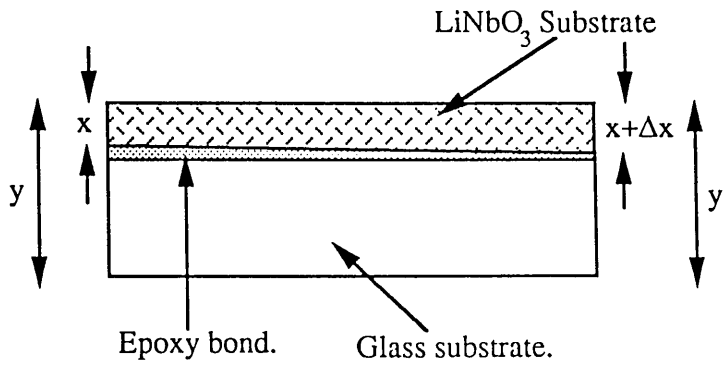


Fig. 3.10 (a). The effect of an uneven bond on the thickness of the lithium niobate substrate after thinning.

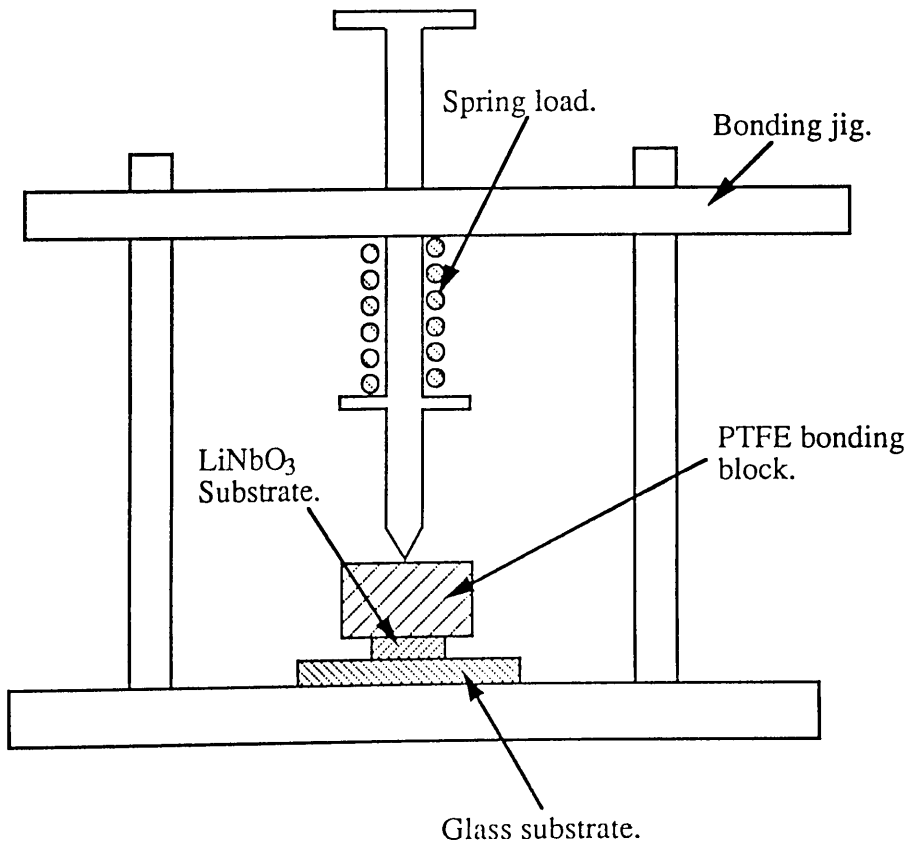


Fig. 3.10 (b). Bonding jig used to ensure a parallel bond between the lithium niobate substrate and the glass substrate.

therefore necessary either to polish the edges after the substrate had been thinned or to polish the edges before thinning and protect them from chipping or scratching during the thinning process. Attempts at edge-polishing three substrates which had previously been thinned to 10 μm were unsuccessful. In an attempt to prevent the edges of the thinned LiNbO_3 substrate from chipping, the surface of the substrate was bonded hard against a quartz block but the stress involved in the edge-polishing caused all the thinned substrates to break, with severe cracking across the entire surface mainly originating at the edges. To protect the edge during the thinning process either quartz or LiNbO_3 blocks could have been mounted around the samples or shellac or quartz wax could have been melted round the edges of the sample. The wax or shellac was chosen since it was simpler and loose chips from the protective blocks could have deeply scored the surface of the LiNbO_3 substrate. The quartz wax was found to work better than the shellac since its more viscous nature allowed it to adhere better to the edges of the substrate. The quartz wax appeared to polish at a similar rate to the LiNbO_3 substrate and also polished smoother than the shellac which tended to chip leaving parts of the edge unprotected.

Conventionally edge polishing has been a slow process, with the method used at Glasgow University and alternative methods reported elsewhere⁷ taking several hours to polish one edge. Furch⁸ reported a novel edge-polishing technique taking only 20 minutes. The technique involved the endface of the substrate being cut by a wire saw prior to it being polished using two different abrasives and two polishing compounds. Between each step the jig and the sample had to be cleaned ultrasonically to ensure that there was no contamination of the next stage from the larger particle sizes of the previous polishing compound. With such a polishing technique, unless there is a different polishing machine for each individual stage, the machine used must be cleaned between stages. This considerably increases the time required for the process and makes it labour intensive. A new process was therefore developed which, although slightly longer, only required one abrasive and one polishing fluid, making the process less labour and machine intensive.

The substrate, once bonded to the supporting glass substrate, was cut to a size of approximately 8 x 8 mm^2 using a circular saw with a diamond impregnated disc. This ensured that the waveguides were exposed at opposite ends of the LiNbO_3 substrate. The reduction in the size of the LiNbO_3 substrate also decreased the risk of the sample being damaged during the thinning process.

The dimensions of the electrode pattern prevented any further reduction in the size of the substrate. Although the disc saw tended to create small chips at the edges of the LiNbO₃ substrate, it was much quicker than a wire saw and the chips were quickly removed during the initial stages of edge-polishing. The sample was then mounted, using shellac, onto a quartz block to protect the edges from chipping, see Fig. 3.11(a). For the edge-polishing of standard LiNbO₃ substrates it is necessary to ensure that the bond between the waveguide surface of the LiNbO₃ substrate and the supporting block is less than 2-3 μm thick. Rounding of the substrate edges has been observed⁸ for bonding layers between the LiNbO₃ substrate and the quartz block thicker than 3 μm. An alternative method of mounting the sample is to clamp it mechanically to a second block of LiNbO₃ which completely eliminates the gap at the edge of the substrate. For the edge-polishing of the transverse modulator the waveguide surface was already bonded onto the glass supporting substrate and so no special methods were required for mounting the sample. If there were any visible chips in the edges parallel to the waveguides these had to be removed by polishing as they would have created stress points once the substrate was thinned.

Dental wax was used to mount the quartz block into a “polishing pot”, an aluminium pot designed to hold the quartz block and screw onto the sample plate of a Logitech polishing jig, see Fig. 3.11(b). The loading on the sample could be adjusted from 0 to 1.5 Kg, and for the edge polishing a maximum loading of approximately 1 Kg was used. The polishing jig consisted of a conditioning ring attached by three legs to the body of the jig. A spring loaded piston ran through the center of the body, with the sample plate at the bottom of the piston. The loading on the sample was adjusted by varying the amount of loading supported by the spring.

Once the sample had been mounted it was lapped on a cast iron plate, using 3 μm alumina in suspension as the abrasive, for approximately 15 minutes to remove any chipping or deep scratches. To reduce the surface roughness of approximately ± 0.3 μm left by the 3 μm alumina on the cast iron plate, the sample was then lapped using 3 μm alumina oxide on a brass plate, for approximately 15 minutes. Since the brass was softer than the cast iron this leaves a smoother finish to the edge without the need to reduce the size of the abrasive particles. Initially the edge was lapped using 9 μm alumina as the abrasive on the cast iron plate, followed by 3 μm alumina on the brass plate: this required the jig and the sample to be cleaned thoroughly before proceeding to the

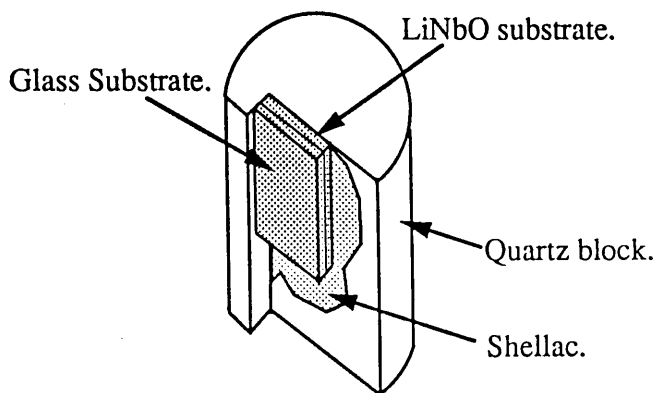


Fig. 3.11 (a). Substrate mounted onto a quartz block to prevent chipping during edge polishing.

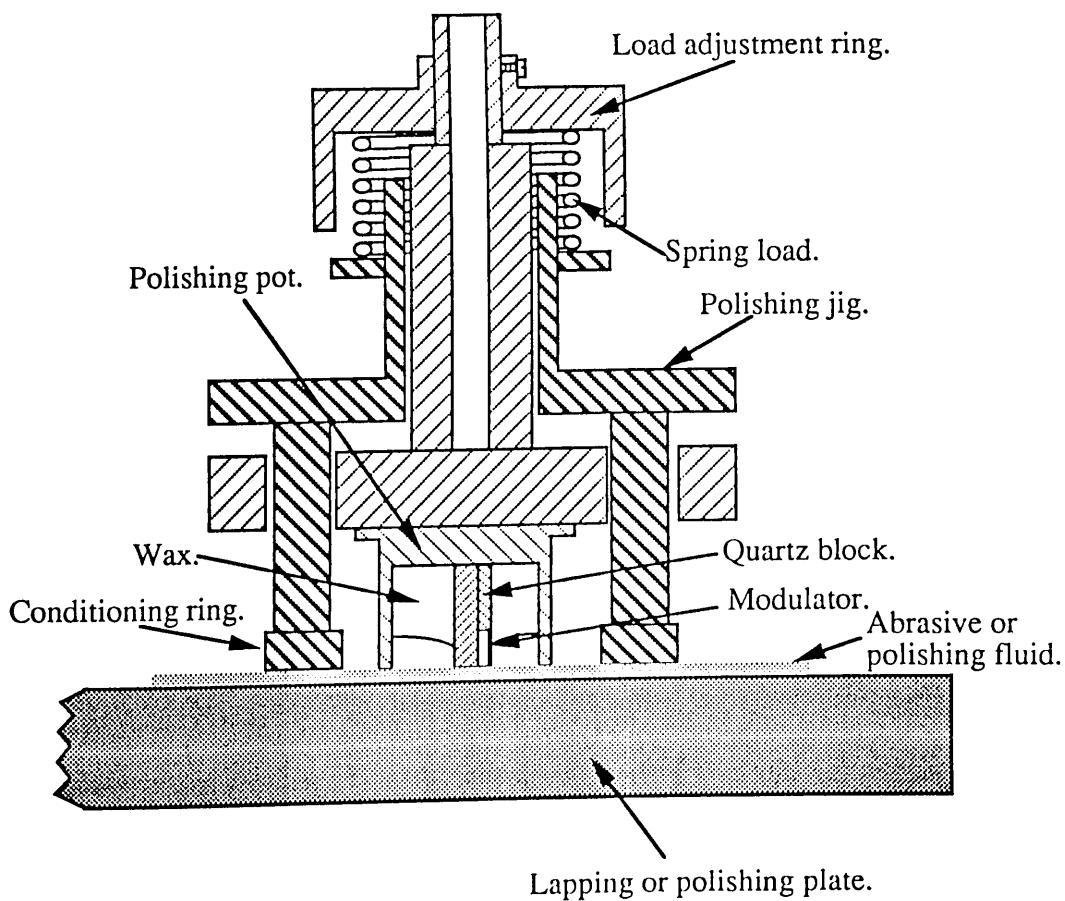


Fig. 3.11 (b). Polishing jig adapted for edge polishing.

smaller abrasive. Only a small difference was observed between the lapping rates of the 3 and 9 μm alumina on the cast iron plate and therefore the 3 μm alumina was used throughout the lapping process. The edge was polished on an expanded polyurethane plate using Syton, a suspension of particles of silicon dioxide smaller than 0.1 μm , supplied by Union Carbide. The jig and polishing machine had to be cleaned thoroughly before polishing since any contamination from the alumina abrasive is likely to scratch the edge during polishing. The edge was polished till no chips or scratches were observable at a magnification of 1000, this usually took 15 minutes of polishing. After the edge polishing the sample was removed from the “polishing pot” and thoroughly cleaned in acetone to remove any shellac.

3.8 Thinning.

The basic method of thinning the transverse modulator was developed from the technique used by Logitech Ltd for the polishing of thin geological rock samples. This technique involves two main stages: firstly the sample is lapped down using an abrasive fluid containing particles ranging from 3 to 25 μm , usually a solution containing alumina or a diamond paste, on a lapping plate. The lapping plate used depends on the hardness of the material being thinned and may be made from cast iron, solder, tin, brass or lead. Depending on the surface finish required, the sample may then be polished using a solution containing very fine particles, <0.1 μm , on a soft polishing plate.

The sample was held by a Logitech PP5 polishing jig, shown in Fig. 3.12, during thinning. The PP5 jig normally uses a vacuum chuck to hold the samples in place during polishing but the small size of the samples prevented a good enough bond being achieved with the vacuum to withstand the force of the polishing action. The vacuum chuck is used on the jig since it allows the sample to be removed easily for inspection. The sample was therefore bonded to a glass plate which in turn was attached to the jig by the vacuum chuck. The glass plate was slowly heated to approximately 90 °C on a hot plate and quartz wax spread thinly onto the centre of the glass plate. The sample was also heated slowly to 90 °C to prevent thermal shock, before being bonded by the quartz wax to the plate with the glass supporting substrate face down. It was important that the temperature was kept as low as possible to avoid excessive thermal expansion of the individual layers in the bond. A large difference in the expansion of two adjacent layers would have led to them splitting and destroying the bond.

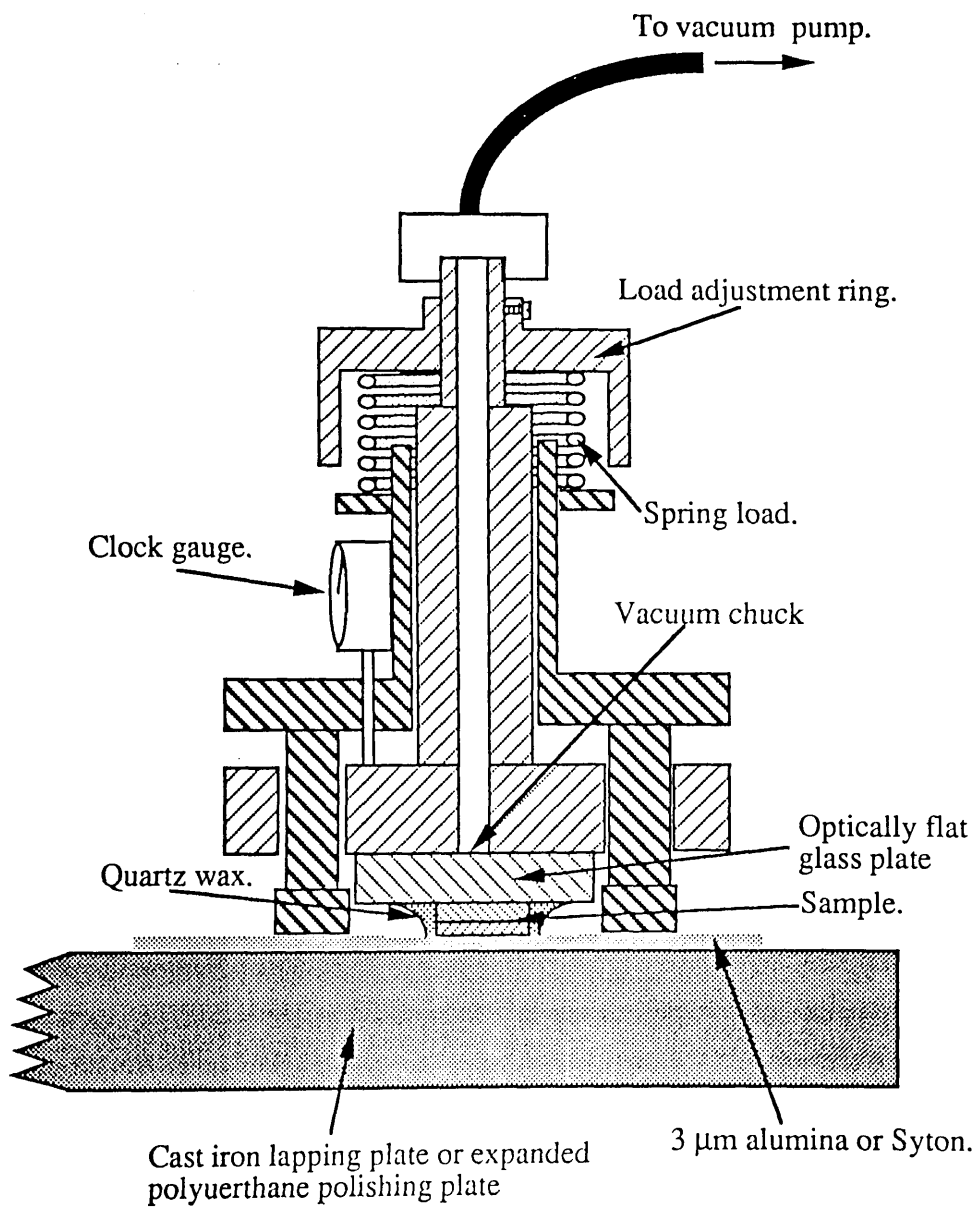


Fig. 3.12 Lapping jig used to thin and polish the sample to less than 20 μm .

The thickness of the wax bond between the sample and the plate had to be uniform to ensure that the thickness of the LiNbO₃ substrate after thinning was uniform. The height of the LiNbO₃ substrate above the glass plate was measured in the centre and at the corners of the substrate to check the uniformity of the thickness of the bond and was used as the starting thickness for thinning. The thicknesses of the LiNbO₃ substrate and the glass supporting substrate were measured both before and after they were bonded to each other. The initial thickness of the LiNbO₃ was used to calculate the amount of LiNbO₃ that had to be removed from the starting thickness measured on the glass plate. The thickness during thinning was continuously monitored using a clock gauge attached to the polishing jig and periodically checked against the thickness measured using the LVDT.

Once a satisfactory bond had been achieved between the sample and the plate, quartz wax was melted around the sample until all the edges were completely covered. As well as protecting the edge-polished faces of the LiNbO₃ substrate, the quartz wax prevented the other edges from chipping. Any chips on the thinned LiNbO₃ substrate provided a stress point from which cracks would spread across the substrate.

Before the sample was attached, the vacuum chuck was lapped until a thin layer had been removed from its surface. This ensured that both the vacuum chuck holding the sample and the conditioning ring were parallel. The substrate was thinned or lapped on a cast iron plate with a rotational speed of 50 rpm using 3 µm alumina in suspension for the abrasive fluid. The jig was set at a loading of approximately 0.75 Kg and reduced to approximately 0.5 Kg once the substrate had been thinned to 200 µm. The cast iron plate was radially grooved to allow the alumina into the centre of the conditioning ring. A lapping rate of 20 µm per min was obtained, allowing the substrate to be thinned in less than one hour. The lapping rate was controlled by adjusting either the loading on the sample or the rotational speed of the lapping plate. If the lapping rate were increased too much, the substrate became liable to chipping and cracking due to the additional stress created by the increased speed of the lapping plate or loading on the sample.

Although the average roughness of the LiNbO₃ substrate face was measured with a Talystep at ± 0.3 µm, surface damage, created by the lapping

action, to a depth of 4 to 6 μm was estimated by G. Graham at Logitech Ltd. This damage was attributed to the loading effect on the sample, along with a tendency for the abrasive particles to ride over each other, causing scratching to a depth greater than the particle size of the abrasive. This damage prevented the LiNbO_3 substrate from being lapped to less than 6 μm from the final desired thickness. By reducing the loading on the plate as the sample approached the target thickness, the depth of the surface damage could be minimised. Initially samples were lapped down to 30 μm before being polished down to the target thickness, but this was very slow, since little more than 4 μm per hour was removed by the polishing action. The polishing also tended to crack the majority of the samples due to stress associated with the polishing action. Once again the stress could be reduced by decreasing the loading on the sample, but the hardness of LiNbO_3 prevented the loading from being reduced to a level where the risk of damage was minimised whilst maintaining a noticeable polishing rate.

After lapping, the jig and polishing machine had to be thoroughly cleaned to remove any abrasive and prevent contamination of the polishing fluid. It was in fact desirable to have at least a low-grade clean room facility and separate jigs and polishing machines for lapping and polishing. Any scratching from contaminants during polishing could have doubled the time required to polish to a given finish and increased the chances of damage due to stress. Although these extra precautions against contamination were not actually available, by taking care to ensure that the equipment was thoroughly cleaned, very few samples were damaged through contamination.

Once the substrate has been thinned it was polished using syton on an expanded polyurethane plate. The rotational speed of the polyurethane plate was 50 rpm and a jig loading of approximately 0.5 Kg was used throughout the polishing. The substrate was polished until the surface roughness left by lapping, approximately 4 μm , had been removed. This process took approximately one hour. It was desirable to keep the polishing time to a minimum since the majority of the samples which were broken during fabrication were broken at the polishing stage. This was because of the high stress on the LiNbO_3 substrate caused by the polishing action. The longer the polishing took, the greater was the risk of the substrate cracking. In an attempt to reduce the stress on the LiNbO_3 substrate the polyurethane plate was replaced by a polytron plate, but no improvement was observed.

In order to achieve thinner substrates than it has been possible to achieve so far, i.e. 15 μm , a method of reducing the stress involved in the polishing action is required. Several modulators were successfully fabricated without the upper face being polished but the surface roughness left by the lapping action, $\pm 0.3 \mu\text{m}$, resulted in the electrode gap varying by 3% for a 20 μm thick substrate and increased the probability of breaks occurring in the top electrodes.

3.9 Contact to the lower electrodes.

Once the substrate has been thinned and polished, the lower electrodes are sealed between the LiNbO_3 substrate and the supporting glass substrate with no point of contact exposed. It was therefore necessary to develop a method by which contact from the modulating drive source could be made to the lower electrodes.

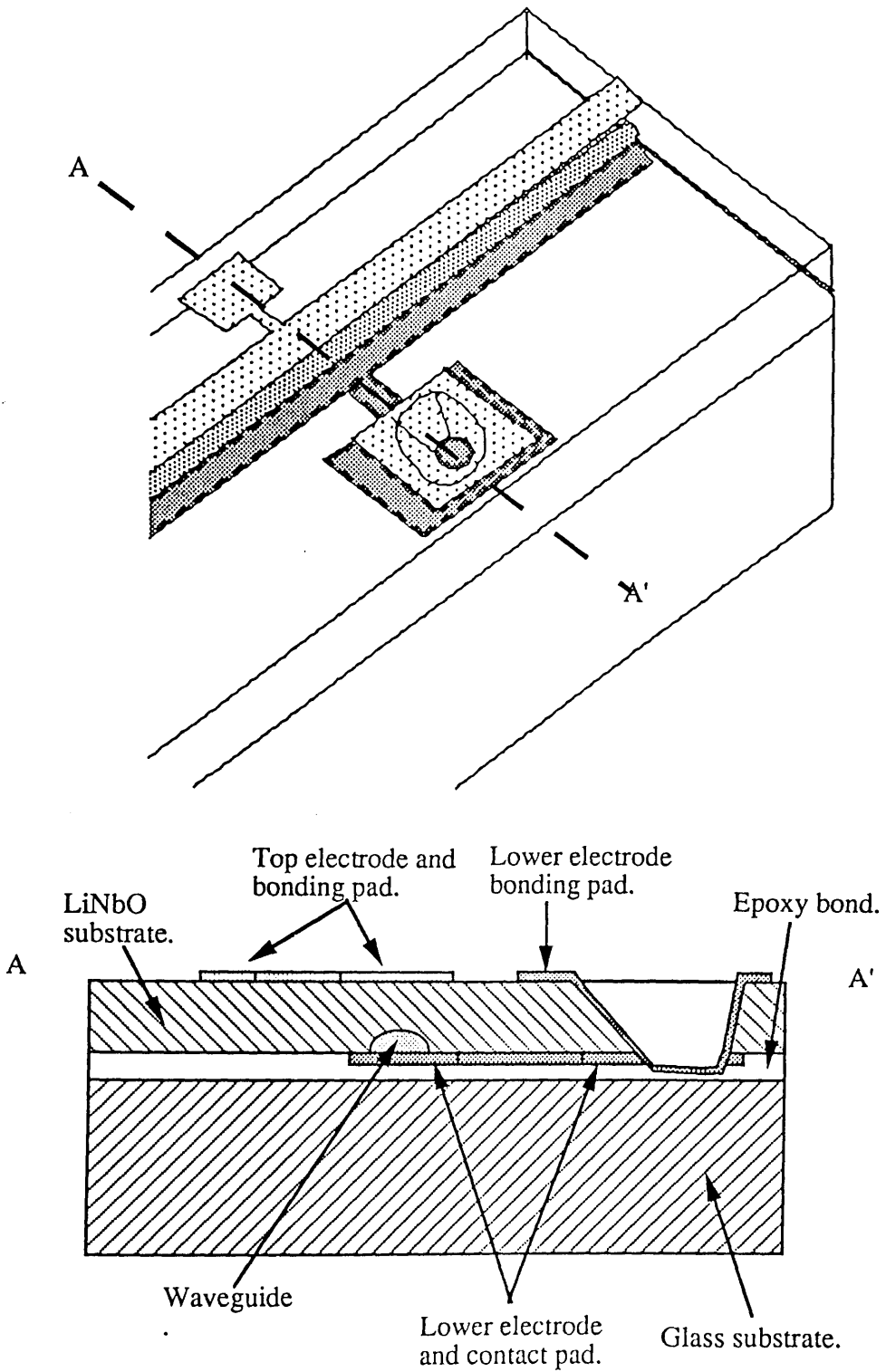
Some of the methods that were tried for achieving contact to the lower electrodes have already been discussed in section 3.4. The first used a conductive epoxy to bond the electrode face of the LiNbO_3 substrate to a large titanium bonding pad on the glass supporting substrate, see Fig. 3.7(a). This would have allowed contact to be made to the lower electrode via a wire bonded to the glass supporting substrate. This method was abandoned since the outgassing of the epoxy upon curing, reported in section 3.6, prevented the substrate from being thinned successfully. A second problem would have occurred, had it been possible to thin the substrate, since the use of a planar conductive epoxy would have prevented the use of strip electrodes on the lower face of the LiNbO_3 substrate. Several attempts were made using a non-conductive epoxy, i.e U.V. epoxy, to bond the LiNbO_3 substrate to the supporting substrate with a small area bonded using a conductive epoxy. This would have allowed strip electrodes to be used but didn't prevent the outgassing from the conductive epoxy causing the sample to crack.

If it was not going to be possible to make contact via the bond between the supporting substrate and the LiNbO_3 substrate, contact would have to be made through either the glass supporting substrate or the LiNbO_3 substrate. The thickness of the glass substrate would have made it hard to expose a contact pad on the lower face of the LiNbO_3 substrate through the glass substrate. The possibility of etching a hole through the thinned LiNbO_3 substrate, exposing a contact pad on the lower face, seemed to be the most promising method since it

would not interfere with the thinning process and would enable strip electrodes to be fabricated. The etched hole had to expose a contact pad attached to the electrodes on the lower face of the LiNbO_3 substrate and allow contact to be made to it from the top surface. The hole may be referred to as a via hole, as is standard in the integrated circuit industry. The via hole walls must be coated with a metal film to make contact to the lower electrodes. The most common method of etching LiNbO_3 is by the use of Reactive Ion Etching, RIE, but this is a slow process with typical etch rates in the order of 0.01-0.05 $\mu\text{m}/\text{min}$. RIE also tends to create very vertical walls which would be hard to coat with aluminium. By using an abrasive etcher a selected area of the LiNbO_3 substrate could be etched rapidly.

A large square contact pad, having dimensions of 1000 $\mu\text{m} \times 1000 \mu\text{m}$, was incorporated into the photolithographic mask for the bottom electrodes and the aluminium thickness for the electrodes was increased to 500 nm. After the substrate had been thinned to the desired substrate thickness, the LiNbO_3 substrate above the contact pad was removed using a Pennwatt 6500 air-abrasive etcher. A hole was etched at an acute angle to the LiNbO_3 surface until half the area of the aluminium contact pad had been removed. The air-abrasive etcher used 3 μm alumina as the abrasive powder, fed under pressure to a hand held nozzle with a diameter of 0.46 mm. Although a copper mask was initially used to confine the area of etching to that above the contact pad, the nozzle was found to give enough control to confine the etching without the use of a mask. If the nozzle were held at an acute enough angle (approximately 20° to the LiNbO_3 surface) and the aluminium contact pad were thick enough (approximately 500 nm) then the hole etched through the contact pad would expose a strip of aluminium approximately 2-4 μm wide, see Fig. 3.13. If the LiNbO_3 substrate had been etched smoothly, the aluminium strip would have been less than 2 μm wide for the given etch angle and aluminium thickness, but slight chipping of the LiNbO_3 substrate at the aluminium edge increased the width.

A second pad, having dimensions of 1500 $\mu\text{m} \times 1500 \mu\text{m}$, was incorporated into the photolithographic mask for the top electrodes, see Fig. 3.14, in such a position so that etched hole would be lined with aluminium during the fabrication of the top electrodes. This second pad formed the bonding pad for the lower electrodes and made contact to the exposed aluminium strip. For protection of the operator large thick rubber gloves were required to be worn during etching, making it hard to handle the relatively small sample. The



Profile through A-A'

Fig. 3.13. Contact to the lower electrodes by means of a via hole.

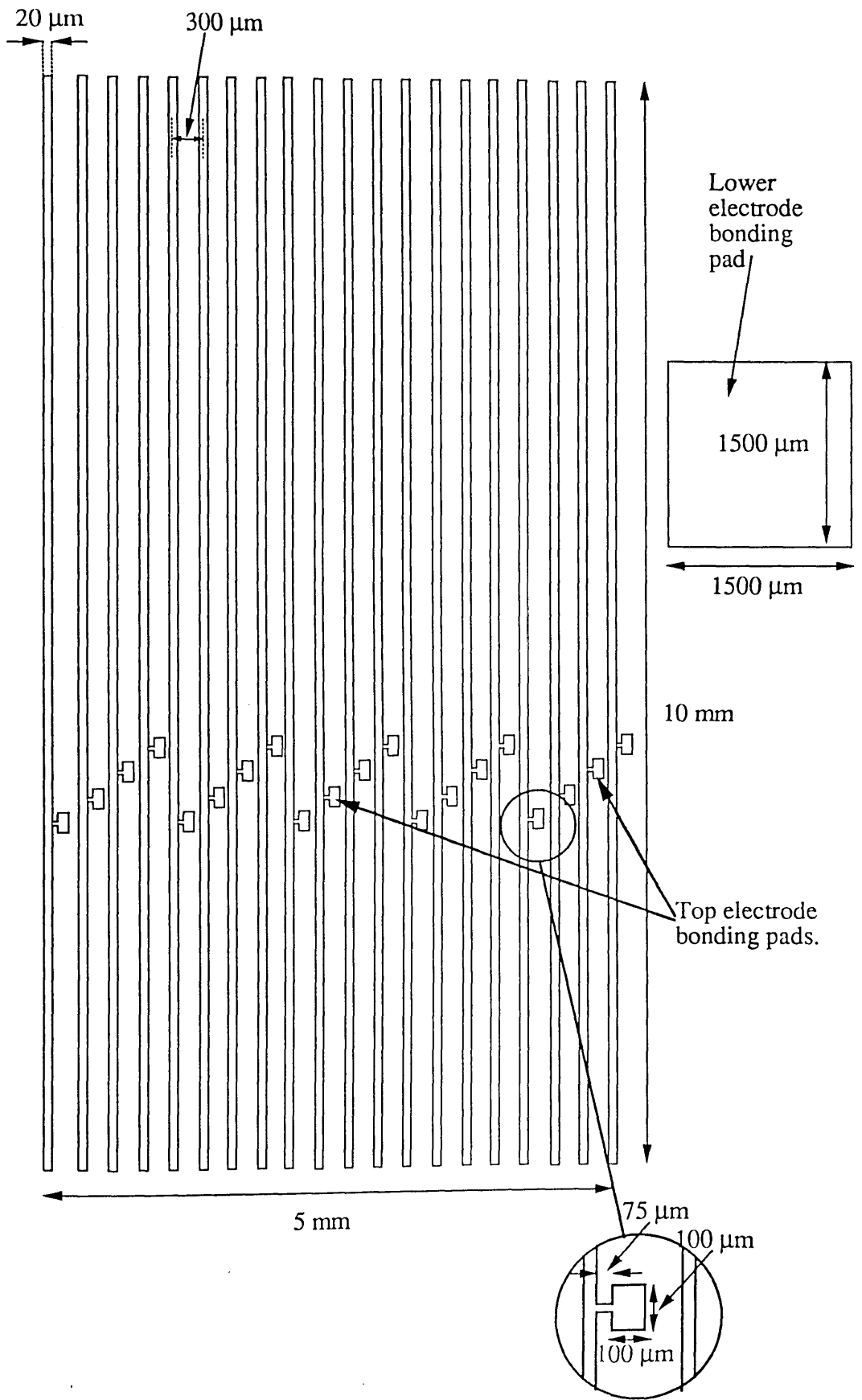


Fig. 3.14. Photolithographic mask used for top electrodes

substrate was therefore etched before it was removed from the thick glass plate used to hold the sample during thinning, making it easier to handle and improving control over the etching angle. This method gave a success rate greater than 90%.

3.10 Top electrode.

The top electrode was fabricated using the same photolithographic technique as described in chapter 3.4 and the photolithographic mask shown in Fig. 3.14. The large pad unattached to the electrodes is the bonding pad for the bottom electrodes as discussed in the previous section. The top electrodes had individual bonding pads which allowed the modulators to be tested separately. No buffer layer was required prior to the electrodes since the electrodes did not lie adjacent to the waveguide but were separated by the thickness of the substrate. Due to the fragility of the sample after thinning, cleaning to the standard required for successful photolithography was a major problem. The use of an ultrasonic bath, a standard procedure before photolithography, was observed to cause severe cracking of the substrate. The sample was therefore cleaned using the same sequence of solvents as before, trichloroethylene, ethanol, methanol and RO water, in a beaker heated to 50 °C on a hot plate. The sample was left in each solvent for 10 minutes to remove any wax, grease or dirt. The use of a hot plate instead of an ultrasonic bath was not as thorough and decreased the chances of successful photolithography.

The mask aligner was used to align the photolithographic mask with the bottom electrodes and contact pad. After exposure and development the sample was loaded into a thermal evaporator for the deposition of 200 nm of aluminium. Following lift-off of the bottom electrode, the fabrication of the transverse electrooptic modulator was complete and the device was ready for mounting for electrooptic measurements.

3.11 Device mounting.

For ease of measurement of the electrooptic coefficients the modulator should be mounted to allow easy bonding to the electrodes, efficient coupling of light from the end-fire rig, simple selection of the required bonded electrodes and positional stability during measurements. A printed circuit board was designed which allowed seven individual modulators on the one substrate to be bonded at

the same time, see Fig. 3.15. The printed circuit board was connected to a junction box, allowing the easy selection and connection of individual modulators to the modulating source.

At first a Hughes HPB-360 pulsed thermal compression bonder was used to bond 50 μm diameter gold wire from the circuit board onto the bonding pad. This bonder exerted too great a pressure on the substrate during the bonding operation and resulted in a hole being punched through the bonding pad. The thermal bonder was replaced by a Kulicke and Soffa 4123 ultrasonic bonder which exerted less pressure on the substrate during bonding. After general teething problems had been solved, good bonds were achieved, providing that there was good adhesion between the aluminium and the LiNbO_3 substrate.

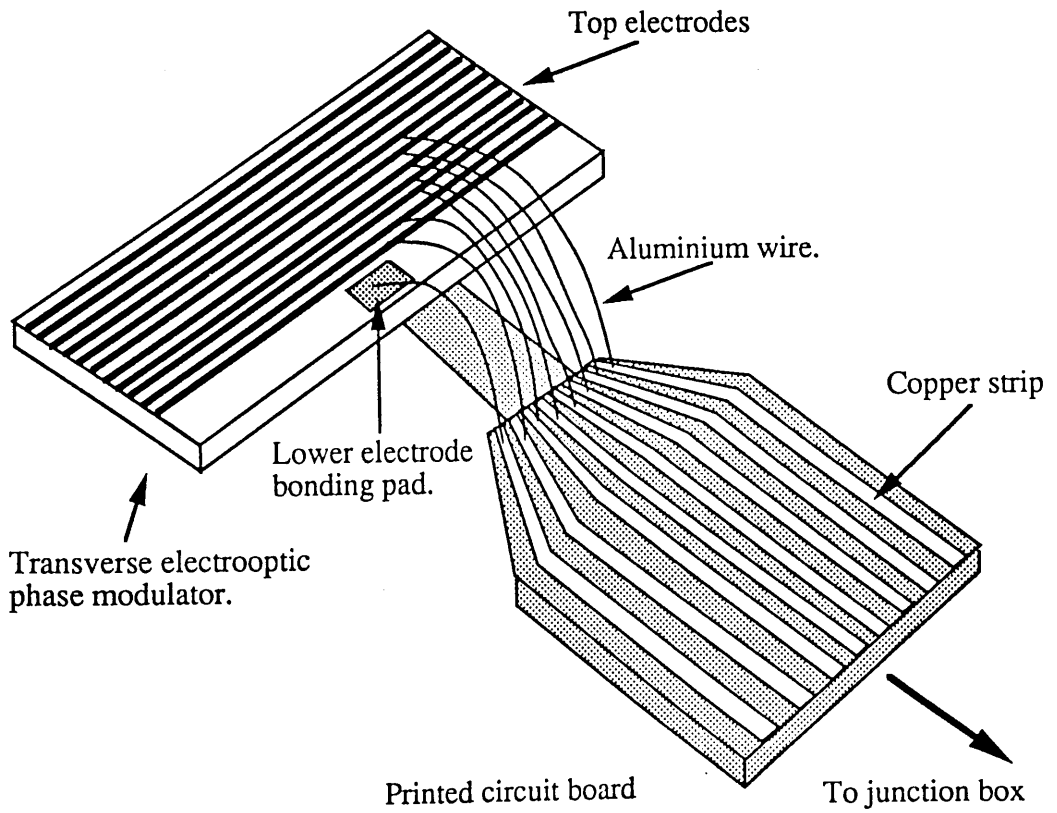


Fig. 3.15. Device mounting for optical testing.

References.

1. Nutt A. C. G., Bristow J. P. G., McDonach A and Layborn P. J. R. "Fibre-to-waveguide coupling using ion-milled groves in lthium niobate at 1.3- μm wavelength." *Opt. Lett.* **9**. Oct. 1984. pp 463-465.
2. Vu T. Q., Norris J. A. and Tsai C. S. "Formation of negative-index-change waveguide lenses in LiNbO_3 by using ion milling." *Opt. Lett.* **13**. Dec. 1988. pp 1141-1143.
3. Kaminow I. P., Ramaswamy V., Schnidt R. V. and Turner E. H. "Lithium niobate ridge waveguide modulator ", *Appl. Phys. Lett.* **24**. June 1974. pp 622-624.
4. Ashby C. I. H. and Brannon P. J. "Laser-driven chemical reaction for etching LiNbO_3 ." *Appl. Phys. Lett.* **49**. Aug. 1986. pp 475-477.
5. Loni A., De La Rue R. M. and Winfield J. M. "Very low loss proton-exchange waveguides with a substantially restored electrooptic effect." Paper MD-3, Topical meeting on Integrated and Guided wave optics, March 28-30, New Mexico, 1988, Opt. Soc. America (Washington).
6. Bristow J. P. G. "Integrated optical components for optical fibre sensors.." PhD. Thesis. Glasgow University. 1985. pp 98.
7. Stulz L. W. "Titanium in-diffused LiNbO_3 optical waveguide fabrication." *Appl. Opts.* **18**. June 1979. pp 2041-2044.
8. Furch B., Bratengeyer E. and Rauch H. "Fast high quality edge polishing of LiNbO_3 ." *J. Opt. Comm.* **4**. 1983. pp 47-50.

Chapter 4.

Theoretical modelling of the transverse electrooptic modulator.

4.1 Comparison of transmission line properties.

Since co-planar strip electrodes and slotlines, see Fig. 4.1, are not only the standard design for electrooptic modulators but are also widely used in electronic devices, there is a wide range of literature available on the theoretical properties of such electrode designs. There is not such a great use of transverse electrodes or non-coplanar microstrip lines, see Fig. 4.2, in electrooptic modulators on a dielectric substrate and so the properties are not so well documented. The following chapters will examine the main properties of both coplanar and non-coplanar designs with only a brief description of the methods used to derive the equations for each.

From the equations which will be presented, the wave impedance and the capacitance of the modulator can be determined and hence the bandwidth and the drive voltage per unit bandwidth or the figure of merit. Although the figure of merit is widely quoted as the measure of efficiency for the modulator, the value quoted is sometimes the voltage required per unit bandwidth and sometimes the power required per unit bandwidth and care must be taken when comparing figures. Since the impedance of the modulator is defined by the modulating source impedance, the voltage per unit bandwidth will be different for the same modulator with a different drive source. By quoting the figure of merit as the power required per unit bandwidth, the voltage per unit bandwidth can be easily calculated for any source impedance.

4.1.1 Transmission line properties of transverse electrodes.

The most widely used solution for the transmission line properties of parallel flat strips face-to-face was presented by Wheeler¹ in 1964. The method involved the use of a conformal transformation for the solution of the wave impedance, from which the capacitance and inductance may be found, for a transmission line in a uniform medium. The method was later extended by the introduction of an effective filling fraction for the solution of strips separated by a dielectric material surrounded by free space². A description of the conformal transformation and the derivation of the resulting equations is presented in

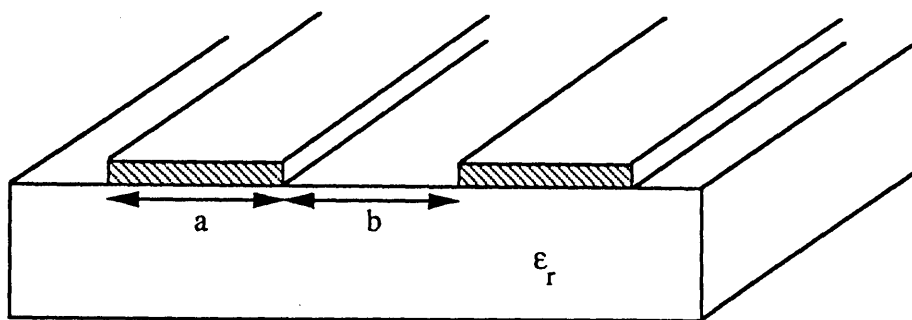


Fig. 4.1. Co-planar electrode structure on a dielectric substrate.

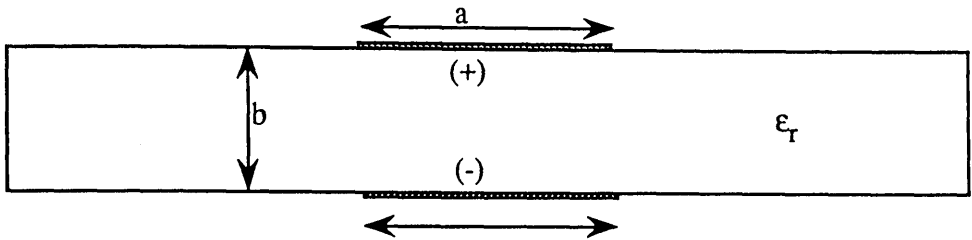


Fig. 4.2. Transmission line : Parallel strips formed on a dielectric sheet.

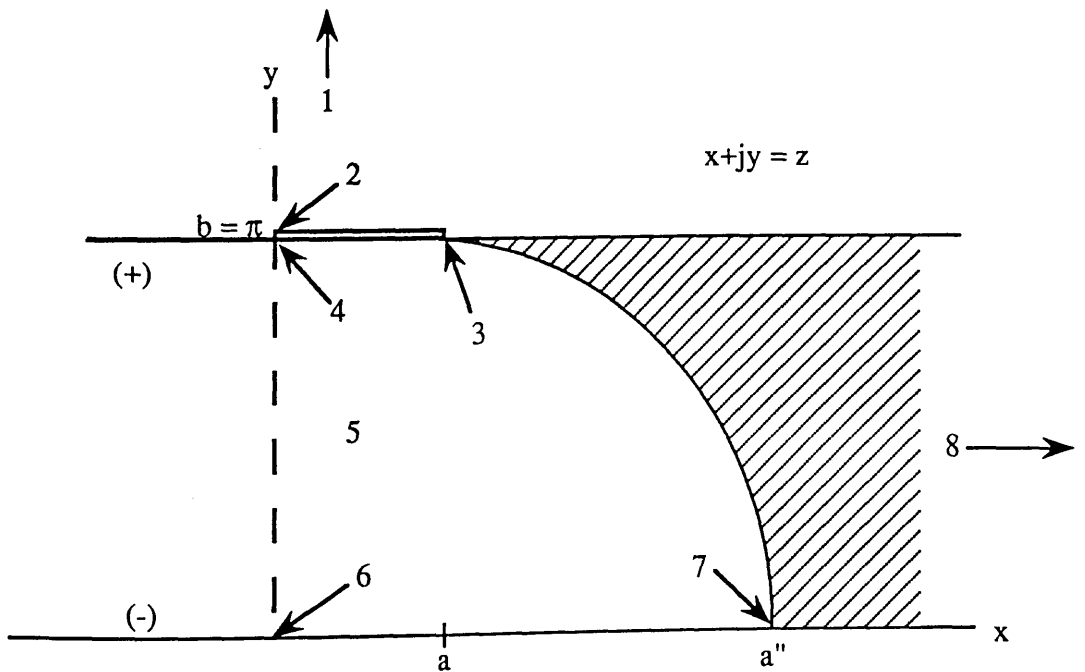


Fig. 4.3. Top left quadrant of transmission line : The main points for mapping are marked 1-8

appendix A. A brief non-technical outline of the method presented by Wheeler is given below, with the minimum amount of analysis used in the derivation presented for the sake of continuity and clarity.

The intention of Wheeler was to present a method by which the transmission line properties of the strip lines might be easily calculated using a calculator or slide rule. Although other more involved computations requiring large computational powers are now possible, e.g. the finite difference method, the conformal mapping technique is more than accurate enough for the present application. The equations resulting from the method presented by Wheeler allow the wave impedance to be calculated quickly and accurately from the width and separation of the strips and the dielectric constant of the separating medium. Similarly the required physical dimensions of the electrodes for a desired wave impedance may be easily calculated using the equations to be presented.

The wave impedance of the transmission line shown in Fig. 4.2 is equivalent to that of the top left quadrant shown in Fig 4.3. The first and most important parameter which requires to be introduced is the shape ratio, i.e the ratio of the strip width, a , to the strip separation, b . The shape ratio, a/b , may be divided into five categories allowing several approximations to be made for each one of the categories.

Very narrow:	$a/b \ll 1$
Narrow:	$a/b < 1$
Square:	$a/b = 1$
Wide:	$a/b > 1$
Very wide:	$a/b \gg 1$

At this point it is necessary to introduce a new parameter g' , which describes the mean effective width of the strip, including the total electric flux on both the outer and inner faces of the strip. It is important to note that the electrode separation, b , is made equal to 2π for ease of derivation.

The conformal transformation selected maps the space coordinates from the z -plane shown in Fig. 4.3 onto the flux-potential coordinates on the z' -plane shown in Fig. 4.4. The most important points are marked from 1 to 8 and an explanation of their significance is given in appendix A. The transformation used is:

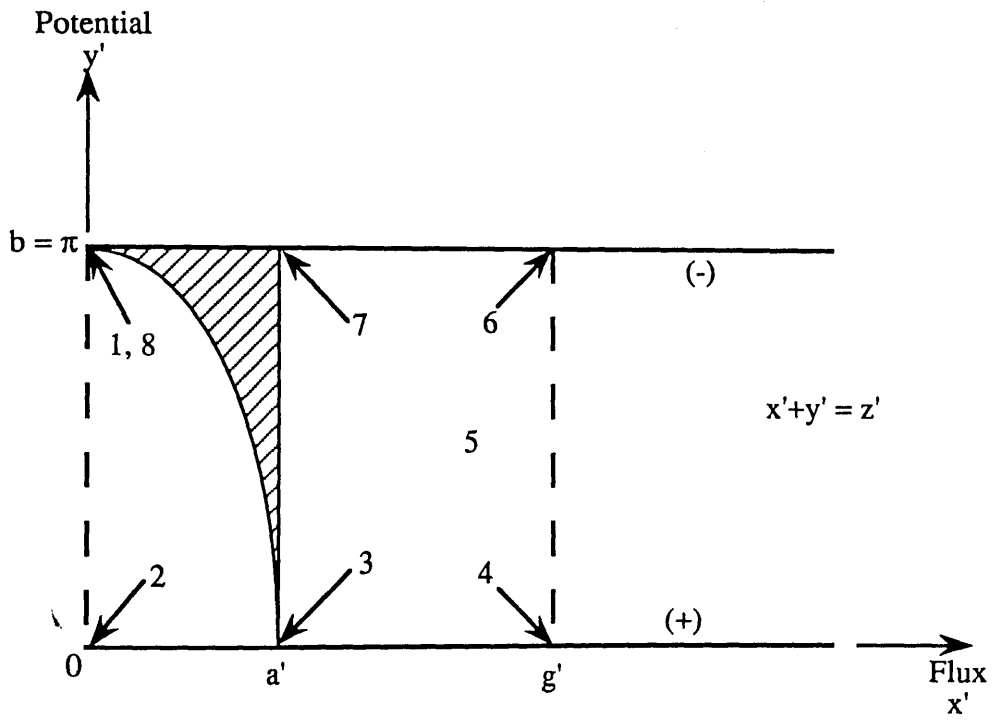


Fig. 4.4. Conformal mapping of Fig. 4.3 onto the flux-potential plane

$$z = j\pi + g' \tanh\left(\frac{z'}{2}\right) - z' \quad (4.1.1)$$

In the z -plane the transmission line corresponds to the classic case of a parallel plate capacitor with an edge effect associated with the fringing field and it is this edge effect which presents the difficulty in solution. In the z' -plane the problem is reduced to a parallel plate capacitor filled with a mixed dielectric. The dielectric-air boundary of the substrate shown in Fig. 4.3 is transformed onto an elliptical curve shown in Fig. 4.4. To the left of the curve is air and to the right is the dielectric substrate. The shaded area just to the right of the curved boundary can be divided into two parts, as shown in Fig. 4.5 (a). With the half separation $b/2=\pi$, the entire area is expressed as $\pi s'$, where s' is the effective width of the area on the x' axis. One part of the area is expressed as $\pi s''$, which effectively adds s'' to the width of the dielectric region to the right of a' and is termed the parallel component. The remainder of the area is $\pi(s'-s'')$ and is effectively in series with the free-space region outside of the dielectric. These series and parallel components can be written in terms of an equivalent parallel width s given by :

$$s = s'' + \frac{(s' + s'')}{\epsilon_r} \quad (4.1.2)$$

The effect of this increment on the effective half width is shown in Fig. 4.5 (b). The effective dielectric constant, ϵ_{re} , can be calculated from the effective filling fraction, q , defined as the ratio of the effective area of the dielectric to the total area of the rectangle.

$$q = \frac{(g' - a' + s)}{g'} \quad (4.1.3)$$

The effective dielectric constant is related to the effective filling fraction by :

$$\epsilon_{re} = (1 - q) + q\epsilon_r \quad (4.1.4)$$

In developing the mathematical approximations for the entire range of the shape ratio it is helpful to work from the extremes of the shape ratio to more elaborate formulae for the intermediate values. To follow the order in which the

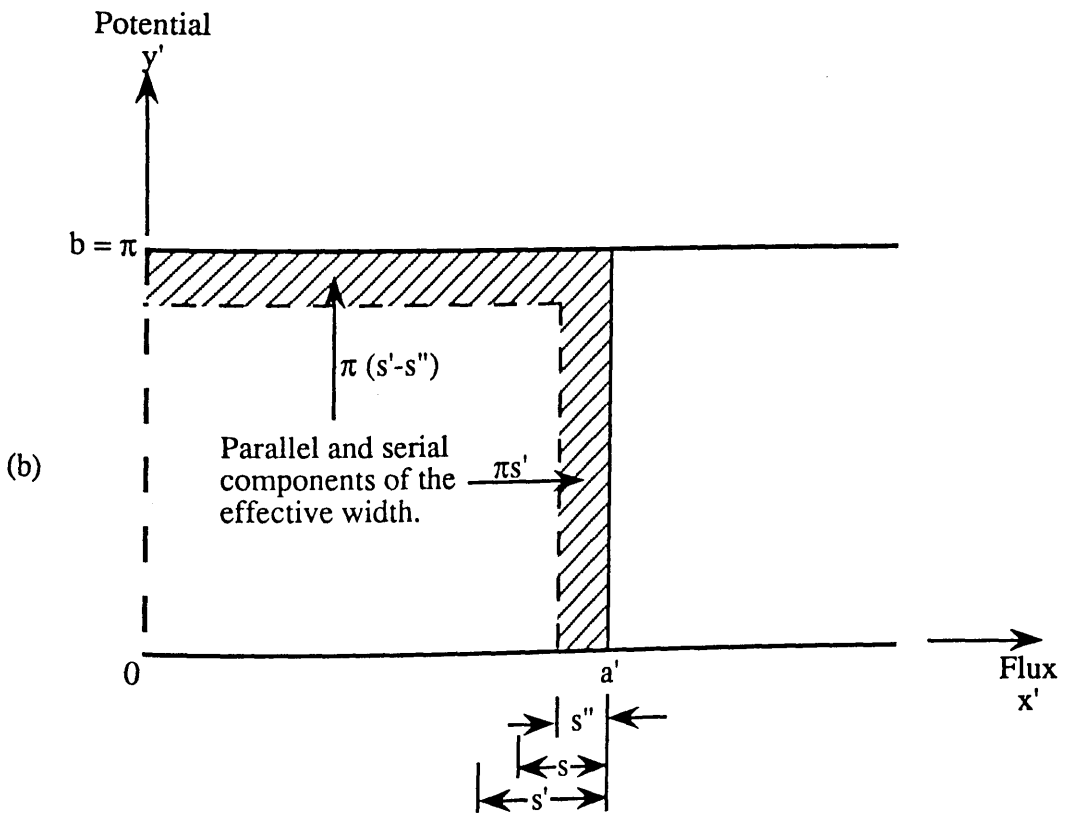
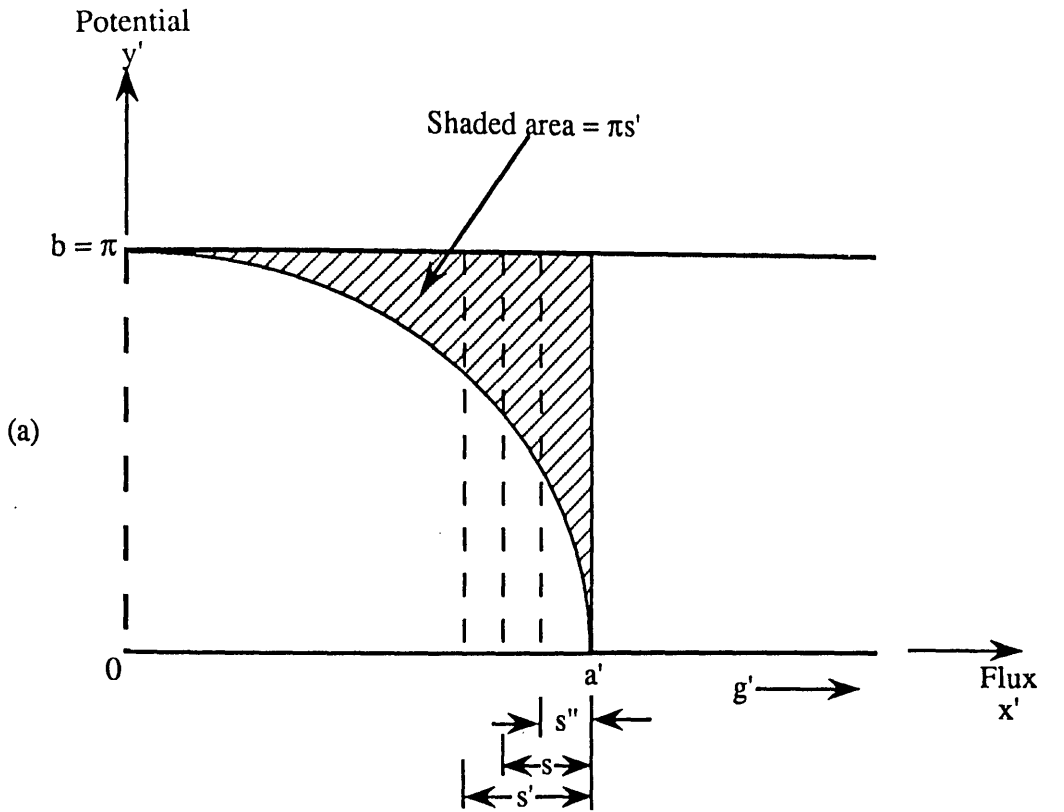


Fig. 4.5. a) Expanded view of extra effective width.
 b) Effective width divided into parallel and serial components.

equations are developed in the appendix, the formula covering wide strips will be looked at first.

4.1.2 Derivation for wide strips.

The free-space resistance R_1 , the inductance L and the free space capacitance C_1 for a pair of wide strips in free space, i.e not separated by a dielectric, can be related to the effective half width g' on the x' plane by

$$R_1 = \frac{R_c \pi}{g'}; \quad g' = \frac{\pi R_c}{R_1} \quad (4.1.5)$$

$$C_1 = \frac{\epsilon_0 l g'}{\pi}; \quad g' = \frac{\pi C_1}{\epsilon_0 l} \quad (4.1.6)$$

$$L = \frac{\mu_0 l \pi}{g'}; \quad g' = \frac{\pi \mu_0 l}{L} \quad (4.1.7)$$

where R_c is the wave resistance of square area of free space, 377Ω , l is the strip length, ϵ_0 is the permittivity of free space and μ_0 is the permeability of free space.

In the problem of a mixed dielectric the free-space resistance and free-space capacitance are dependent upon the effective dielectric constant ϵ_{re} of the entire space surrounding the strips. The inductance is not dependent upon the surrounding medium. The resulting values of resistance and capacitance are :

$$R = \frac{R_1}{\sqrt{\epsilon_{re}}}; \quad C = \epsilon_{re} C_1 \quad (4.1.8)$$

The wave velocity is also reduced by the same ratio as the resistance.

The wave impedance for a wide ($a/b > 1$) pair of parallel strips face-to-face on a dielectric substrate is found from the approximations and derivations presented in appendix A. It is an advantage of the transformation selected by Wheeler that the wave impedance formulae can be written explicitly both for analysis (R in terms of a/b and ϵ_r) and for synthesis (a/b in terms of R and ϵ_r).

The wave impedance for a given electrode width and separation can be found from the relationship:

$$\frac{R}{R_c} = \frac{\sqrt{\frac{1}{\epsilon}}}{\frac{a}{b} + \frac{1}{\pi} \ln 4 + \frac{\epsilon + 1}{2\pi\epsilon} \left[\ln \left(\frac{a}{b} + 0.94 \right) + 1.451 \right] + \frac{\epsilon - 1}{2\pi\epsilon^2} (0.082)}$$
(4.1.9)

The strip-width and separation required for a desired impedance can be found from:

$$\frac{a}{b} = \frac{1}{\pi} (g_\epsilon - 1) - \frac{1}{\pi} \ln (2g_\epsilon - 1) + \frac{\epsilon - 1}{2\pi\epsilon} \left[\ln (g_\epsilon - 1) + 0.293 - \frac{0.517}{\epsilon} \right]$$
(4.1.10)

where g_ϵ is the value of the effective half-width, g' , that would be required if the space were entirely filled with the dielectric material ϵ_r , i.e:

$$g_\epsilon = \frac{\pi}{\sqrt{\epsilon_r}} \frac{R_c}{R}$$
(4.1.11)

The errors in the above equations are estimated by Wheeler¹ to be less than 0.5% for Eq. (4.1.9) and less than 1% for Eq. (4.1.10).

From the equation defining the effective half width, g' , Eq. (A-20) in the appendix, and Eq. (4.1.7) it is possible to write the inductance of the transmission lines as :

$$L = \frac{\mu_0 l}{\left(\frac{a}{b} + \frac{1}{\pi} \left(1 + \ln 2\pi \left(\frac{a}{b} + 0.92 \right) \right) \right)}$$
(4.1.12)

where a is the separation, b is the the width of the strips, l is the electrode length and μ_0 is the dielectric permeability.

Since the capacitance of the strip line is dependent upon the dielectric material separating the strips, the effective dielectric constant must be taken into account when calculating the capacitance. Using Eq. (A-12), Eq. (A-19), Eq. (4.1.2) and Eq. (4.1.3) the effective filling fraction, q , can be written as :

$$\begin{aligned}
q = 1 - \frac{\ln 2(g' - 1)}{g'} + \frac{0.732}{g' \epsilon_r} \ln 2(g' - 1) - \\
\frac{0.732}{g' \epsilon_r} [\text{anti cosh}(0.358 \cosh(\ln 2(g' - 1) + 0.953))] \\
+ \frac{(\epsilon_r - 1)}{g' \epsilon_r} \left(0.386 - \frac{1}{2(g' - 1)} \right)
\end{aligned} \tag{4.1.13}$$

where g' , the effective width, is given by :

$$g' = \frac{a\pi}{b} + 1 + \ln 2\pi \left(\frac{a}{b} + 0.94 \right) \tag{4.1.14}$$

The effective dielectric constant, ϵ_{re} , may then be found from Eq. (4.1.4) and Eq. (4.1.13) and the capacitance of the strips from Eq. (4.1.8) :

$$\epsilon_{re} = (1 - q) + q\epsilon_r \tag{4.1.4}$$

$$C = \frac{\epsilon_{re} \epsilon_0' g'}{\pi} \tag{4.1.15}$$

This completes the derivation of the transmission line properties for wide strips ($a/b > 1$).

4.1.3 Derivation for narrow strips.

A similar approach is used for the derivation of narrow strips ($a/b < 1$), based on free-space formulas and the principles stated for the wide strips. Once more the main body of the following derivation is presented in appendix A with a brief description of the main concepts given below. It is useful to introduce some new parameters more relevant to the narrow strip case. The width parameter g' is replaced by a separation parameter h' . The wave impedance for narrow strips surrounded by free-space is given by :

$$R_1 = R_c \frac{h'}{\pi}; \quad h' = \frac{\pi R_1}{R_c} = \frac{\pi^2}{g'} \tag{4.1.16}$$

The wave impedance for a pair of narrow strips separated by a dielectric sheet is given by:

$$\frac{R}{R_c} = \frac{h_a}{\pi \sqrt{\epsilon_a}} \quad (4.1.17)$$

where h_a is the separation parameter h' that would be present if the space were entirely filled with a dielectric ϵ_a , the average of the sheet and free-space dielectric constants, given by :

$$\epsilon_a = \frac{\epsilon_r + 1}{2} \quad (4.1.18)$$

From Eq. (A-26) and (A-35) defined in the appendix, the separation parameter h' is defined by :

$$h' = h_a + \frac{1}{2} \frac{\epsilon_r - 1}{\epsilon_r + 1} \left(\ln \frac{\pi}{2} + \frac{1}{\epsilon_r} \ln \frac{4}{\pi} \right) \quad (4.1.19)$$

From the inverse of Eq. (A-27), the shape ratio, a/b , in terms of the wave impedance, R , and the dielectric constant, ϵ_r , can be found from :

$$\frac{a}{b} = \left(\frac{1}{4} \exp(h') - \frac{1}{2} \exp(-h') \right)^{-1} \quad (4.1.20)$$

For analysis the wave impedance for narrow strips, $a/b < 1$, separated by a dielectric sheet, can be written in terms of the shape ratio, a/b , and the dielectric constant of the sheet, ϵ_r , as :

$$\frac{R}{R_c} = \frac{1}{\sqrt{\epsilon_a}} \frac{1}{\pi} \left[\ln \frac{4b}{a} + \frac{1}{8} \left(\frac{a}{b} \right)^2 - \frac{1}{2} \frac{(\epsilon_r - 1)}{(\epsilon_r + 1)} \left(\ln \frac{\pi}{2} + \frac{1}{k} \ln \frac{4}{\pi} \right) \right] \quad (4.1.21)$$

The synthesis equation for narrow strips, Eq. (4.1.16) is estimated to have a relative error of less than 0.5 %, while the equation for analysis, Eq. (4.1.17), is estimated to have a relative error of less than 1 %.

The inductance for a pair of narrow strips is independent of the dielectric surrounding the strips and is given by :

$$L = \frac{\mu_0 h'}{\pi} \quad (4.1.22)$$

Substituting the definition of h' , the separation parameter, given by Eq. (A-26) into Eq. (4.1.22) the inductance can be rewritten as :

$$L = \frac{\mu_0'}{\pi} \left(\ln \left(\frac{4b}{a} \right) + \frac{1}{8} \left(\frac{a}{b} \right)^2 \right) \quad (4.1.23)$$

The capacitance, C , for a pair of narrow strips separated by dielectric sheet, ϵ_r , is given by:

$$C = \frac{\epsilon_0' h_a}{\pi \sqrt{\epsilon_a}} \quad (4.1.24)$$

where ϵ_a is the average of the sheet and free-space dielectric constants and h_a is the separation parameter, h' , that would be present if the space were entirely filled with a dielectric ϵ_a . From Eq. (A-26) and (4.1.19) the capacitance can be written as :

$$C = \frac{\epsilon_0'}{\pi \sqrt{\frac{\epsilon_r + 1}{2}}} \left(\ln \frac{4b}{a} + \frac{1}{8} \left(\frac{a}{b} \right)^2 - \frac{\epsilon_r - 1}{\epsilon_r + 1} \left(0.226 + \frac{0.120}{\epsilon_r} \right) \right) \quad (4.1.25)$$

where ϵ_r is the dielectric constant of the sheet and a and b are the width and separation of the strips.

4.1.4 Transmission line properties of co-planar strip lines.

Conformal mapping techniques have been used for a quasi-static analysis of co-planar microwave waveguides by Wen³. Since the co-planar strip lines used for a co-planar electrooptic modulator are complementary to the co-planar waveguides, the analysis developed by Wen may be used to derive the following formulae for the co-planar strip lines shown in Fig 4.1.

$$C = \frac{(\epsilon_r + 1)\epsilon_0 K'(\kappa)}{2 K(\kappa)} \quad (4.1.26)$$

where C is the capacitance per unit length, $K(\kappa)$ is the complete elliptic integral of the first kind, ϵ_r is an average of the principle dielectric constants, for x-cut or z-

cut LiNbO_3 ϵ_r is the average of the ordinary and extraordinary dielectric constants, 44 and 28 respectively⁴.

$$\epsilon_r = \frac{(\epsilon_x + \epsilon_z)}{2} \quad (4.1.27)$$

and

$$\kappa = \frac{b}{b + 2a} \quad (4.1.28)$$

where a is the strip width and b is the separation between the edges of the strip as shown in Fig. 4.1.

Hilberg⁵ has obtained the accurate (to within 3 parts per million) and simple expressions for $K(\kappa)/K'(\kappa)$ shown below

$$\frac{K(\kappa)}{K'(\kappa)} = \frac{1}{\pi} \ln \left[2 \frac{1 + \sqrt{\kappa}}{1 - \sqrt{\kappa}} \right] \quad \text{for } 0.707 \leq \kappa \leq 1 \quad (4.1.29)$$

$$\frac{K(\kappa)}{K'(\kappa)} = \frac{\pi}{\ln \left[2 \frac{1 + \sqrt{\kappa'}}{1 - \sqrt{\kappa'}} \right]} \quad \text{for } 0 \leq \kappa \leq 0.707 \quad (4.1.30)$$

where

$$\kappa' = \sqrt{(1 - \kappa^2)} \quad (4.1.31)$$

Substituting Eq. (4.1.29) and Eq. (4.1.30) into Eq. (4.1.25), the capacitance per unit length is:

$$C = \frac{(\epsilon_r + 1)\epsilon_0}{2} \frac{\pi}{\ln \left[2 \frac{1 + \sqrt{\kappa}}{1 - \sqrt{\kappa}} \right]} \quad \text{for } 0.707 \leq \kappa \leq 1 \quad (4.1.32)$$

$$C = \frac{(\epsilon_r + 1)\epsilon_0}{2} \frac{1}{\pi} \ln \left[2 \frac{1 + \sqrt{\kappa'}}{1 - \sqrt{\kappa'}} \right] \quad \text{for } 0 \leq \kappa \leq 0.707 \quad (4.1.33)$$

Similarly it can be shown that the wave resistance, or characteristic impedance, of parallel co-planar strips on a dielectric substrate is :

$$R = \frac{120}{\sqrt{\frac{\epsilon_r + 1}{2}}} \ln \left[2 \frac{1 + \sqrt{\kappa}}{1 - \sqrt{\kappa}} \right] \quad \text{for } 0.707 \leq \kappa \leq 1 \quad (4.1.34)$$

$$R = \frac{120}{\sqrt{\frac{\epsilon_r + 1}{2}}} \frac{\pi^2}{\ln \left[2 \frac{1 + \sqrt{\kappa'}}{1 - \sqrt{\kappa'}} \right]} \quad \text{for } 0 \leq \kappa \leq 0.707 \quad (4.1.35)$$

The above equations allow for the simple calculation of the characteristic impedance and capacitance of the co-planar electrodes in terms of the physical dimensions of the electrodes and the dielectric constant of the substrate. Since the purpose of the presentation of the above equations for the characteristics of co-planar electrodes was to allow for a direct comparison with the characteristics of transverse electrodes, no equations for the synthesis of the strip width and separation required for a specific characteristic impedance have been presented.

4.1.5 Summary

The formulae presented in sections 4.1.2 and 4.1.3 allow either the synthesis, the derivation of the shape ratio from the wave impedance and dielectric constant, or the analysis, the derivation of the wave impedance or capacitance from the shape ratio and dielectric constant, for the entire range of electrode width and separation. The capacitance and impedance against shape ratio are plotted in Fig 4.6. for both the narrow and the wide strip conditions. The dielectric constant of the dielectric sheet is assumed to be 43, the extraordinary dielectric constant for LiNbO₃.

The objective of sections 4.1.2 and 4.1.3 was to present a series of simple equations by which the transmission line properties could be calculated without the use of intensive computation. These equations provide a quick, easy and accurate estimate of the wave impedance and capacitance for the electrodes of a transverse electrooptic modulator. A more accurate study of the charge on the electrodes and the field distribution could be provided by use of a computational

approach such as the finite difference method. A similar method of conformal mapping was used to derive the equations given above for co-planar electrodes.

4.2 Comparison of operating voltage and figure of merit.

As mentioned previously, one of the main advantages of using transverse electrodes is the nearly uniform electric field through the waveguide (assuming that the LiNbO₃ has uniform conductivity, which may not be the case for proton exchanged waveguides). From Eq. (1.2.12) the voltage required for a radian phase change is :

$$\frac{V}{\text{rad}} = \frac{\lambda b}{R_{mn} \pi L n^3} \quad (4.2.1)$$

where b is the electrode separation, L is the electrode length R_{mn} is the appropriate electrooptic coefficient and n is the refractive index.

For the co-planar electrodes shown in Fig. 4.7 the non-uniform distribution of both the electric and optical fields increases the voltage required for a specific phase shift by a factor called the overlap integral⁶. In Fig. 4.7(a) the optical waveguide is positioned between the two electrodes and E_{\parallel} , the parallel component, is the effective electric field. In Fig. 4.7(b) the waveguide is positioned below one of the electrodes and E_{\perp} , the perpendicular component, is the effective electric field. The waveguide should be positioned so the largest electrooptic coefficient, R_{33} , is employed to alter the refractive index. The cut of the LiNbO₃ would therefore be chosen so that the effective component of the electric field for the electrode configuration lies along the z -axis of the LiNbO₃. The effect of the overlap integral modifies Equation 4.2.1 to

$$\frac{V}{\text{rad}} = \frac{\lambda b}{\Gamma \cdot R_{mn} \pi L n^3} \quad (4.2.2)$$

where Γ is the overlap integral and is dependent upon the electric field orientation and distribution relative to the optical field distribution. Γ is given by⁶

$$\Gamma = \frac{b}{V} \iint E \cdot |E'|^2 dA \quad (4.2.3)$$

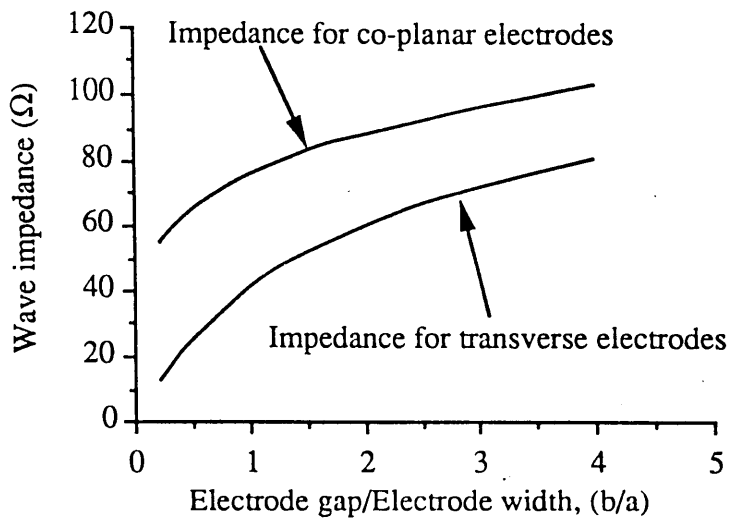


Fig 4.6 (a). Comparison between the wave impedance for transverse and co-planar electrode structures.

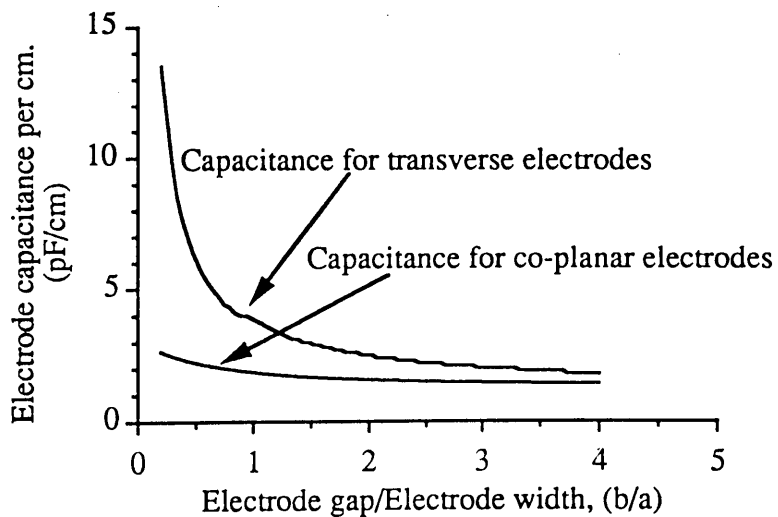
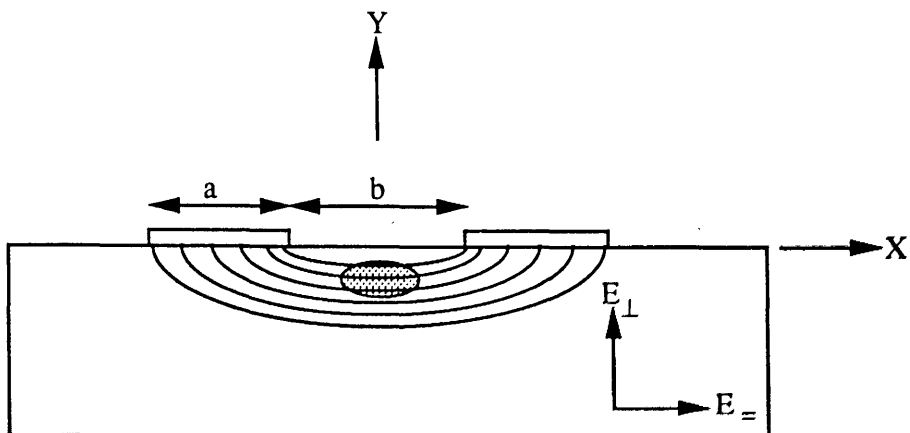
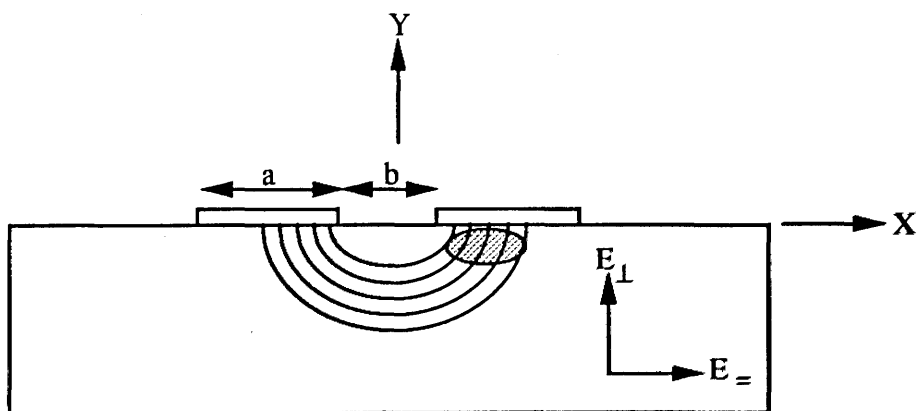


Fig 4.6 (b). Comparison between the electrode capacitance for transverse and co-planar electrode structures.



(a) Waveguide positioned between the electrodes with E_{\parallel} electric field component effective.



(b) Waveguide positioned below one of the electrodes with E_{\perp} electric field component effective.

Fig. 4.7. The two possible positions of the waveguide relative to the electrodes for the co-planar electrode structure.

where E is the spatially varying applied electric field distribution and E' is the normalised optical field distribution.

Marcuse⁷ has studied the dependence of Γ on the position of the waveguide relative to the electrodes, the electrode separation and the orientation of the electric field. The parallel and perpendicular components of the electric field produced from co-planar electrodes on an anisotropic dielectric can be found from⁷

$$E_{=} = \frac{V}{\pi} \frac{\cos\left(\frac{\varphi}{2}\right)}{\left[\left(\left(\frac{b}{2}\right)^2 + y^2 - x^2\right)^2 + (2xy)^2\right]^{1/4}} \quad (4.2.4)$$

$$E_{\perp} = \frac{V}{\pi} \frac{\sin\left(\frac{\varphi}{2}\right)}{\left[\left(\left(\frac{b}{2}\right)^2 + y^2 - x^2\right)^2 + (2xy)^2\right]^{1/4}} \quad (4.2.5)$$

where

$$\tan \varphi = \frac{2xy}{\left(\frac{b}{2}\right)^2 + y^2 - x^2}$$

The optical field profile for titanium indiffused LiNbO₃ waveguides is assumed to have a Gaussian distribution in width and a Hermite Gaussian distribution in the depth direction. Marcuse⁷ uses the 1/e mode intensity full width for the parallel and perpendicular components of the optical field, $W_{=}$ and W_{\perp} respectively, to characterise the distribution. The following conditions concerning the dependency of the overlap integral on the position of the waveguide relative to the electrodes can be drawn from Marcuse for an assumed mode shape ratio of $W_{=}/W_{\perp}=0.5$. For E_{\perp} the maximum overlap integral occurs when the centre of the waveguide is below the inner edge of one of the electrodes. The overlap integral increases as the electrode separation, b , increases, see Fig 4.8(a). For very large electrode separation the overlap integral for E_{\perp} is effectively greater than 1, possibly due to edge effects⁶. For $E_{=}$ the

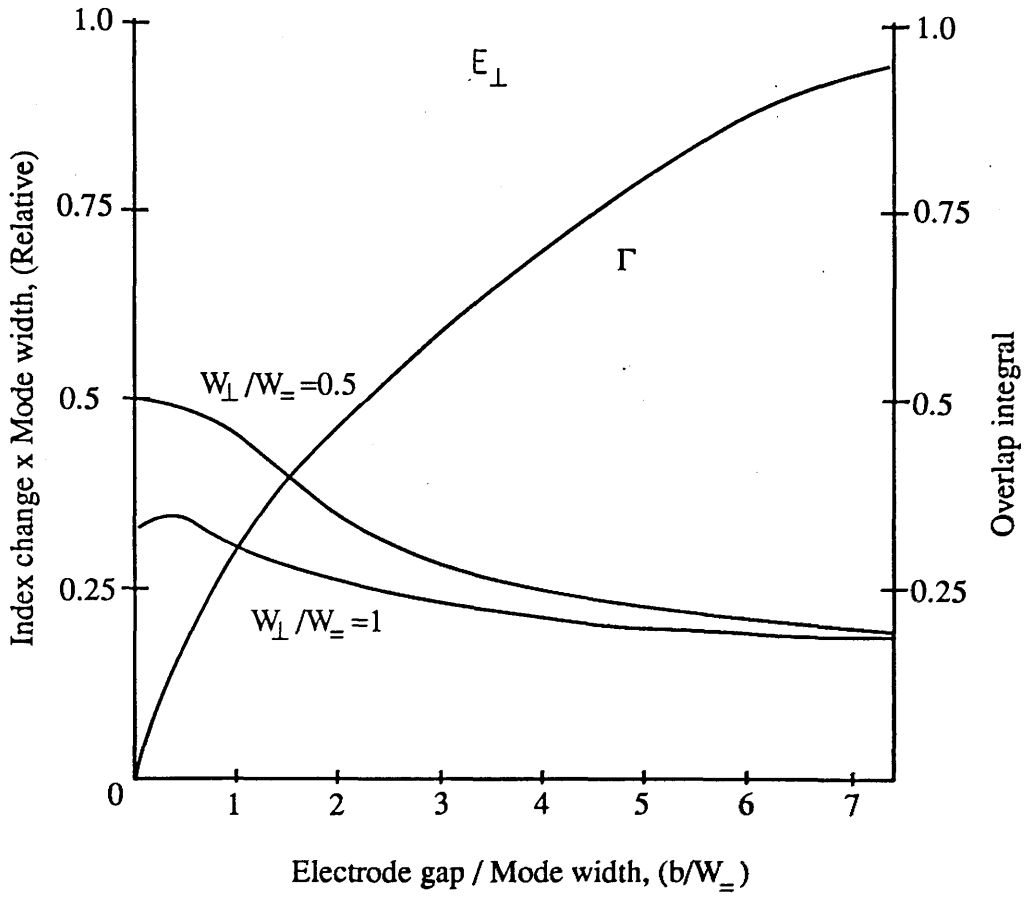


Fig. 4.8(a). Index change.mode width product and overlap integral Vs. Electrode gap / Mode width for the E_⊥ field

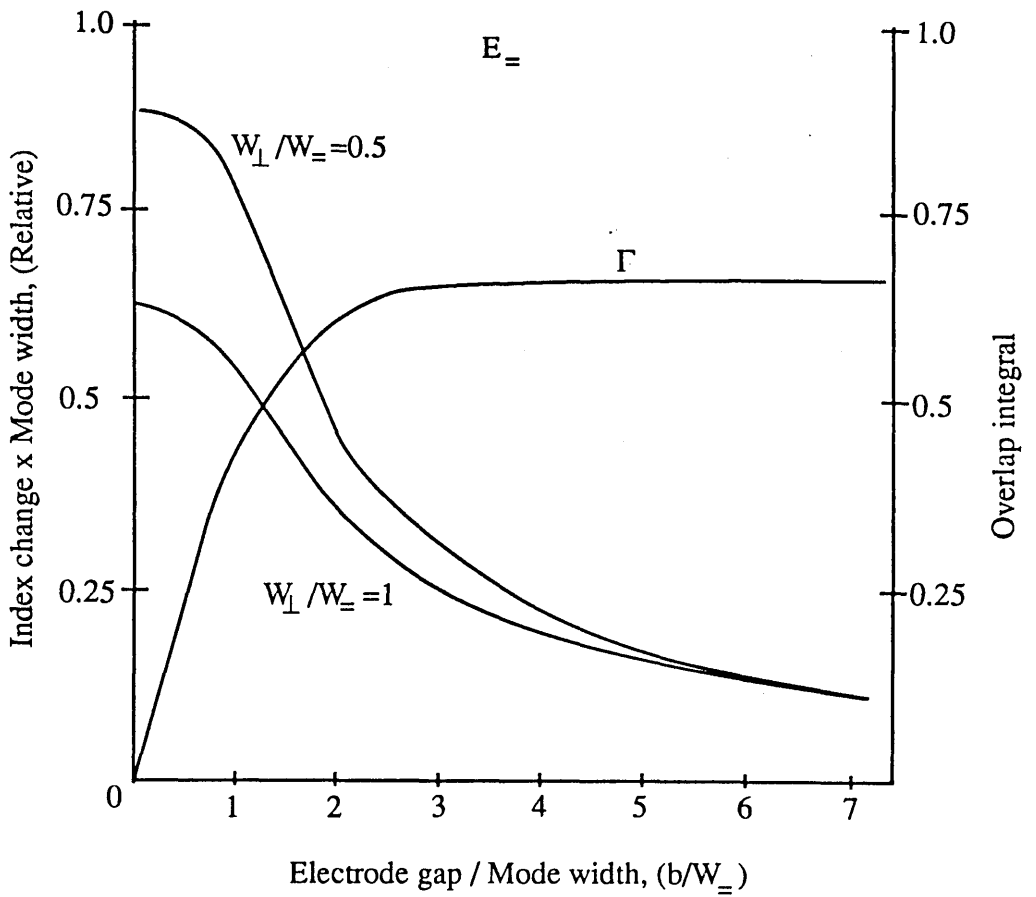


Fig. 4.8(b). Index change.mode width product and overlap integral Vs. Electrode gap / Mode width for the E_{\perp} field

maximum overlap integral occurs when the waveguide is centred between the electrodes. As b increases, the overlap integral increases rapidly until it saturates at $b \geq W_{\parallel}$ where $\Gamma \approx 0.68$, see Fig 4.8(b). Decreasing the mode size has the same effect as increasing the electrode separation. Although for both electrode configurations Γ increases with increasing b , more importantly the induced index change, Δn , is proportional to V/b and therefore decreases with increasing b . Therefore, maximising the overlap integral does not necessarily yield the lowest operating voltage. For small electrode separation E_{\parallel} is more effective than E_{\perp} but Δn drops off more rapidly for E_{\parallel} as b increases. Fig. 4.8 shows the product of the index change and the mode size versus b/W_{\parallel} , the effect of decreasing the mode size increases Δn while also increasing Γ . Optimising the induced index change involves minimising the mode size and using an electrode separation, b , less than $0.5W_{\parallel}$. The electrode separation is less critical for E_{\perp} .

For matching to an optical fibre a more circular mode than the quoted example of $W_{\parallel}/W_{\perp} = 0.5$ is desired to reduce the insertion losses. Unfortunately the induced index change decreases as W_{\parallel}/W_{\perp} increases, thus increasing the operating voltage. For transverse electrodes, which have an overlap integral of 1, the mode shape can, in principle, be readily matched to optical fibres with no increase in the operating voltage.

For example, Kaminow⁸ reported an operating voltage of 0.32 V/rad for a co-planar modulator utilising the parallel component of the electric field with electrodes 23 μm wide, 30 mm long and a separation of 9.3 μm . This corresponds to an overlap integral of approximately 0.6, i.e the electrical field is only 60% effective. Any further increase in the electrode separation would only slightly improve the overlap integral but would give a much larger effect in the reduction of the $\Delta n \cdot W_{\parallel}$ product. A transverse modulator with the same electrode dimensions and electric field completely effective would only require 0.19 V/rad.

4.3 Comparison of bandwidth, figure of merit and microwave properties.

Beside a low operating voltage, other important criteria for the operation of an electrooptic modulator are a high bandwidth, low figure of merit and good microwave properties.

4.3.1 Bandwidth.

The modulation bandwidth for co-planar or transverse lumped electrodes is determined by the smaller of the inverse of the optical or electrical transit times or the time constant of the lumped circuit parameters. The time constant is usually the smaller for a frequency length product less than 2.2 GHz·cm, above which the electrical transit time becomes the dominant effect. The time constant of the lumped circuit parameters is inversely proportional to the capacitance and characteristic resistance of the electrodes. A resistor may be placed in parallel with the electrodes to match the characteristic impedance of the electrodes to that of the driving source, normally 50 Ω. The bandwidth-length product for lumped electrodes is given by :

$$\Delta f = \frac{1}{\pi R C} \quad (4.3.1)$$

where the capacitance, C, is defined by the Eq. (4.1.31) and Eq. (4.1.32) for co-planar electrodes and by Eq. (4.1.15) and Eq. (4.1.24) for transverse electrodes. As mentioned, the characteristic impedance, R, will normally be matched to that of the driving source. If a high drive current is available, the system may be designed for a lower characteristic impedance allowing a higher bandwidth to be achieved. As explained in section 4.5 the structure of the co-planar electrodes gives a lower capacitance and therefore higher bandwidth than transverse electrodes for a small electrode gap to width ratio, but as the ratio increases the bandwidth of transverse electrodes increases at a faster rate than that of the co-planar electrodes and it exceeds it at approximately 3 GHz. Fig. 4.9 shows the bandwidth for both co-planar and transverse electrodes as a function of the electrode gap to width ratio.

A higher bandwidth can be achieved using a travelling wave electrode structure, where the electrodes act as an extension of the driving transmission line. The co-planar travelling wave electrode structure, see Fig 1.4, has been demonstrated by several people to achieve modulation bandwidths in excess of 15 GHz⁹. The modulation bandwidth-length product for a travelling wave electrode structure is given by :

$$\Delta f \cdot L = \frac{2c}{\pi \sqrt{\epsilon_{\text{eff}}} \delta} \quad (4.3.2)$$

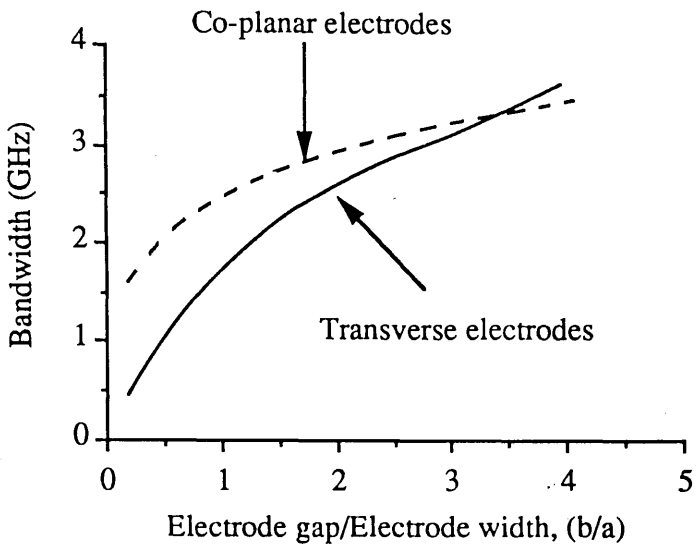


Fig. 4.9. Comparison of bandwidth for transverse and co-planar electrodes.

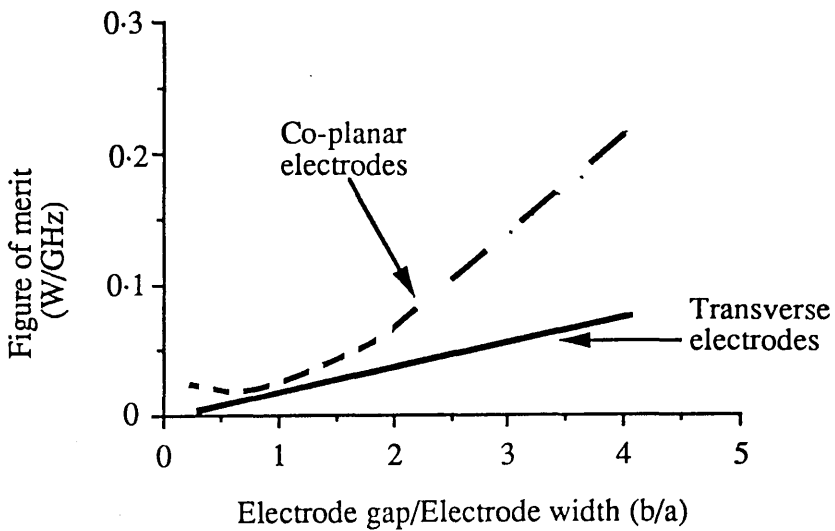


Fig. 4.10 Comparison of the figure of merit for co-planar and transverse electrodes

where c is the speed of light, ϵ_{eff} is the effective microwave dielectric constant, L is the interaction length and δ is a measure of the velocity mismatch between the optical and microwave signals and is given by:

$$\delta = \left(1 - \frac{\sqrt{\epsilon_0}}{\sqrt{\epsilon_{\text{eff}}}} \right) \quad (4.3.3)$$

Since the effective dielectric constant for transverse electrodes is higher than that for co-planar electrodes with the same electrode width and separation, the bandwidth for a modulator with a transverse travelling wave electrode structure is less than that for a co-planar travelling wave electrode structure. The effective dielectric constant for transverse electrodes, ϵ_{teff} , with $a/b > 1$ can be calculated from :

$$\epsilon_{\text{teff}} = (1 - q) + q\epsilon_r \quad (4.3.4)$$

where q is defined by equation 4.1.13. For transverse electrodes with $a/b < 1$, ϵ_{teff} can be calculated (from Eq. (A-33) and (A-26)) as:

$$\epsilon_{\text{teff}} = \frac{(\epsilon_r + 1)}{2} + \frac{(\epsilon_r - 1)}{2 \left(\ln \left(\frac{4b}{a} \right) + \frac{1}{8} \left(\frac{a}{b} \right)^2 \right)} \left(\ln \frac{\pi}{2} + \frac{1}{\epsilon_r} \ln \frac{4}{\pi} \right) \quad (4.3.5)$$

For co-planar electrodes the value of the effective dielectric constant, ϵ_{ceff} , is less dependent upon the electrode strip width and separation. From Gupta et al¹⁰ ϵ_{ceff} can be found from :

$$\epsilon_{\text{ceff}} = \frac{(\epsilon_r + 1)}{2} \left[\tanh \left(1.785 \log \left(\frac{h}{b} \right) + 1.75 \right) + \frac{kb}{h} (0.04 - 0.7k + 0.01(1 - 0.1\epsilon_r)(0.25 + k)) \right] \quad (4.3.6)$$

where

$$k = \frac{b}{b + 2a}$$

The theoretical bandwidth-length product for a transverse travelling wave electrooptic modulator with electrodes 5 μm wide and a 10 μm separation is 7.8

GHz.cm, compared with 9.34 GHz.cm for a co-planar travelling wave electrooptic modulator. The loss in the bandwidth for the transverse travelling wave electrode structure due to the increase in the effective dielectric constant is more than compensated for by a decrease in the required interaction length for transverse electrodes for a specified electrooptic phase shift due to the more efficient interaction between the electrical and optical fields. Assuming an overlap integral of 0.6 (see section 4.2) associated with the co-planar electrodes, an increase of 66% is required in the interaction length to maintain the same phase shift for an applied voltage. The figure of merit, the operating voltage per unit bandwidth, for a travelling wave modulator with the transverse electrode structure reported above is 0.08 V/GHz.Rad compared with 0.103 V/GHz.Rad for co-planar electrodes with an assumed overlap integral 0.6.

4.3.2 Figure of merit.

The figure of merit can be defined as either the operating voltage per unit bandwidth or the operating power per unit bandwidth and is widely used as a measure of the efficiency of the modulator. The lower the figure of merit, the more efficient is the modulator. When comparing the figure of merit for various modulators it is important to remember that the operating voltage will vary depending on the type of modulator, i.e. for a cut-off modulator the operating voltage is the voltage required for 70 % extinction while the operating voltage for a Mach-Zehnder modulator is the voltage required for π phase shift between the two arms of the interferometer. The operating power is merely the square of the operating voltage divided by the impedance of the modulator. Since the source impedance will vary depending upon the application it is often preferable to quote the power per unit bandwidth since this is independent of the source impedance. If a high drive current is available the source impedance may be decreased, which effectively increases the bandwidth and the required operating power of the modulator.

The figure of merit is widely used as a measure of the efficiency of the modulator since an increase in the bandwidth, made at the expense of the operating voltage, by reducing the electrode length or similarly a reduction in the operating voltage made at the expense of the bandwidth, will have no effect on the figure of merit. The required operating voltage for a specified phase shift can be found for co-planar and transverse electrodes from expressions given in

sections 4.2.2 and 4.2.1 respectively and the bandwidth from expressions given in section 4.3.1.

The figure of merit, quoted here as the power per unit bandwidth, for both co-planar and transverse electrode structures is plotted against the electrode gap-width ratio in Fig. 4.10. The figure of merit for the transverse electrode structure is consistently lower than that for the co-planar electrode structure, with the gap between the two values increasing as the gap-width ratio increases. The initial decrease in the figure of merit for the co-planar electrode structure can be attributed to the operating voltage flattening off as the gap decreases, due to the sudden decrease in the value of the overlap integral. As the electrode gap-width ratio increases, the difference in capacitance, and hence bandwidth, for transverse and co-planar electrodes decreases, whilst the difference in the operating voltage increases, and therefore the relative improvement in the figure of merit achieved using transverse electrodes increases.

4.3.3 Microwave properties.

There are several other important advantages of transverse electrodes at microwave frequencies which have yet to be considered. Gupta et al¹⁰ have reviewed the microwave properties of several different types of transmission lines including transverse electrodes or microstrip lines, and co-planar electrodes or co-planar strips. For transverse electrodes the attenuation loss at a modulating frequency of 10 GHz can be improved by as much as twenty times for electrode dimensions corresponding to a characteristic impedance of 50 Ω . The impedance for transverse electrodes has a higher tolerance to errors in the fabrication parameters. The higher effective microwave dielectric constant for the transverse electrodes increases the velocity mismatch between the electrical and optical fields and therefore decreases the bandwidth-length product for a travelling wave modulator, but this is more than compensated for by a reduction in the interaction length due to the increase in the electrooptic effect for transverse electrodes. Other general advantages achieved using transverse electrodes include a higher power handling capability, smaller dispersion and less loss through radiation.

References.

1. Wheeler H. A., "Transmission-line properties of parallel wide strips by a conformal-mapping approximation." IEEE Trans. Microwave Theory Tech. **MTT-12**, 1964, pp 280-289.
2. Wheeler H. A., "Transmission-line properties of parallel strips separated by a dielectric sheet." IEEE Trans. Microwave Theory Tech. **MTT-13**, 1965, pp 172-185.
3. Wen C. P. "Coplanar waveguide: A surface strip transmission line suitable for nonreciprocal gyromagnetic device applications." IEEE Trans. Microwave Theory Tech. **MTT-17**, Dec. 1969, pp 1087-1090.
4. Weiss R. S. and Gaylord T. K. "Lithium niobate: Summary of physical properties and crystal structure." Appl. Phys. **A-37**. 1985. pp 197.
5. Hilberg W. "From approximations to exact relations for characteristic impedance." IEEE Trans. Microwave Theory Tech. **MTT-17**, May 1969, pp 259-265.
6. Alferness R. C. "Waveguide electrooptic modulators." IEEE Trans. Microwave Theory Tech. **MTT-30**, Aug. 1982, pp 1121-1136.
7. Marcuse D. "Optimal electrode design for integrated optics modulators." IEEE J. Quantum Electronics. **QE-18**. March 1982. pp 393-398.
8. Kaminow I. P. Stulz L. W. and Turner E. H. "Efficient strip-waveguide modulator." Appl. Phys. Lett. **27**. Nov. 1975. pp 555-557.
9. Gee C. M., Thurmond G. D. and Yen H. W. "17-GHz bandwidth electro-optic modulator", Appl. Phys. Lett. **43**. December 1983. pp 998-1000.
10. Gupta K. C., Garg R. and Bahl I. J. "Microstrip lines and slotlines" Artech House Inc. (Massachusetts) 1979. pp 296-299.

Chapter 5.

Experimental evaluation of the transverse electrooptic modulator.

The two most important criteria that the transverse modulator should satisfy to provide an attractive alternative to established co-planar modulators are a low operating voltage and high bandwidth. The operating voltage, the voltage corresponding to an electrooptically induced π phase-shift, was measured both using a Mach-Zehnder interferometer and a heterodyne detection system. The electrooptic coefficients for the waveguide were measured using the reciprocal arrangement where the phase-shift, and hence the electrooptic coefficient, was measured for a given applied voltage. The bandwidth of the modulator was calculated from the measured capacitance for electrodes with a 50Ω load resistor. From the theoretical calculations presented in section 4.3.1, the bandwidth of the transverse modulator, with electrodes $20 \mu\text{m}$ wide and separated by $20 \mu\text{m}$, was expected to be in the order of 2 GHz. To measure the bandwidth directly would have required careful microwave packaging and feeding of the modulator. The relationship between the bandwidth and the capacitance is well established and therefore an accurate measurement of capacitance provides a good estimate of the actual bandwidth. A further important criterion for a modulator is the resistance of the waveguide to optical damage or the photorefractive effect. During measurements upon proton-exchanged optical waveguides at moderate power levels, $20 \text{ kW}\cdot\text{cm}^{-2}$, and a wavelength of $0.633 \mu\text{m}$, large instabilities were observed due to both the photovoltaic and photoconductive effects. These observations are detailed below along with the parameters of the modulators measured using the methods mentioned above and a more detailed account of the measurement systems.

5.1 Electrode capacitance and modulator bandwidth.

The theoretical calculations of chapter 4 predict typical capacitance values in the low picofarad range. It was therefore necessary to ensure that any stray capacitance, which would mask the actual capacitance of the electrodes, was eliminated. Once the sample has been packaged ready for electrooptic testing as described in section 3.10, each bonded wire or solder joint would contribute to the capacitance, as would the individual unshielded wires and conducting strips on the mounting board. The use of an Omni-probe 646 probing station enabled

the capacitance to be measured directly across the two bonding pads without having to bond any wires to the pads. The probes were connected to a switching matrix by a short length of unshielded wire. The switching matrix was in turn connected to a Hewlett-Packard 4275A multi-frequency LCR meter which was capable of measuring the capacitance from 10 KHz to 10 MHz. A Keithley quasi-static capacitance meter was also tried in conjunction with the Omni-probe, but proved to be not sensitive enough and the capacitance measured on the same electrodes varied over consecutive measurements.

An x-y-z translation stage allowed the approximate positioning of the sample while a microscope and micrometer control of the probes allowed individual bonding pads to be selected. Care had to be taken when bringing the probes into contact with the bonding pads since the soft aluminium was easily removed by the probes, preventing subsequent bonding to the electrode.

At the low values of capacitance that were being measured it was impossible to ensure that all stray capacitance was physically removed and this would increase the measured capacitance. Several sets of electrodes of varying length and electrode gap were measured using the above technique. The capacitance measured for each electrode pair is presented in Fig. 5.1, in comparison with the theoretical values. The slightly higher values of capacitance measured could be accounted for by stray capacitance in parallel with the electrodes. Likely sources of stray capacitance would be the unshielded cables between the probing station and the switching matrix or an excess length of the co-axial cable connecting the switching matrix to the LCR meter. It can therefore be concluded that the error between the measured and theoretical values, 10%, can easily be accounted for by stray capacitance and a close match to the actual capacitance is, therefore, predicted by the conformal mapping technique. The effect of stray capacitance could have been reduced by the use of shielded cables, i.e. co-axial cables, connecting the probes to the switching matrix and a reduction in the length of the co-axial cable connecting the LCR meter to the switching matrix.

The capacitance per unit length of the electrodes can easily be reduced by decreasing the shape ratio, the electrode width divided by the electrode gap, a/b . In designing the modulator an electrode width of 20 μm was chosen to keep the fabrication as simple as possible. This width was much greater than that required to provide a reasonably uniform electric field over the guide region, but the

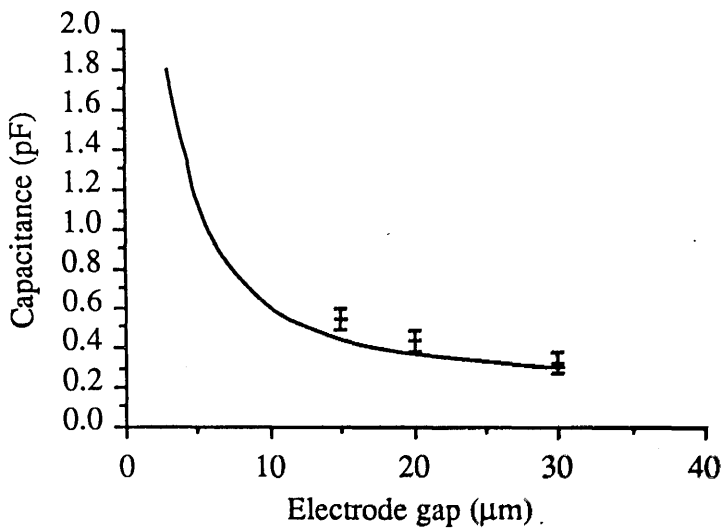


Figure 5.1 Electrode capacitance for transverse electrodes. Electrode width = 20 μm.

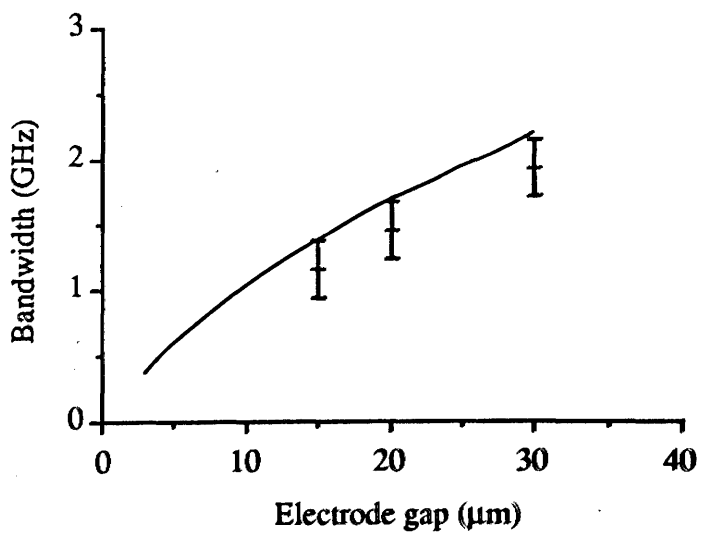


Figure 5.2 Electrode bandwidth for transverse electrodes. Electrode width = 20 μm.

alignment of the relatively wide electrodes with the waveguides was therefore a lot easier and less critical.

Since lumped electrodes were used, i.e the electrode length was less than a quarter of the microwave wavelength at the maximum operating frequency, the bandwidth of the modulator was determined by the electrical charging time, as described in chapter 4. To match the electrode impedance to the source impedance a 50Ω load impedance must be connected in parallel to the electrodes. The bandwidth can be found from

$$\Delta f = \frac{1}{\pi \cdot C \cdot 50} \quad (5.1.1)$$

The bandwidth calculated from the measured electrode capacitance is presented in Fig. 5.2. along with the bandwidth calculated from the theoretical values of capacitance calculated from the appropriate equations presented in section 4.1.2 and 4.1.3. A close match is found between the values of bandwidth calculated from the theoretical capacitance and the values of bandwidth calculated from the measured capacitance.

5.2 Measurement of the operating voltage and electrooptic coefficients.

The electrooptic coefficients, R_{13} and R_{33} , were measured for the waveguides fabricated, using two different techniques of phase-shift detection. The operating voltage that would be required for a π phase-shift was measured, after the electrooptic coefficients had been determined, using the same techniques. The first, and easiest, method of measuring the phase-shift produced by the electrooptic effect was to use an external Mach-Zehnder interferometer. The second method used was to apply an AC modulated electric field to the modulator and use heterodyne detection to calculate the phase-shift. Since only z-cut LiNbO_3 was used, the measurement of R_{33} required the use of TM polarisation and the measurement of R_{13} required the use of TE polarisation.

5.2.1 Measurements using a Mach-Zehnder interferometer.

The Mach-Zehnder interferometer used is shown in Fig. 5.3. The beam was split into a reference beam and a modulation beam using a 50:50 beam-

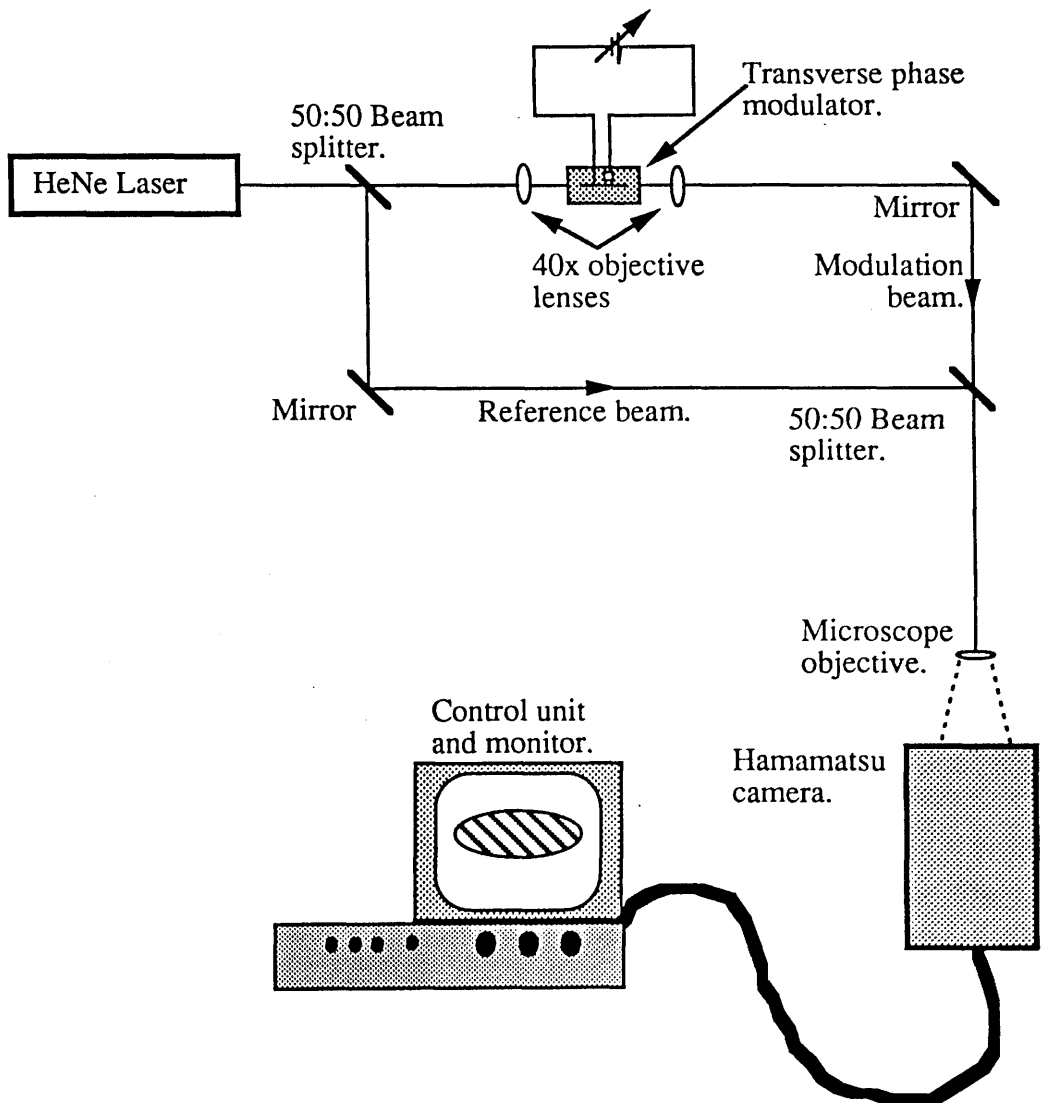


Fig. 5.3. External Mach-Zehnder interferometer used to detect d.c. phase shift.

splitter. The difference between the path lengths that the beams travel must be less than the coherence length of the laser. The coherence length of the laser is the path length that the light can travel before the phase of the light can no longer be predicted, in the order of 30 cm for a multimode 0.633 μm HeNe laser. As the difference in path lengths approaches that of the coherence length of the laser there will be a steady loss in the phase relation between the two beams upon recombination. An end-fire rig was used to couple the modulated beam into and out of the waveguide. Before attempting coupling into the guide, care was taken to align all the components of the interferometer and end-fire rig correctly so as to ensure that the two beams recombined onto the same path.

The light was focused onto the end face of the LiNbO_3 device using a 40x microscope objective. The small dimensions of the waveguide required critical alignment and focusing of the microscope to achieve efficient coupling. The input stage which positioned the input objective was fitted with differential micrometers, allowing positioning to within $\pm 0.1 \mu\text{m}$, to maximise the coupling efficiency. As well as allowing movement in the x- and y-directions the sample stage also allowed the modulator to be tilted and rotated to ensure that the light was launched parallel to the waveguide axis. A second 40x microscope objective focused the output beam onto the observation plane.

With the difference in the path length of the two beams less than the coherence length of the laser and the beams recombining to travel along the same path, an interference pattern was produced at the observation plane. Any change in the phase of either of the two beams produced a shift in the fringe pattern. If the beams recombined along an identical path a circular fringe pattern would be produced and a slight deviation would produce an elliptical fringe pattern. A Hamamatsu camera was placed in the observation plane to monitor the resulting fringe pattern. An optical attenuator was required in the reference path to compensate for the difference in beam intensities due to the various losses between the input and output of the end-fire rig. Any phase change between the two beams resulted in a shift of the fringes, with one complete fringe-shift, from light fringe to light fringe, corresponding to a phase difference of 2π .

The shift in the interference fringe pattern was measured directly on the monitor of the Hamamatsu camera. The Hamamatsu camera was connected to an IBM personal computer which enabled either line or 2-dimensional plots to be stored on the computer. The intensity profile of the fringe pattern could have

been stored from a line plot on the IBM and plotted later. This would have allowed a more accurate determination of the shift in the fringe pattern but might have prevented observation of slower shifts in phase due to optical damage. The extra precision obtained from the plotter was not felt to be significant enough in the overall accuracy of the system to justify its use. By measuring the applied DC voltage required to produce a specified electrooptically-induced phase-shift the electrooptical coefficients could be estimated from Eq. (5.2.1).

$$|R_{mn}| = \frac{\lambda \cdot \Delta\phi}{E \cdot \pi \cdot L \cdot n^3} \quad (5.2.1)$$

where R_{mn} is the relevant electrooptic coefficient, E is the applied electric field, λ is the free-space wavelength, L is the electrode length, n is the relevant refractive index and $\Delta\phi$ is the phase-shift. The electric field was assumed to be orientated purely along the z-axis with a uniform distribution over the optical field.

To assist with the determination of the shift in the fringe pattern a grid was attached to the monitor. The non-uniform nature of the fringes caused difficulty in ascertaining a fraction of a fringe shift with any certainty, although the maximum point was clearly distinguished. The electrooptically induced phase-shift was therefore kept to multiples of 2π , i.e from maximum to maximum, during measurements of the electrooptic coefficients.

The accuracy of the calculation of the electrooptic coefficient was limited by errors in the detection system, errors in estimation of the overlap between the optical and electrical fields and errors in the measurement of the physical dimensions of the modulator. Although the transverse electrodes would have applied an electric field orientated almost purely along the z-axis, there was still a degree of fringing of the field at the edges of the electrodes, resulting in a decrease in the effect of the electric field. To ensure that there was no significant decrease in the effect of the electric field, the width of the electrodes should have been chosen to be at least $2 \mu\text{m}$ wider than the width of the guided mode and the waveguide should be centered below the electrodes. In designing the electrode mask, the width of the electrodes was chosen to be $20 \mu\text{m}$ to ease the alignment between the waveguide and the electrodes. The width of the waveguide mask varied from $4\text{-}7 \mu\text{m}$. It was therefore assumed that there was no reduction in the electrooptic effect due to fringing effects.

During thinning, the thickness of the substrate was checked using a linear voltage differential transformer (LVDT) with an accuracy of $\pm 1 \mu\text{m}$. Although this accuracy was considered acceptable to determine the terminal thickness it could lead to an error of approximately $\pm 10\%$ in the measurement of the electrooptic coefficient at a nominal total thickness of $10 \mu\text{m}$. Therefore, after thinning, the electrode gap or substrate thickness was measured using an optical microscope with a calibrated graticule. At $1000\times$ magnification, each division of the graticule corresponded to a micron and the accuracy to which substrate thickness could be measured was estimated to be within $\pm 0.5 \mu\text{m}$. This corresponded to an error in the measured value of the electrooptic coefficient of approximately $\pm 5\%$ for a $10 \mu\text{m}$ electrode gap. The degree to which the shift in the fringe pattern could be accurately determined was estimated to be within a tenth of a fringe.

Other sources of error outwith the detection system are inherent in the modulator itself. Optical damage could create either a shift in the optical field profile or an induced phase-shift due to changes in internal electric fields. The effect of either would be to create a shift in the fringe pattern not associated with the electrooptically induced phase-shift created by the applied DC field. The optical damage or photorefractive effect was observed for guides fabricated using proton-exchange, where its presence warranted further investigation which will be discussed in detail later. Photorefractive effects were also observed during d.c. experiments on titanium-indiffused guides but were not investigated further.

The Mach-Zehnder interferometer was used to establish the electrooptic phase-shift measured, for applied voltages up to 300 V . An operating wavelength of $0.633 \mu\text{m}$ was used to measure the electrooptic coefficients for both titanium-indiffused waveguides and proton-exchanged waveguides. The titanium indiffused guides were also measured at $1.15 \mu\text{m}$.

5.2.2 Measurement using a heterodyne detection system.

Many of the inaccuracies inherent in or associated with the Mach-Zehnder interferometer were overcome by using a heterodyne system to detect the electrooptic phase-shift. With a good signal-to-noise ratio a more accurate and stable measurement of the phase-shift was possible. Since the change in the

optical field profile and the phase-shift induced through the photorefractive effect are relatively slow, the use of a high frequency (1 MHz) AC applied electrical field removed the error associated with the optical damage from the measured phase-shift. The modulation frequency used with the heterodyne detection system was low enough to ensure that the crystal was not 'clamped'. The clamped condition corresponds to the resonance of the crystal where the strain on the crystal is zero. Smaller electrooptic coefficients would be effective for the clamped condition, since there would be no contribution from the photoelastic effect. For the 'clamped' condition to be effective the modulating frequency would be required to be high enough to create an acoustic standing wave between the electrodes, approximately 300 MHz for a 20 μm thick substrate.

The basic heterodyne system that was used is shown schematically in Fig. 5.4. The beam was split into a reference beam, B_r , and modulation beam, B_m , using a 50:50 beam splitter. Then, using an acousto-optic Bragg cell, the reference beam was modulated at 21 MHz, the intermediate frequency. B_r can be written as :

$$B_r = A_r \text{Cos}((\omega_o \pm n\omega_{if})t + \phi_r) \quad n = 0, 1, 2, 3 \dots \quad (5.2.2)$$

where n is the diffraction order, A is the signal amplitude, ϕ_r is the relative phase, ω_o is the optical frequency and ω_{if} is the intermediate frequency, i.e. 21 MHz. The first-order diffraction beam from the Bragg cell was isolated and mixed with the modulating beam at the detector. As with the Mach-Zehnder interferometer, it is important that the coherence requirements are satisfied for the beams to recombine successfully, i.e. the path difference must be less than the coherence length of the laser and the beams must recombine along the same path. The modulating beam, B_m can be written as :

$$B_m = A_m \text{Cos}(\omega_o t + \Delta\phi_m(t) + \phi_m) \quad (5.2.3)$$

where

$$\Delta\phi_m(t) = \Delta\phi_{m0} \text{Sin}(\omega_m t) \quad (5.2.4)$$

$\Delta\phi_{m0}$ is the peak phase-shift, ϕ_m is the relative phase and ω_m is the modulating frequency for the phase-modulator. As long as the coherence requirements are

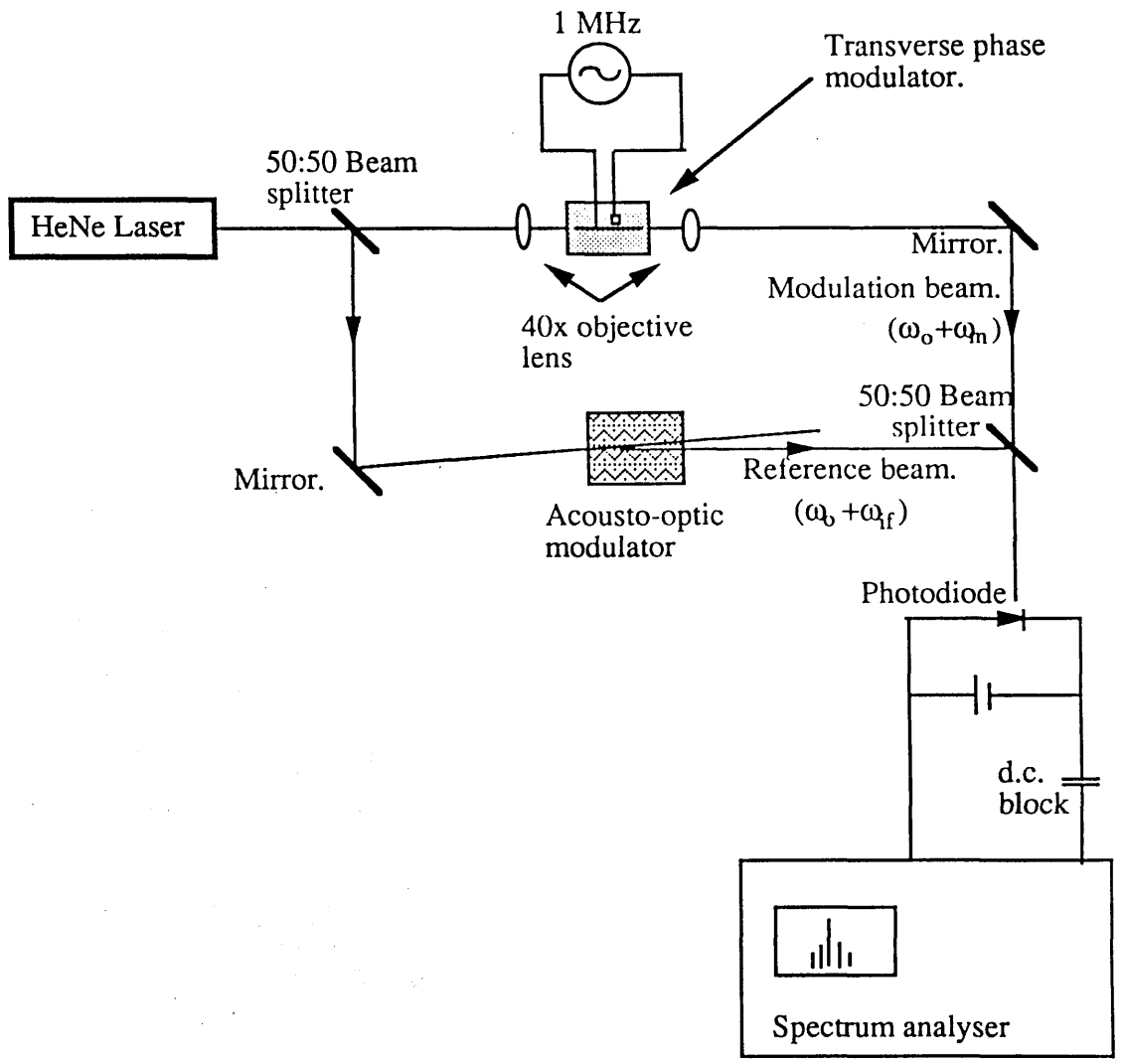


Fig. 5.4. Heterodyne detector used to measure a.c. phase-shift.

satisfied and $\phi_m - \phi_r = \text{constant}$, we can ignore the relative phase term in both beams.

The detector signal is proportional to the instantaneous intensity of the combination of the two beams, i.e. :

$$\begin{aligned} i(t) &\propto [A_r \text{Cos}(\omega_o + \omega_{if})t + A_m \text{Cos}(\omega_o t + \Delta\phi_m(t))]^2 \\ &\propto A_r^2 \text{Cos}^2(\omega_o + \omega_{if})t + A_m^2 \text{Cos}^2(\omega_o t + \Delta\phi_m(t)) \\ &\quad + 2A_r A_m \text{Cos}(\omega_o + \omega_{if})t \cdot \text{Cos}(\omega_o t + \Delta\phi_m(t)) \end{aligned} \quad (5.2.5)$$

$$\begin{aligned} i(t) &\propto \frac{1}{2}A_r^2 [1 + \text{Cos}2(\omega_o + \omega_{if})t] \\ &\quad + \frac{1}{2}A_m^2 [1 + \text{Cos}2(\omega_o t + \Delta\phi_m(t))] \\ &\quad + A_r A_m [\text{Cos}((2\omega_o + \omega_{if})t + \Delta\phi_m(t)) \\ &\quad + \text{Cos}(\omega_{if}t + \Delta\phi_m(t))] \end{aligned} \quad (5.2.6)$$

The bandwidth of the photodetector prevents it from responding to the optical frequency components of the signal, which therefore average to zero. Looking at the second half of Eq. (5.2.6) and ignoring the optical frequency components gives :

$$\begin{aligned} i(t) &\propto A_r A_m \text{Cos}(\omega_{if}t + \Delta\phi_m(t)) \\ &\propto A_r A_m \text{Cos}(\omega_{if}t + \Delta\phi_{mo} \text{Sin}(\omega_m t)) \\ &\propto A_r A_m [\text{Cos}(\omega_{if}t) \text{Cos}(\Delta\phi_{mo} \text{Sin}(\omega_m t)) \\ &\quad - \text{Sin}(\omega_{if}t) \text{Sin}(\Delta\phi_{mo} \text{Sin}(\omega_m t))] \end{aligned} \quad (5.2.7)$$

$\text{Cos}(\Delta\phi_{mo} \text{Sin}(\omega_m t))$ and $\text{Sin}(\Delta\phi_{mo} \text{Sin}(\omega_m t))$ can be expressed in terms of Fourier expansions. The number of relevant terms in the series expansion is dependent on the magnitude of $\Delta\phi_{mo}$.

$$\text{Cos}(\Delta\phi_{mo} \text{Sin}(\omega_m t)) = C_0 + C_2 \text{Cos}(2\omega_m t) + C_4 \text{Cos}(4\omega_m t) + \dots \quad (5.2.8)$$

$$\text{Sin}(\Delta\phi_{mo} \text{Sin}(\omega_m t)) = C_1 \text{Sin}(\omega_m t) + C_3 \text{Sin}(3\omega_m t) + \dots \quad (5.2.9)$$

The coefficients C_n of the Fourier series may be written as Bessel functions of the first kind, where $C_n = J_n(\Delta\phi_{mo})$. Substituting Eq. (5.2.8) and (5.2.9) into (5.2.7) and changing the Fourier coefficients for Bessel functions we have :

$$\begin{aligned}
 i(t) \propto & J_0(\Delta\phi_{mo})\text{Cos}(\omega_{if}t) \\
 & - \frac{J_1(\Delta\phi_{mo})}{2} [\text{Cos}(\omega_{if} - \omega_m)t - \text{Cos}(\omega_{if} + \omega_m)t] \\
 & + \frac{J_2(\Delta\phi_{mo})}{2} [\text{Cos}(\omega_{if} - 2\omega_m)t - \text{Cos}(\omega_{if} + 2\omega_m)t] \\
 & - \frac{J_3(\Delta\phi_{mo})}{2} [\text{Cos}(\omega_{if} - 3\omega_m)t - \text{Cos}(\omega_{if} + 3\omega_m)t] + \dots \quad (5.2.10)
 \end{aligned}$$

The amplitude of the carrier and the sidebands is dependent upon $\Delta\phi_{mo}$. Standard tables and graphs of the values of $J_n(\Delta\phi_{mo})$ are available¹ from which, knowing the relative amplitude of one or more sidebands, the value of $\Delta\phi_{mo}$ can be found. As the phase-shift was increased the sidebands went through several zeros whilst higher order sidebands became progressively more significant. The most accurate point at which to measure the phase-shift was at the zero crossing of a sideband. By measuring the applied voltage required for a particular zero crossing of a sideband the induced phase-shift was found from tables of zero crossings of the Bessel functions and the electrooptic coefficient calculated from Eq. (5.2.1).

The intermediate frequency was fed to the Bragg cell from a signal generator. A function generator was used to modulate the phase of the light, via the transverse electrooptic phase modulator, at a frequency of 0.5-1 MHz. The maximum output from the function generator limited the maximum phase-shift to $5/4 \pi$ radians, i.e just greater than the first zero crossing of the first sideband. The modulation signal was therefore amplified to provide a modulation level capable of producing zero crossings for the first three sidebands.

The optical signal was detected initially using a silicon photodiode connected via a DC blocking capacitor to an r.f. spectrum analyser. The DC blocking 100 pF capacitor was connected in series with the input to the spectrum analyser to eliminate the effect of the photodiode's biasing voltage. A poor signal-to-noise ratio (SNR) led to difficulty in ascertaining accurately the relative amplitude of the sidebands. The problem was further increased due to

interference, apparently due to radiation from the drive sources for the acoustooptic modulator and the phase modulator being picked up by the detector circuit and inductive coupling between the drive and detector cables, which partially masked the true detected signal. To improve the SNR, the signal could be amplified after detection by an operational amplifier or at detection with an avalanche photodiode. The avalanche photodiode was chosen since no operational amplifiers were immediately available with a large enough bandwidth and the amplifier circuit might also have increased the noise level. A Telefunken S 171 P silicon avalanche photodiode with a gain bandwidth product greater than 200 GHz was used. The diode was set up in a photoconductive mode with a biasing voltage of 150 V. The strength of the detected signal was further improved by increasing the amplitude of the first order diffracted beam by using a power amplifier to increase the strength of the i.f. signal to the Bragg cell.

The number of zero crossings that could be measured, usually up to the third zero crossing of the first sideband, was limited by interference picked up from the power amplifier, supplying the modulating signal, at higher voltages. The 21 MHz i.f signal was also picked up by the spectrum analyser from the power amplifier supplying the Bragg cell, preventing a zero crossing of $J_0(\Delta\phi_{mo})$ being measured.

5.3 Results obtained using guides fabricated by titanium-indiffusion.

The transverse electrooptic phase-modulator, with guides fabricated using the titanium-indiffusion process described in section 3.2.1, was tested using the Mach-Zehnder interferometer described above at 0.633 μm and 1.15 μm and the heterodyne phase-detection system at 0.633 μm . It was not possible to detect a strong enough signal at 1.15 μm to enable the measurement of the electrooptic coefficients using the heterodyne system, possibly due to the higher attenuation in the Bragg cell at 1.15 μm . The electrooptic coefficients are presented in Fig. 5.5. The values obtained at 0.633 μm agree closely with values reported previously. No previous publication of values for R_{13} and R_{33} measured at 1.15 μm has been found and so no direct comparison has been made for the values reported here. However values reported for R_{13} and R_{33} at 3.39 μm and other coefficients, namely R_{22} , at 1.15 μm indicate a decrease in the electrooptic coefficient with an increase in wavelength². This is in agreement with the values reported here.

	R_{13}	R_{33}
<u>Titanium indiffused:</u>		
<u>(0.633μm)</u>		
Mach-Zehnder	8.8×10^{-12} m/v	30.5×10^{-12} m/v
Heterodyne	8.7×10^{-12} m/v	30.9×10^{-12} m/v
<u>(1.15 μm)</u>		
Mach-Zehnder	7.5×10^{-12} m/v	28.5×10^{-12} m/v
<u>Proton-exchanged:</u>		
<u>(0.633 μm)</u>		
Mach-Zehnder		23.3×10^{-12} m/v
Heterodyne		22.6×10^{-12} m/v

Fig. 5.5. Measured electrooptic coefficients for titanium indiffused and proton-exchanged waveguides.

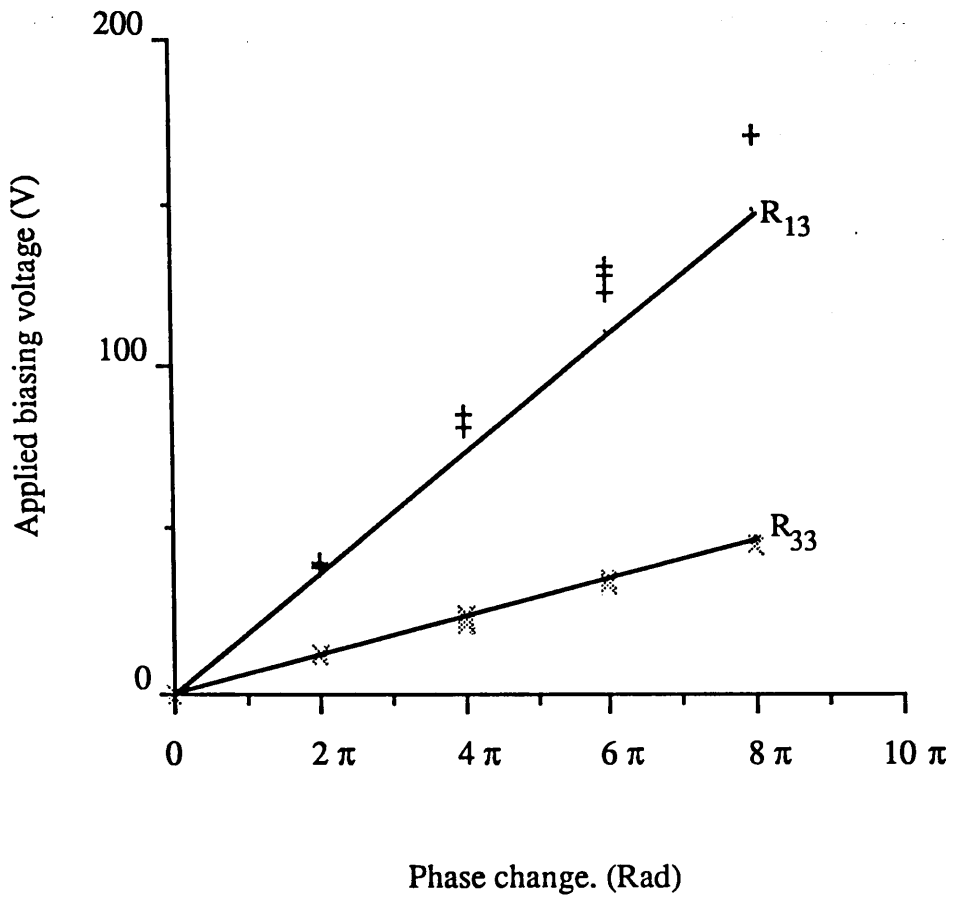


Fig. 5.6. Applied voltage versus phase shift for both the R₃₃ and the R₁₃ coefficients.
 Electrode length = 7.48 mm
 Electrode separation = 23 μm.

Fig. 5.6 plots the measured operating voltage against the phase shift produced through both the R_{13} and the R_{33} coefficients, along with the theoretical values calculated from the measured electrooptic coefficients. It should be noted that the theoretical values of the voltage for R_{13} are extrapolated from measurements of the coefficients made between 0–50 V. the difference between the theoretical voltages and the measured voltages for R_{13} is believed to be due to the very high applied electric fields ($8.7 \text{ V}/\mu\text{m}$) and possible photorefractive effects. No quantitative experiments were run to establish the resistance of the titanium-indiffused waveguides to the photorefractive effect, but no serious degradation in the stability of the detected phase was observed at $0.633 \mu\text{m}$ at optical power densities up to approximately 20 KW.cm^{-2} and an applied DC electrical field of $2.2 \text{ V}/\mu\text{m}$.

5.4 Measurement of the R_{33} electrooptic coefficient in proton-exchange waveguides.

The electrooptic effect in guides fabricated using the proton-exchange procedure described in section 3.2.2 was measured at $0.633 \mu\text{m}$. Both the Mach-Zehnder interferometer and the heterodyne system were used for detecting the phase-shift. The waveguides were not capable of supporting guided modes at $1.15 \mu\text{m}$ and consequently no measurements of the electrooptic coefficient were possible. Since proton-exchange increases only the extraordinary index, the combination of the transverse electrode design and the use of proton-exchange to fabricate the waveguides means only z-cut LiNbO_3 could be used. Since the TE polarisation is not supported, the R_{13} coefficient becomes practically redundant and only the R_{33} electrooptic coefficient was effective. The use of x-cut and y-cut LiNbO_3 would require a non-zero value for the R_{31} and R_{32} coefficients respectively.

While using the Mach-Zehnder measurement system, the guided-mode intensity profile was observed to undergo severe drifting due to photorefractive effects, making it hard to obtain a reliable figure for R_{33} . Immediately upon application of the bias the mode would start to drift and cause a shift in the fringe pattern. There was also the possibility of the internal electric field across the guiding region, created by the photorefractive effect, being in the opposite direction to the applied field, creating a reduced electrooptic phase-shift. By using a high frequency modulating field ($0.5\text{--}1 \text{ MHz}$) with the heterodyne

system any phase-modulation or mode-drifting due to the photorefractive effect would be too slow to be detected. The values quoted from measurements obtained using the Mach-Zehnder system were calculated from the phase-shift measured immediately on application of the biasing field. After application of the biasing field there was a gradual reduction in the electrooptically induced phase-shift due to the internal induced electric field through the photorefractive effect. The photorefractive effect in the proton-exchange guides is examined in more detail in the following section.

The values of R_{33} measured using each system are reported in Fig. 5.5. Both sets of measurement are in close agreement with the values reported by Loni et al¹² using the same proton-exchange waveguide fabrication procedure.

5.5 Evaluation of the photorefractive effect in proton-exchanged waveguides.

5.5.1 Index instabilities in proton-exchanged guides and the mechanics of the photorefractive effect.

To understand and evaluate fully the photorefractive effect in the proton-exchanged guides it is necessary to understand both the physical nature of the proton-exchange process and the mechanics of the optically induced change in the refractive index.

The formation of a proton-exchanged guiding region was discussed in detail in chapter 2. By immersing the LiNbO_3 substrate into a bath of molten benzoic acid there is an exchange between the Li^+ ions and the hydrogen ions from the acid³. The protons may only occupy interstitial sites⁴ since the small atomic size of the protons prevents the occupation of the substitutional site of the Li^+ ion. One initial problem of guides fabricated using benzoic acid was the instability of the guides with both temperature and time. This could be caused by the small size and high mobility of the protons allowing them to migrate over extended periods of time⁵. A second problem was the instability of the waveguide under an applied DC electric field⁶. This could result in the extinction of the guided mode over a period in the order of one minute. Removal of the applied field resulted in a slower return of the light into the guide region, with a reverse in bias increasing the rate of recovery. It is possible to reduce the temporal instabilities in the index profile by either annealing the guides after

exchange or the use of a buffered melt, i.e. benzoic acid containing small amounts of lithium benzoate, or a combination of both. The use of a dilute melt and annealing also improves the DC stability and attenuation whilst also altering the index profile from an approximately step-index profile to a deeper, more graded-index profile⁴. There could be at least two possible sources for the instabilities observed in the proton-exchange guides, the photorefractive effect as observed in virgin LiNbO₃, or the drifting of protons within the guiding region under the action of an applied electric field. A combination of both effects is perhaps more probable and would account for the difficulty in quantifying the fluctuations in the refractive index.

Optically induced inhomogeneities due to the photorefractive effect in LiNbO₃ were observed by Ashkin et al⁷. The presence of the photorefractive effect is highly detrimental for integrated optical applications. Ashkin et al observed that upon exposure to a gas laser at 0.5145 μm and 0.6328 μm with a few milliwatts output power there was a change in the extraordinary refractive index by as much as 2×10^{-4} . Light at the longer wavelengths of 1.1526 μm and 1.06 μm did not produce any inhomogeneity in the crystal. If the change in the refractive index was produced by the electrooptic effect it would correspond to an applied internal field of approximately 10 KV/cm. Heating the sample increased the relaxation rate of the index inhomogeneities.

The photorefractive effect^{7,8} can be divided into two components, a photovoltaic effect and a photoconductive effect. The photovoltaic effect is present in the absence of an applied field and can be attributed to impurities or defects in the LiNbO₃ crystal. It is proportional to the optical absorption coefficient and inversely proportional to the total material conductivity. Carriers in the form of electrons are excited from the Fe²⁺ impurities present in the substrate and drift to the edge of the illuminated region where they are trapped. This charge separation creates a space-charge field which causes an alteration in the refractive index through the electrooptic effect. The photoconductive effect is also due to the drifting of photoexcited carriers from the Fe²⁺ impurities in the illuminated region, but this time under the application of an applied field. Since the carriers will drift in the direction of the applied field, a second field will be created across the illuminated region in the opposite direction to the applied field, thereby reducing the electrooptic effect. Past studies on the photorefractive effect for waveguides formed by proton-exchange have shown a reduction from the effects observed in virgin LiNbO₃ substrates, in both the photoconductive and

photovoltaic effects⁹. This could be attributed to the higher conductivity of the exchanged region, any photoexcited carriers not becoming trapped and no space-charge build-up occurring. Guides formed by titanium indiffusion show an increase in the optical damage from that present in virgin LiNbO₃ substrates.

The instability of guides fabricated by proton-exchange was recognised as a problem soon after the development of the proton-exchange technique. Yi-Yan observed a day-to-day oscillatory evolution of the effective mode indices in guides fabricated by proton-exchange in pure benzoic acid. The maximum observed change in refractive index was 0.0025 for a single mode guide exchanged for 1/2 hour. An increase in the exchange time led to a decrease in the magnitude of variation in the refractive index although even for long exchange times, e.g. 38 hrs, the variation did not disappear totally although the small variations reported may have been due to photorefractive effects. Yi-Yan attributed the evolution in the index profile to a continuous migration of the protons, due to their small size and relatively high mobility, within the guiding layer. Jackel¹⁰ studied the effects of using dilute melt benzoic acid and post-exchange annealing upon the short and long term stability of the guides. The short term instabilities were attributed to the formation of metastable phases but no clear evidence of this has been shown. Both annealing and the use of dilute melt benzoic acid were used to increase the stability of the guides. The effect of both is to reduce the concentration of protons in the exchanged region. Guides fabricated using 3.4 Mole % lithium benzoate in benzoic acid showed no index change over a period of several days¹⁰. De Micheli¹¹ et al observed similar effects in proton-exchanged guides fabricated at high temperatures (300 °C). The use of infrared absorption on x-cut LiNbO₃ substrates following exchange in pure benzoic acid by Loni et al⁴ showed the presence of a broad unpolarised peak shifted towards lower frequencies from the sharp polarised peak at 3510 cm⁻¹ which corresponds to the free OH group. Similar measurements on z-cut LiNbO₃ substrates showed the presence of only the sharp peak at 3510 cm⁻¹. This broad peak is due to the presence of a hydrogen-bonded OH group⁴, a hydrogen-ion sharing its bond with two oxygen ions. Polarisation measurements indicated that free OH groups were constrained to vibrate in the (x,y)-plane. After annealing the x-cut sample at 250 °C for 0.5hr there was a significant reduction in the intensity of the infrared absorption band due to the hydrogen bonded OH groups while the band due to the free OH groups was unchanged. Guides fabricated in dilute melt benzoic acid showed a similar reduction in the broad peak. Loni et al suggested that the hydrogen-bonded OH group may be

responsible for the undesirable effects associated with proton-exchanged waveguides, i.e. device instabilities such as d.c. drift, since they are not as tightly bonded as the free OH group. The number of hydrogen-bonded OH groups present in the exchanged region can be reduced either by annealing or by exchanging in dilute melt benzoic acid. De Micheli et al suggested that the interstitial protons may also be responsible for the observed reduction in the electrooptic coefficient since the conductivity of the crystal is increased, which will reduce the effect of the applied electric field. Such an increase in conductivity would reduce the photorefractive effect since the optically induced charge within the crystal will have a smaller effect. This is in keeping with Jackel's¹⁰ observation of low optical damage for waveguides fabricated by proton-exchange in 1 Mole % dilute benzoic acid without annealing.

As well as variations in the effective mode indices on a day-to-day basis, Jackel observed that the depth of the guides increases over a long period of time i.e a guide originally 5.5 μm deep was reported by Jackel to be about 0.25 μm deeper after 18 months. Jackel has claimed that the long term stability of the guides can be improved by increasing the lithium benzoate concentration in the benzoic acid. This decreases the diffusion coefficient of the protons. A guide fabricated with a dilute melt of 3.4 Mole % lithium benzoate will have a diffusion coefficient of $8.8 \times 10^{-3} \mu\text{m}^2/\text{hr}$ as opposed to $1.37 \mu\text{m}^2/\text{hr}$ for pure benzoic acid¹⁰. Comparing the diffusion coefficients Jackel concluded that any significant drift in the protons would take over 100 times longer for the samples fabricated in the dilute melt.

Recently there have been two alternative procedures published^{12,13} to achieve low loss guides with a substantially restored electrooptic effect by reducing the concentrations of protons. In the first method, reported by Loni et al, guides were fabricated by exchanging in 1% melt benzoic acid at 235 °C for 4 minutes followed by annealing at 275 °C for 30 minutes and 375 °C for 15 minutes. The second method, reported by Suchoski et al, fabricated the guides by exchanging in pure benzoic acid for 10-30 minutes at 200 °C followed by annealing at 350 °C for 2-4 hours depending on the wavelength of operation. Although the two methods are slightly different the end result is similar, with annealing used to control the concentration of protons in the guiding region. The first method introduces a very localised area of proton-exchange which is incapable of guiding till after annealing and the annealing then diffuses the protons into the substrate to form the guide. From the infrared spectroscopy

measurements reported by Loni et al⁴, both methods should result in a reduction in the number of OH groups being hydrogen-bonded. As mentioned a restoration of the electrooptic effect was reported for both values with a value of 24×10^{-12} m/V reported for the first method and 30×10^{-12} m/V for the second, but Suchoski et al measurement's may well be wrong due to the assumed value of the overlap integral used in the electrooptic calculations. The guides fabricated using the second method were measured by Suchoski at both $0.633 \mu\text{m}$ and $1.15 \mu\text{m}$ on both x- and z-cut with no reduction in the electrooptic coefficient at the longer wavelength. This is inconsistent with the values reported here for the R_{13} and R_{33} coefficients for Ti indiffused guides and for the R_{22} coefficient reported elsewhere². The large possible errors in Suchoski et al's estimates probably hide this expected decrease in value of the coefficients. Both methods produced guides with very low losses, in the region of 0.2 dB/cm. Another important common point between the two methods is the absence of any reported instabilities due to the photorefractive effect.

5.5.2 Instabilities in proton-exchanged waveguides observed using a transverse electrooptic phase modulator.

Proton-exchanged waveguides were fabricated using a method essentially equivalent to that described by Loni et al. The LiNbO_3 sample was masked to define stripe windows 4 to 7 μm wide. The samples were immersed in a melt made up from 1 Mole % lithium benzoate in benzoic acid at 235°C , for 4 minutes, followed by annealing for 45 minutes at 375°C . The proton-exchanged stripes were not capable of supporting guided light at $0.633 \mu\text{m}$ before annealing. During the fabrication process, only the subsequent deposition of the SiO_2 buffer layer would be likely to result in any further annealing.

In the absence of an applied electric field the guides supported a single TM mode. A $0.633 \mu\text{m}$ HeNe laser with a measured output power of 5 mw was used to test the stability of the guides. Any change in the effective index of the guide was monitored using the external Mach-Zehnder interferometer, previously described, in conjunction with the Hamamatsu camera. The intensity of the light in and around the guide was monitored using the Hamamatsu camera. In the absence of an external applied field, the guides initially showed little change in the effective refractive index, with slight variations in phase settling after a short period. Taking into account losses associated with the

microscope objective used for launching the light, the spot size and Fresnel losses at the waveguide ends, the estimated power coupled into the waveguide was approximately 20 KW.cm^{-2} . A bias of 50 V, equivalent to an electric field strength of 2.5 MV/m, was applied across the guide whilst changes in the mode profile with time were observed on the Hamamatsu camera. Immediately on application of the 50 V bias, the guided mode decreased in intensity, with the light in the substrate below the guide increasing in intensity. After approximately 1 minute there was almost no guided light in the proton-exchanged region. The maximum phase-shift under a constant biasing voltage measured using the Mach-Zehnder interferometer was 6π . This was measured 1 min 45 sec after the application of the biasing voltage and corresponds to an index change of 0.27×10^{-3} . After a further 14 minutes the guiding effect appeared to be fully restored to the proton-exchanged region, after which the light slowly drifted from the proton-exchanged region back to the substrate and then back to the surface region again with the period of the oscillation taking longer each time. If, during such cycles, the input coupled light was removed, there was no apparent change in the refractive index distribution until the light was fully restored. After approximately one hour the light stabilised in the proton-exchanged region, with only small fluctuations in intensity. Line scans of the intensity of the light across the LiNbO_3 substrate and through the center of the waveguide were taken from the Hamamatsu camera using an IBM PC at various intervals. Figs. 5.7(a)-(f) show the intensity profiles at selected time intervals in the migration of the guiding.

Once the light had stabilised in the proton-exchanged region the light was removed for 15 minutes. When the light was returned to the guide similar effects were observed as before with the light initially moving relatively rapidly from the guide to the substrate before once more stabilising in the guide after approximately 1 hour. The exact behaviour of the drifting of the optical mode appeared to be dependent upon the previous exposures of the LiNbO_3 sample to light. The time for the first oscillation of the light from the proton-exchanged region to the substrate and back varied from one exposure to the next but it was not possible to characterise these variations systematically.

The above observations can be explained by considering the photorefractive effect with apparently little contribution from protonic drift. If protons were drifting in the exchanged region it would be expected that the drifting would be more stable, with a less oscillatory nature. In the presence of

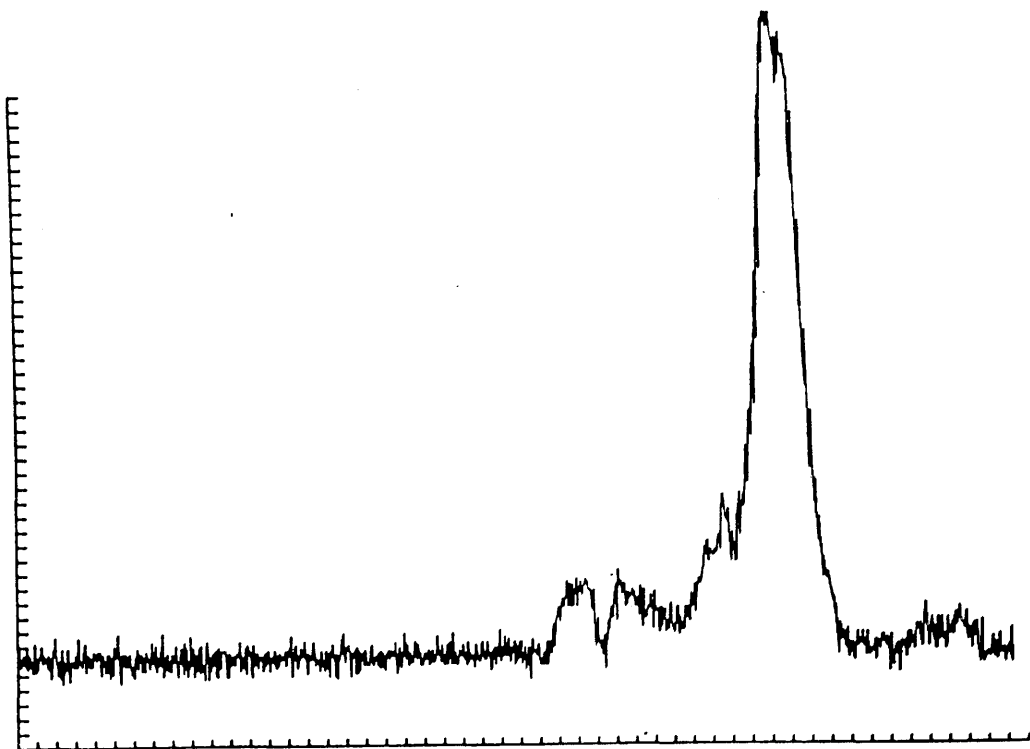


Fig. 5.7(a). Intensity profile through the guide and across the substrate before application of the biasing voltage.

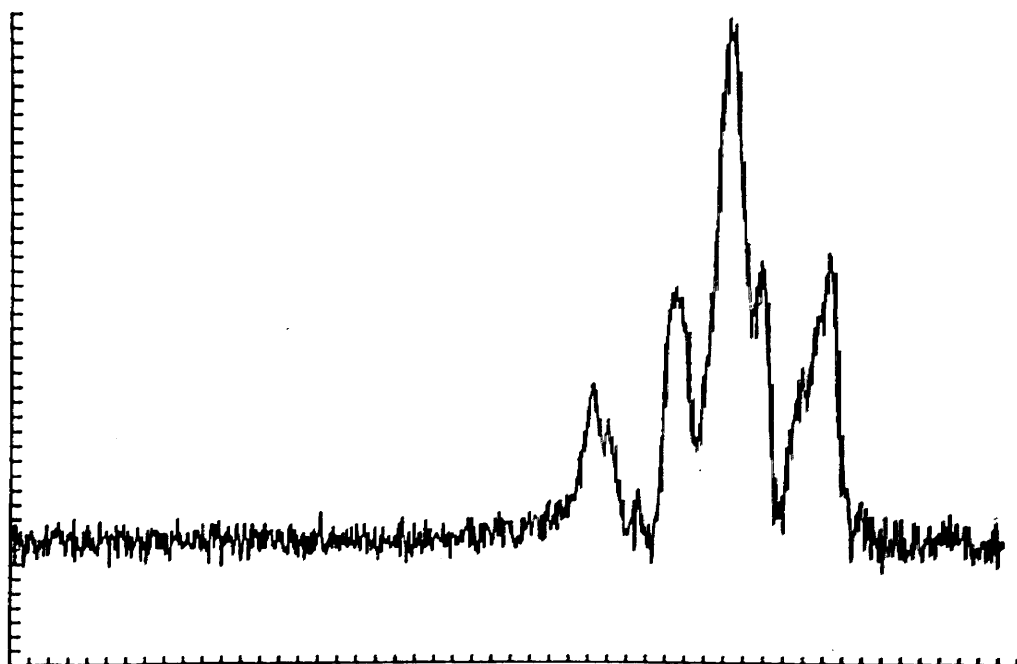


Fig. 5.7(b). Intensity profile through the guide and across the substrate 30 seconds after application of the biasing voltage.

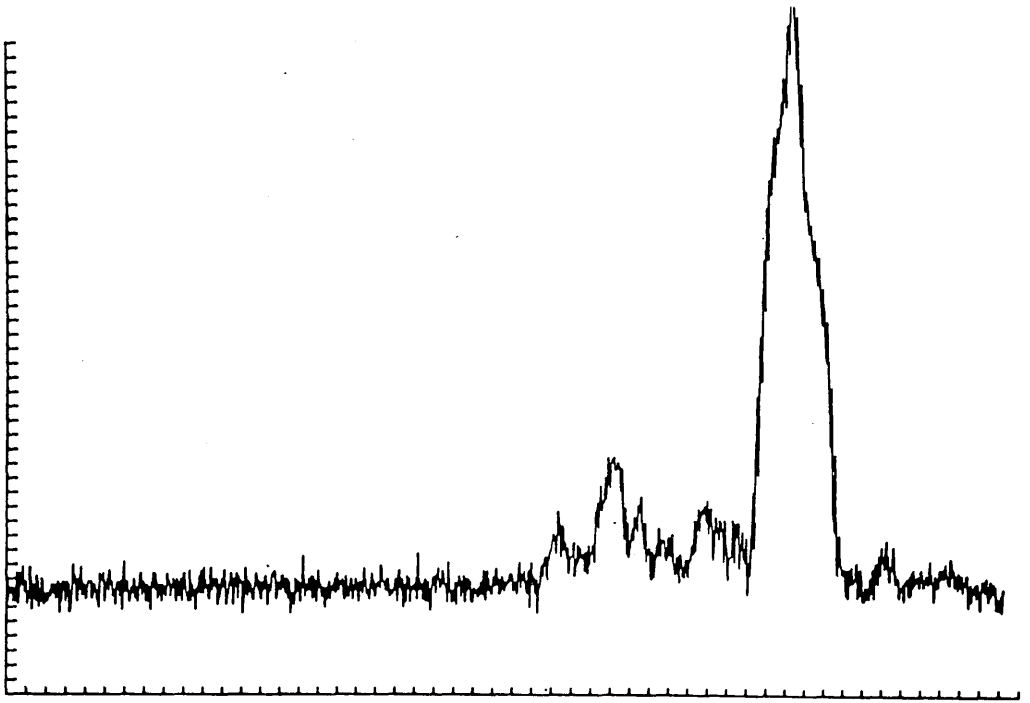


Fig. 5.7(c). Intensity profile through the guide and across the substrate 15 minutes after application of the biasing voltage.

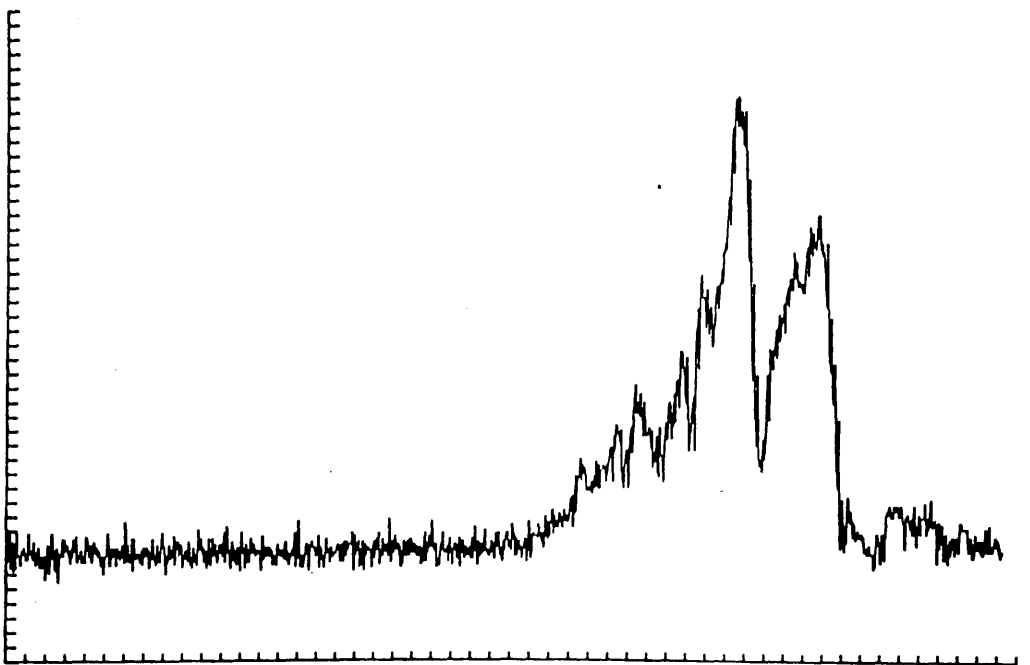


Fig. 5.7(d). Intensity profile through the guide and across the substrate 22 minutes after application of the biasing voltage.

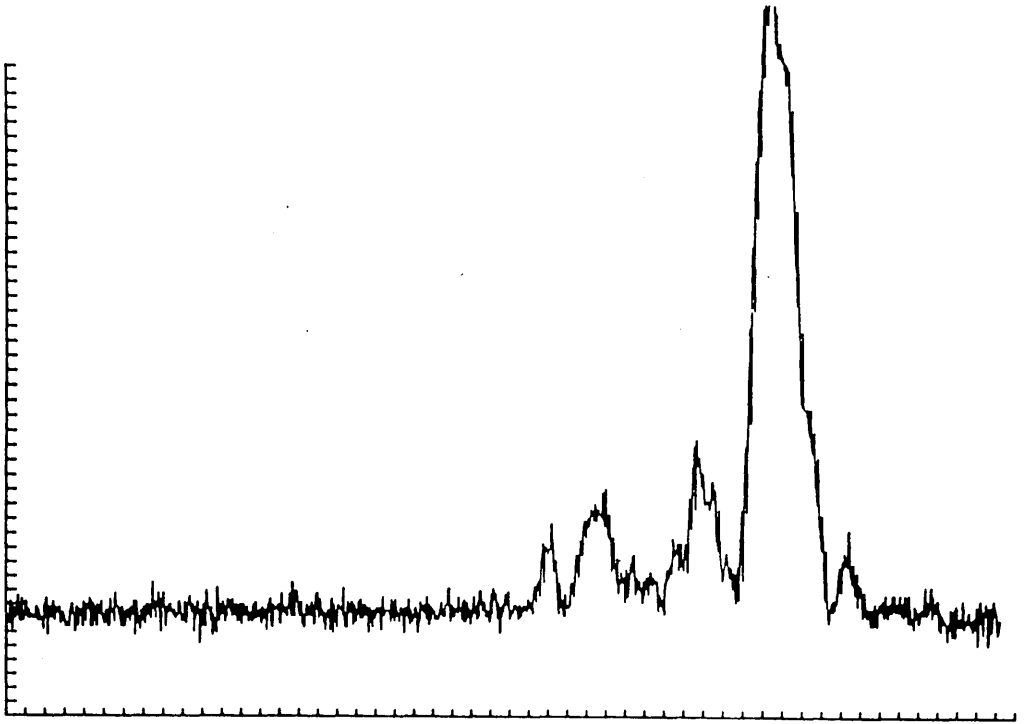


Fig. 5.7(e). Intensity profile through the guide and across the substrate 36 minutes after application of the biasing voltage.

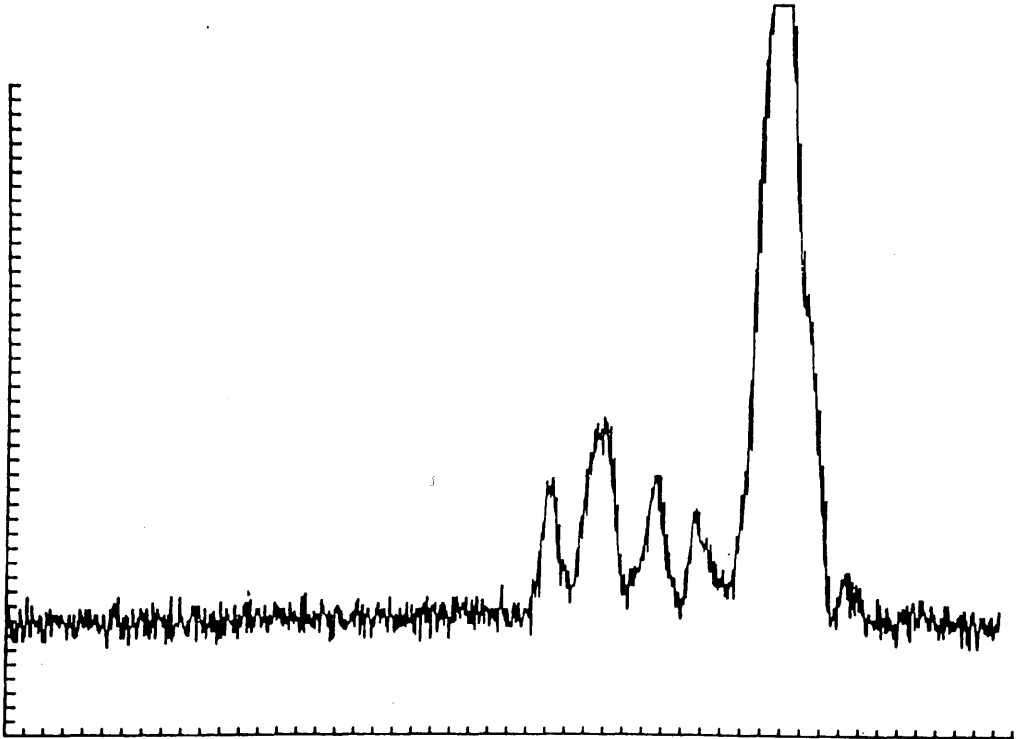


Fig. 5.7(f). Intensity profile through the guide and across the substrate 45 minutes after application of the biasing voltage.

an applied electrical field the photoexcited carriers (electrons) from the Fe^{2+} impurities in the LiNbO_3 sample will drift in the opposite direction to that of the applied field. This results in an internal field created in the opposite direction to the external field. If the direction of the optically induced electrical field created a negative change in the refractive index, the change may be large enough to destroy the guiding capabilities of the proton-exchanged region. The light would now no longer be supported in the exchanged region but instead be present in the substrate below. The optically induced charge distribution in the exchanged region would then relax in the absence of light while a similar charge distribution is created in the substrate below the guide. The light would then return to the guide where the optical induced charge distribution would again be created in the exchanged region while the charge distribution in the substrate would relax. If the creation of the charge distribution in the presence of light is faster than the relaxation of the charge distribution in the absence of light, the situation will eventually become stable with no further change in the distribution.

The above observations along with the measured restoration in the electrooptic coefficients appear to indicate that the hydrogen-bonded OH group is responsible for the previously reported instabilities and reduction in the electrooptic coefficients associated with proton-exchange. The reduction in the hydrogen-bonded OH group can be achieved both by annealing and by the use of dilute melt benzoic acid. Both the increase in the electrooptic coefficient and the reappearance of a stronger photorefractive effect can be attributed to a reduction in the ionic conductivity of the region.

Loni et al reported an absence of optical damage in planar guides fabricated using similar proton-exchange conditions. This could be explained by the use of lower optical power densities in the planar guides¹³, in comparison with those for the stripe guides reported here, since similar waveguide input power levels were used.

Due to a shortage of time available it was not possible to test the long term stability of the waveguides, which would require monitoring over a period of 12-24 months. The short term stability (variations over a period of minutes to hours) of the guides seemed to be mainly affected by the photorefractive effect. Effects due to protonic drifting may have been obscured by the photoconductive effect but, in the absence of an electrical bias across the waveguide, no stability problems other than those associated with the photovoltaic effect were observed.

References.

1. Royal Society Mathematical Tables 7, Bessel Functions (III): Zeros And Associated Values. University of Cambridge Press, 1960.
2. Weis R. S. and Gaylord T. K. "Lithium niobate: Summary of physical properties and crystal structure", *Appl. Phys. A* **37**. 1985 pp 191-203.
3. Jackel J. L. Rice C. E. and Veselka J. J. "Proton exchange for high-index waveguides in LiNbO₃." *Appl. Phys. Lett.* **41**. October 1982 pp 607-608.
4. Loni A., Hay G., De La Rue R. M. and Winfield J. M. "Proton-exchanged LiNbO₃ waveguides: The effects of post-exchange annealing and buffered melts as determined by infrared spectroscopy, optical waveguide measurements, and hydrogen isotopic exchange reactions." *J. Lightwave Tech.* **7**. June 1989. pp 911-919.
5. Yi-Yan A. "Index instabilities in proton-exchanged LiNbO₃ waveguides." *Appl. Phys. Lett.* **42**. April 1983. pp 633-635.
6. Wong K. K., De La Rue R. M. and Wright S. "Electro-optic-waveguide frequency translator in LiNbO₃ fabricated by proton exchange." *Optics Lett.* **7**. November 1982 pp 546-548.
7. Ashkin A., Boyd G. D., Dziedzic J. M., Smith R. G., Ballman A. A., Levinstein L., and Nassau K. "Optically-induced refractive index inhomogeneities in LiNbO₃ and LiTaO₃." *Appl. Phys. Lett.* **9**. July 1966. pp 72-74.
8. Schmidt R. V., Cross P. S. and Glass A. M. "Optically induced crosstalk in LiNbO₃ waveguide switches." *J. Appl. Phys.* **51**. January 1980. pp 90-93.
9. Becker R. A. "Methods of characterizing photorefractive susceptibility of LiNbO₃ Waveguides." *SPIE Proc.* **578**. 1985. pp 12-18.

10. Jackel J. L. "Short- term and long-term stability in proton exchanged lithium niobate waveguides", SPIE Proc. **460**. 1984 pp 43-48.
11. De Micheli M., Ostrowsky D. B., Barety J. P., Canali C., Carnera A., Mazzi G. and Papuchon M. "Crystalline and optical quality of proton exchanged waveguides", J. Lightwave Tech. **LT-4**. July 1986. pp 743-745.
12. Loni A., De La Rue R. M. and Winfield J. M. "Very low loss proton-exchange waveguides with a substantially restored electrooptic effect." Paper MD-3, Topical meeting on Integrated and guided wave optics, March 28-30, New Mexico, 1988, Opt. Soc. America (Washington).
13. Suchoski P. G., Findakly T. K. and Leonberger F. J. "Stable low-loss proton exchanged LiNbO₃ waveguide devices with no electrooptic degradation", Opt. Lett. **13**. November 1988. pp 1050-1052.

Chapter 6.

Summary, conclusions and future work.

6.1 Summary.

The basic crystal structure of lithium niobate in both its ferroelectric and paraelectric states has been reviewed. The properties of lithium niobate relating to the electrooptic effect have been discussed, in particular the crystal symmetry. A general introduction to the electrooptic effect and the dependence of the effective electrooptic coefficients on the symmetry class was presented.

An introduction to the concept of a transverse electrooptic phase modulator was presented. The reduction in the voltage required to induce a given phase-shift through the electrooptic effect for transverse electrodes, as compared with that for standard co-planar electrodes, was discussed. A review of some of the more important electrooptic modulators utilising co-planar electrodes that have been reported in the published literature and the possible benefits that may be gained by the use of transverse electrodes, including a substantial reduction in operating voltage, have been discussed.

The increase in the accuracy to which the electrooptic coefficient for a waveguide could be measured from the induced phase-shift for a known applied voltage using a transverse electrode structure on a thinned substrate was discussed. It was noted that the calculation of the overlap integral between the optical and electrical fields for co-planar electrodes could lead to errors in the measured electrooptic coefficients.

Various methods of achieving waveguides in lithium niobate have been reviewed, i.e. lithium oxide (Li_2O) outdiffusion, titanium-indiffusion, ion-implantation, proton-exchange and the growth of thin films of lithium niobate by R.F. sputtering and molecular beam epitaxy. The properties of the resulting waveguides and the problems associated with each method were discussed, in particular the stability problem of titanium-indiffused and proton-exchanged waveguides due to photorefractive effects.

It was mentioned that the problems traditionally associated with guides fabricated by proton-exchange, such as relaxation effects in the effective mode-

indices, high propagation losses and greatly reduced electrooptic coefficients have been substantially solved by the use of a fabrication technique developed at Glasgow University. A study of the electrooptic coefficients and the degree of restoration of the photorefractive effect associated with waveguides fabricated with the new technique was carried out later in the work for the thesis.

The method that was developed for the fabrication of the transverse electrooptic phase modulator was reported. This covered the fabrication procedures used for both titanium-indiffused and proton-exchanged waveguides and the technique used for the alignment of the electrodes. Various techniques used to deposit the silicon dioxide used for the buffer layer and the aluminium for the lower electrodes were discussed, the term "lower electrodes" refers to the electrodes which are located between the lithium niobate substrate and a glass supporting substrate.

The need for a supporting substrate to prevent the thinned lithium niobate substrate from breaking and the methods that have been attempted to bond the lithium niobate substrate to a glass supporting substrate were reported. The use of a conductive epoxy to bond the substrate to the sample was prevented by the outdiffusion of gases which created weak spots in the bonding layer and led to the sample cracking during thinning. The use of a two part epoxy proved better than a U.V. curing epoxy, which tended to expand excessively on heating. The requirement of a bond of uniform thickness between both substrates was discussed and the possible methods by which it might be achieved were investigated.

End-polishing to enable the efficient coupling of light into the guide by means of an end-fire rig was carried out after the sample had been bonded to the supporting substrate. A new method was reported that enabled the edges to be polished quickly and without the need for several different polishing and abrasive fluids. This method reduces the requirement for the sample and polishing machine to be cleaned thoroughly between each stage. The polished edges had to be protected during the thinning stage to prevent the edges from chipping. The use of quartz wax was found to give a nearly ideal means of achieving this protection.

The procedure, developed in conjunction with Logitech Ltd, that enabled the substrate to be thinned to less than 20 μm was reported. A thick glass plate

was used to hold the sample in position during thinning and was attached to the polishing jig by means of a vacuum chuck which enabled the thickness of the substrate to be checked periodically by means of a linear voltage differential transducer. A lapping rate of 20 μm per min was achieved, enabling the 1mm thick substrate to be thinned to below 100 μm in less than one hour, at which point the loading on the sample was reduced by a third to prevent cracking. Once the sample had been thinned to within +5 μm of the target thickness, the lapped surface was polished to remove all visible surface damage created by the lapping action.

The methods attempted to achieve contact to the lower electrodes have been described. The most successful method involved the use of a via hole, etched in the lithium niobate substrate by means of an abrasive etcher, to expose a contact pad on the lower surface of the lithium niobate substrate. Aluminium was evaporated to line the walls of the via hole, making contact to the lower electrodes, at the same time as the top electrodes were deposited.

The theoretical analysis of the transmission line properties of the transverse electrode structure by means of a conformal mapping technique was reported. This technique allows the accurate analysis of the capacitance, wave impedance and inductance on the basis of the electrode width and separation and the dielectric constant of the substrate. Equations were also presented that allow the synthesis of the required electrode width-separation ratio for a specific wave impedance and dielectric constant. A similar technique was reported for co-planar electrodes that allows the analysis of the wave impedance and capacitance for the electrode dimensions and the dielectric constant. A comparison between the transmission line properties, operating voltage, bandwidth, figure of merit and microwave properties for the transverse electrode structure and the co-planar electrode structure was made.

The various methods used to detect the electrooptically induced phase-shift were discussed. The use of an external Mach-Zehnder interferometer allowed the simple detection of the induced phase-shift from an applied d.c. voltage. Stability problems and a strong photorefractive effect observed in proton-exchanged waveguides indicated the use of a heterodyne system with an a.c. modulating field. The R_{33} and the R_{13} coefficients for titanium-indiffused waveguides were measured at 0.633 μm and 1.15 μm and the R_{33} coefficient for the proton-exchanged waveguides was measured at 0.633 μm . The values

reported showed a close match to previously reported values for both the titanium indiffused and the proton-exchanged waveguides at 0.633 μm and the values reported at 1.15 μm for the titanium-indiffused waveguides were in agreement with the trend expected from the values for other coefficients reported at longer wavelengths¹. The value reported for the proton-exchanged waveguides for the R_{33} coefficient showed a close match to previously reported values for a similar waveguide fabrication procedure². The operating voltages for the transverse electrooptic phase modulator with waveguides fabricated by titanium-indiffusion and proton-exchange were reported.

The capacitance of the transverse electrode structure was reported for various values of electrode separation. The bandwidth was calculated from the measured capacitance and compared with the bandwidth calculated from the theoretical capacitance. This enabled the figure of merit to be calculated from the operating voltage and the bandwidth to be calculated from the measured capacitance.

A restoration of the photorefractive effect in conjunction with the restoration of the electrooptic coefficients was reported. The restoration of both was attributed to a decrease in the conductivity of the proton-exchanged region, possibly due to a reduction in the concentration of hydrogen-bonded OH groups by annealing. Upon coupling light into the substrate, a rapid decrease in the intensity of the light in the guiding region was reported with a simultaneous increase in the intensity of light in the substrate below the guiding region. After approximately fifteen minutes the situation reversed itself and was followed by oscillations in the intensity of the light between the guide and the substrate, with the time taken for an oscillation increasing until after approximately one hour, the light had stabilised in the guide. The mechanics of the photorefractive effect were discussed and possible explanations of the restoration of the effect were given.

6.2 Conclusions.

From the results presented in chapter 5 the transverse electrooptic phase modulator has proved itself to be a potentially viable alternative to the more standard electrooptic modulator using co-planar electrodes and one with several important advantages. The increase in the electrooptic effect due to a uniform electric field distribution across the optical field distribution leads to a decrease in the operating voltage required for a specific electrooptically induced phase shift.

This voltage decrease gives the transverse electrooptic modulator an advantage where the application requires low power consumption. Although the capacitance for the transverse electrode structure is higher than that for a coplanar electrode structure of similar electrode dimensions, for high capacitances, as the value of the capacitance decreases, there is a more rapid decrease in the capacitance of the transverse electrode structure than for the coplanar electrode structure of similar electrode dimensions. Therefore, for situations where the electrodes are designed for a high bandwidth at the expense of the operating voltage, the transverse electrooptic modulator will have a lower operating voltage for a given bandwidth. The figure of merit is lower for the transverse electrooptic modulator over the complete range of electrode dimensions considered.

The use of the transverse electrooptic phase modulator to ascertain accurately the electrooptic coefficients of waveguides has been demonstrated. Although the fabrication of the transverse electrooptic modulator is more complicated and time consuming than that for a modulator using a coplanar electrode structure, the increase in accuracy attained should prove of sufficient worth for its use to be considered when any new waveguide fabrication technique or variations in the parameters of an existing technique is being investigated.

From the comparison between the measured capacitance in section 5.1 and the capacitance calculated from the theoretical equations presented in section 4.1.2 and 4.1.3, it can be concluded that the conformal mapping technique allows an accurate determination of the capacitance for a given dielectric constant and electrode dimensions. The conformal mapping technique should provide a similar accuracy for the calculation of the wave impedance but no measurements were made of the wave impedance of the fabricated devices, so a direct comparison has not been made.

The oscillations in the phase and the strong drifting in the optical mode profile that were observed during the measurements of the electrooptic coefficients of proton-exchanged waveguides using the Mach-Zehnder interferometer were attributed to the photorefractive effect. The nature of the oscillations, along with the expectation of a reduction in the concentration of the hydrogen-bonded OH group, implied that the photorefractive effect was a more likely explanation than the ionic drifting normally observed in proton-exchanged waveguides. One possible explanation for the reappearance of both effects would

be a decrease in the conductivity of the exchanged region, due to the reduction in the concentration of the hydrogen-bonded OH groups, increasing both the effect of the external applied field and hence the electrooptically induced phase shift and the internally induced electric field created from the optically induced charge separation through the photorefractive effect. If, as described, the return of the photorefractive effect is associated with the same change in the crystal structure as is responsible for the restoration of the electrooptic coefficients, one of the major benefits of proton-exchanged waveguides will be lost.

6.3 Future work.

Possible extensions of the work carried out in this thesis can be split into two broad areas: firstly the benefits described in this thesis for a modulator using a transverse electrode structure as opposed to the more standard co-planar electrode structure and secondly the use of the transverse electrooptic phase modulator to study waveguide fabrication techniques, in particular the method of proton-exchange described in this thesis.

Looking at the first area of possible work, the design and construction of a transverse electrooptic modulator with narrower electrodes designed for high frequency (> 1 GHz) operation should be considered as well as the continued study of the thinning process to enable the substrate to be reduced to $10\ \mu\text{m}$ or less. In addition, a more detailed study of the use of a transverse electrode structure in alternative modulator and other device designs to the simple phase modulator fabricated in the thesis may show the largest improvements over the co-planar electrode structure. In particular, the use of a transverse electrode structure to fabricate a travelling wave modulator should allow the bandwidth to be increased beyond the maximum bandwidth achieved to date, while the characteristic impedance of the electrode structure can readily be matched to $50\ \Omega$, making it ideal for use in a standing wave modulator. A recent proposal for a travelling wave modulator suggested the use of a ridge waveguide with the electrode gap partially filled by air³. This has the effect of reducing the effective dielectric constant and the velocity mismatch between the optical and electrical fields and hence increasing the bandwidth. The suggested design is likely to be hard to fabricate and the idea for velocity matching may be more readily realisable by transverse electrodes in conjunction with an additional material, with a lower dielectric constant, sandwiched between the electrodes alongside the waveguide. A possible design realisation for this is shown in Fig 6.1.

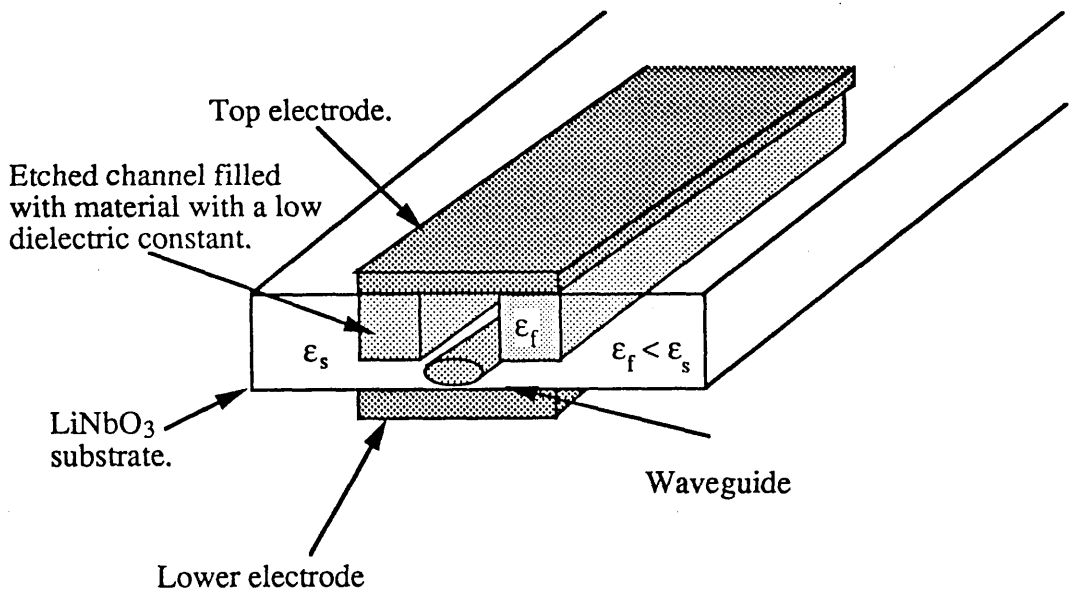


Fig. 6.1. Possible high bandwidth travelling wave electrooptic modulator using a material with a low dielectric constant to reduce the effective dielectric constant.

A thinner substrate which will provide a lower operating voltage, regardless of the modulator type, may be achieved by the lapping and polishing techniques described in chapter 3, followed by ion-beam milling to remove an extra 5-10 μm of substrate above the waveguide, see Fig. 6.2. This would combine the speed of thinning achieved by mechanical lapping with the localised etching and control of etch rate characteristic of ion-beam milling. In addition, the probability of the sample cracking during polishing will inevitably increase as the substrate thickness decreases.

Future work on the proton-exchanged waveguides should employ the transverse electrode structure to study not only possible further improvements in the electrooptic coefficients, but also the reappearance of the photorefractive effect. During the oscillations in the optical mode profile associated with the photorefractive effect, the thinned substrate confined the light to the region just below the waveguide and aided the interpretation of what was happening in the guiding region.

The transverse electrodes structure has demonstrated its potential as an alternative to the more standard co-planar electrodes for use in electrooptic modulators. In addition the use of transverse electrodes enables a more accurate estimate of the electrooptic coefficients for waveguides fabricated by novel techniques.

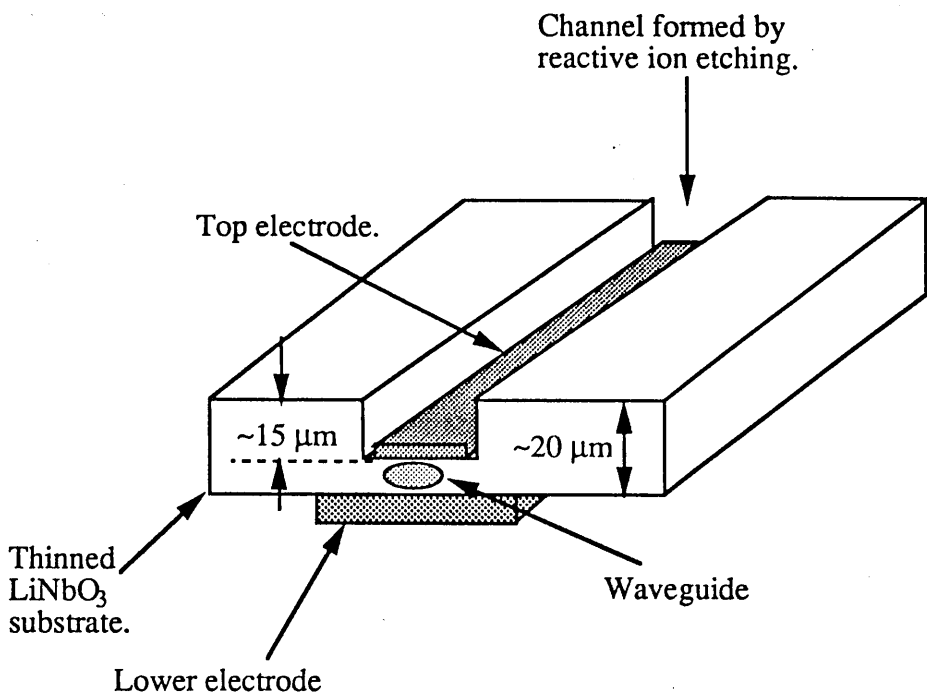


Fig. 6.2. The use of reactive ion-beam etching following thinning the substrate by mechanical lapping to achieve a thinner electrode gap.

References.

1. Weis R. S. and Gaylord T. K. "Lithium niobate: Summary of physical properties and crystal structure", Appl. Phys. A 37. 1985 pp 191-203.
2. Loni A., De La Rue R. M. and Winfield J. M. "Very low loss proton-exchange waveguides with a substantially restored electrooptic effect." Paper MD-3, Topical meeting on Integrated and guided wave optics, March 28-30, New Mexico, 1988, Opt. Soc. America (Washington).
3. Minakata M. et al. "Design of a broad-band travelling wave optical modulator based on velocity matching", Second Optoelectronics Conference (OEC '88) 3C. October 1988 pp 164-165.

Appendix A.

Evaluation of the transmission line properties of strips separated by a dielectric sheet by the use of conformal mapping.

The use of the conformal mapping technique to establish a relationship between the transmission line properties of metal strips separated by a dielectric sheet and the strip dimensions and the dielectric constant of the sheet was explained in chapter 4. Since the explanation given in chapter 4 tried to be as non-technical as possible, a more detailed examination of the actual mapping and subsequent derivation presented by Wheeler¹ is given below. This is presented mainly for clarification of the explanation given in chapter 4. For a full explanation of the mapping procedure, the reader's attention is drawn to an earlier paper by Wheeler which describes the conformal mapping technique to evaluate the field configuration of strips in a wave medium of uniform properties².

To establish the transmission line properties a relationship between the structural properties and electrical properties is required. The most significant electrical property of the strips is the wave impedance from which the other properties can easily be derived. The most significant structural property is the shape ratio, defined as the ratio of strip width to separation. The cross section of the transmission line, two parallel strips on opposite faces of a dielectric sheet, is shown in Fig. 4.2. The width of the strip is a , the separation is b and the dielectric constant of the sheet is ϵ_r . The conductors forming the strip lines are assumed to be thin sheets of a perfectly conductive material.

A.1 Conformal mapping techniques.

The top left quadrant of the transmission line cross section is shown in Fig. 4.3 on the z -plane ($z=x+jy$). The wave impedance of this quadrant is the same as that of the pair of strips. The critical points in the z -plane for mapping are marked 1–8. The heavy solid lines represent the conductors and the heavy dotted lines represent the electric flux-bisection boundaries. The light dotted lines represent the flux lines that would be present off the edge of the strip if the surrounding medium were free space. The dielectric to the left of this line,

represented by the shaded area, will cause a distortion of the flux lines. It is important to note that the separation is made equal to π for ease of derivation.

By using the mapping procedure described in reference 2, the conductor boundaries are mapped onto the $z'=x'+jy'$ plane, shown in Fig. 4.4, where x' is the flux coordinates and y' is the potential coordinates. The numbered points in the z' plane correspond to those in the z plane and so it can be seen that the boundary of the dielectric is mapped as a curve in the z' plane between points 3 and 8. The potential along the conductor boundary is zero, so points 2,3 and 4 all lie along the x -axis. The problem is now reduced to one of a mixed dielectric in the gap between parallel planes of infinite extent. The area to the left of the curve represents the dielectric sheet region, while the area to the right represents the region outside the dielectric sheet. An effective dielectric constant for the entire region will be evaluated which is a weighted mean between the dielectric constant for the sheet and free space. The conformal mapping technique maintains the angle of refraction at the boundary between the dielectric sheet and free space.

Depending on the shape ratio and dielectric constant of the structure several approximations are required. The shape ratio can be divided into five categories.

Very narrow:	$a/b \ll 1$
Narrow:	$a/b < 1$
Square:	$a/b = 1$
Wide:	$a/b > 1$
Very wide:	$a/b \gg 1$

For the two extremes of the shape ratio the effective relative dielectric, ϵ_{re} constant can be simplified as follows,

Very wide:	$\epsilon_{re} = \epsilon_r$
Very narrow:	$\epsilon_{re} = \frac{\epsilon_r + 1}{2}$

The first approximation is valid since, for $a/b \gg 1$, nearly all the flux is in the dielectric. The second approximation is valid since the electric field is symmetrically concentrated near the strip with free space on one side and the dielectric on the other side. The shape ratio of concern to our problem lies

between these two extremes, on either side of the square condition. It is, however, necessary to derive the situation for the extremes of the shape ratio and interpolate for intermediate conditions in order to avoid extensive computation.

At this point it is helpful to introduce another parameter, the partial filling fraction q which is mainly dependent on the shape ratio. The filling fraction can be defined as the ratio of the dielectric area over the total area below $b=\pi$ in Fig. 4.4. The lower value of q is defined as q'' and the upper value as q' .

Conformal mapping techniques limit the solution of the transmission line problem to one where the dielectric boundaries are all located along either flux lines or potential contours. Therefore on the z' plane every dielectric boundary would be parallel to one axis or the other. As can be seen from Fig. 4.4 the dielectric boundary forms a curve between points 3 and 8, meeting neither of the above boundary conditions. It is possible however to express the boundary as a mixture of the two conditions.

The area between a' and g' is completely filled with dielectric. The area to the left of a' is mainly filled with free space except the shaded area to the right of the dielectric boundary. It is this area that defies exact analysis by the conformal mapping technique, since the boundary is curved. By dividing the shaded area into two rectangles we can obtain an approximate solution. This splits the boundary into two lines, one parallel to the flux axis and one parallel to the potential axis, as shown in Fig. 4.5. The magnitude of the entire shaded area is expressed as $\pi s'$, where s' is the effective width along the x' axis. The rectangle parallel to the potential boundary has an area $\pi s''$ adding s'' to the area right of a' . This area is termed the parallel component. The rectangle parallel to the flux axis has an area $\pi(s''-s')$, and is effectively in series with the free-space region outside the dielectric. By replacing the curved boundary a close approximation of the shaded area is achieved, which is a small part of the total effect of the dielectric, which conforms to the requirements of conformal mapping.

The effective width of the shaded area, s , lies between the two bounds, s' and s'' . The effect of the shaded areas in Fig. 4.5 can be thought of in terms of dielectric and air capacitors in series and parallel connection. It is therefore possible to obtain a first approximation for the shaded area and the effective width from :

$$s = s'' + \frac{s' - s''}{\epsilon_r} = \frac{1}{\epsilon_r} s' + \frac{\epsilon_r - 1}{\epsilon_r} s''$$

The actual filling fraction q' is formulated in terms of the effective width

$$q' = \frac{g' - a' + s'}{g'} = 1 - \frac{a' - s'}{g'} = 1 - \frac{a'}{g'} \left(1 - \frac{s'}{a'}\right) \quad (\text{A-1})$$

This expression includes all of the area filled with the dielectric. The parallel part of the filling fraction, q'' , is evaluated from the dielectric to the right of a' and the parallel part of the curved area of dielectric to the left of a' .

$$q'' = \frac{g' - a' + s''}{g'} = q' - \frac{s' - s''}{g''} \quad (\text{A-2})$$

Similarly the effective filling fraction can be found from

$$q' = \frac{g' - a' + s}{g'} = q'' - \frac{s' - s''}{g'} \quad (\text{A-3})$$

From the concept of parallel capacitors, the effective dielectric constant is related to the effective filling fraction by

$$q' = \frac{\epsilon_{re} - 1}{\epsilon_r - 1} \quad (\text{A-4})$$

$$\epsilon_{re} = 1 + q(\epsilon_r - 1) \quad (\text{A-5})$$

It is useful at this point to state the concepts which are valid for the extremes of the dielectric constant. For a dielectric with a low value of dielectric constant, the dielectric causes no appreciable distortion of field, producing only a small effect on the electric field proportional to $(\epsilon_r - 1)$. For a high value of dielectric constant there is no appreciable energy outside the dielectric, as shown in Fig. A.1, so that the flux boundary, represented by a dashed line, and the dielectric boundary coincide. This situation is equivalent to adding a second neutral plane above the strip. The effective width of one quadrant of Fig. A.1 is

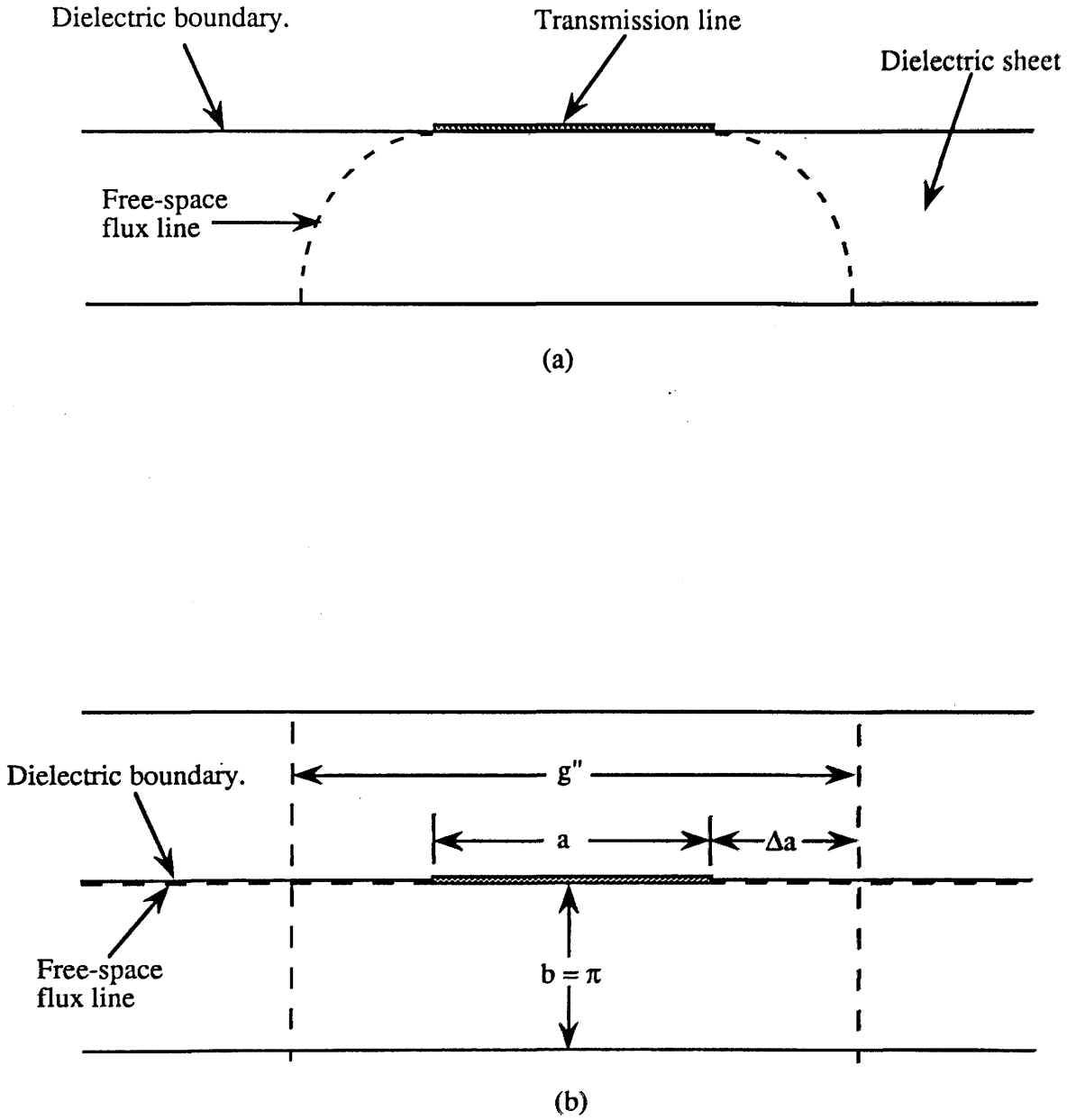


Fig. A-1. Comparison of dielectric sheet boundary and free-space flux line between (a) a transmission line and (b) a strip between parallel planes.

half filled with the dielectric so the effective width of the dielectric filling is $g''/2$. Therefore only the parallel part of the dielectric area is effective and can be defined and computed by conformal mapping. For this case the lower bound of the effective filling fraction as shown in Fig. A.1 is

$$q'' = \frac{1}{2} \frac{g''}{g'} > \frac{1}{2} \quad (\text{A-6})$$

This concept will be used later in the derivation of wide strips.

Returning to the principal problem, that of evaluating the shaded area outside of the curve in Fig. 4.4, there is one more parameter which must be introduced. This is the effective area fraction and is defined as the effective area of dielectric to the left of a' over the total area to the left of a' , s/a' . By plotting the effective area fraction against the shape ratio, it can be seen from Fig. A.2 that the effective area fraction has a maximum for the square shape and decreases to zero for both shape extremes. The effective area fraction lies between two bounds, the lower bound s''/a' corresponding to a high ϵ and represents the parallel component of the area fraction and the upper bound s'/a' , the actual area fraction, corresponding to $\epsilon_r=1$, and having a maximum value of $1-\pi/4$. The effective area fraction is a weighted mean between the graphs for these bounds with the weighting dependent upon the dielectric constant.

In developing mathematical approximations for the entire range of the shape ratio, it is helpful to work from the extremes of the shape ratio to more elaborate formulae for the intermediate values.

A-2 Wide strip derivation.

The free-space impedance R_1 , the inductance L and the free space capacitance C_1 for a pair of wide strips in free space, i.e not separated by a dielectric, can be related to the effective half width g' on the x' plane by

$$R_1 = \frac{R_c \pi}{g'}; \quad g' = \frac{\pi R_c}{R_1} \quad (\text{A-7.a})$$

$$C_1 = \frac{\epsilon_0' g'}{\pi}; \quad g' = \frac{\pi C_1}{\epsilon_0'} \quad (\text{A-7.b})$$

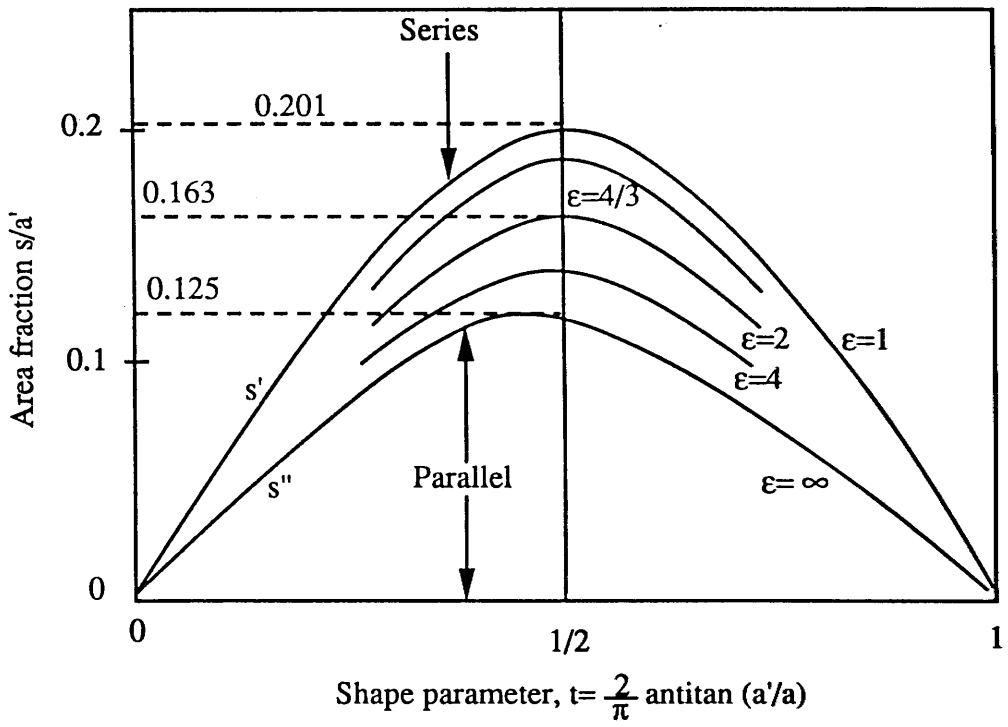


Fig. A-2. Variation of extra area with shape.

$$L = \frac{\mu_0 l \pi}{g'}; \quad g' = \frac{\pi \mu_0 l}{L} \quad (\text{A-7.c})$$

where R_c is the wave impedance of a unit square area of free space, 377Ω , l is the strip length, ϵ_0 is the permittivity of free space and μ_0 is the permeability of free space.

In the problem of a mixed dielectric, the free-space impedance and free-space capacitance are dependent upon the effective dielectric constant ϵ_{re} of the entire space surrounding the strips. The inductance is not dependent upon the surrounding medium because of magnetic uniformity. The resulting values of resistance and capacitance are

$$R = \frac{1}{\sqrt{\epsilon_{re}}} R_1; \quad C = \epsilon_{re} C_1 \quad (\text{A-8})$$

The wave velocity is also reduced by the same ratio as the resistance.

The marginal condition for wide strips, $a/b=1$, corresponds roughly to $R=R_c/2\sqrt{\epsilon'}$ for which $g'=2\pi$. For wider strips, $g'=\pi$ may be taken as the extreme condition.

Using the conformal mapping formulas given by Wheeler² for the relation between the space coordinates on the z -plane and the flux potential coordinates on the z' -plane and the conditions described above, the following formulae can be derived. It should be noted that Wheeler uses a parameter d which is described on the collinear boundary coordinate plane. This is nearly equal to the effective width g' and therefore g' and d have been interchanged in the formulae taken from Wheeler's description of parallel strips surrounded by free space. This interchange is valid for all except the closest approximations where the small difference between the two parameters may be included as $(d-g')$.

The line between the points 3 and 7 represents the free space flux line that would terminate on the edge of the strip if the dielectric sheet were not present. The flux along this line is constant and it is therefore mapped as a straight line of constant flux as shown in Fig. 4.4. The flux and potential are not constant along the boundary of the dielectric sheet between points 3 and 8 and the boundary is therefore mapped as a curve on the z' plane. The evaluation of the area on the z'

plane between the curve marked by points 3 and 8, the straight line marked by points 3 and 7 and the $y'=\pi$ boundary is the principle objective of the conformal mapping procedure used.

The mapping between the z -plane and the z' -plane can be described by

$$z = x + jy = j\pi + g' \tanh \frac{1}{2}z' - z' \quad (\text{A-9})$$

The imaginary part of Eq. (A-9) at the dielectric boundary, $x=0$ and $y=\pi$, determines a curve on the z' -plane representing the dielectric boundary :

$$y = \pi = \pi + g' \frac{\tan \frac{1}{2}y' (1 - \tanh^2 \frac{1}{2}x')}{1 + \tan^2 \frac{1}{2}y' \tanh^2 \frac{1}{2}x'} \quad (\text{A-10.a})$$

Eq.(A-10.a) can reduced so that x' can be expressed explicitly in terms of y'

$$\cosh x' = g' \frac{\sin y'}{y'} - \cos y' \quad (\text{A-10.b})$$

where for large x'

$$x' = \ln 2 \left(g' \frac{\sin y'}{y'} - \cos y' \right) \quad (\text{A-11})$$

From the transformations defined by Wheeler¹, the effective half width of the outer face of the strip, a' , can be expressed in terms of g' , the effective width of the strip including outer and inner faces.

$$a' = \ln 2 (g' - 1) \quad (\text{A-12})$$

The shaded area in Fig. 4.5 approaches a limit as g' increases, corresponding to the case for very wide strips., and gives :

$$a' - x' = \ln \left[\frac{\frac{\sin y'}{y'} - \frac{\cos y'}{g'}}{1 - \frac{1}{g'}} \right] = \ln \frac{\sin y'}{y'}, (g' \rightarrow \infty) \quad (\text{A-13})$$

The maximum for s' is found by integrating over the entire curve of Eq. (A-13).

$$\max s' = \frac{1}{\pi} \int_0^{\pi} \left(\ln \frac{\sin y'}{y'} \right) dy' = 0.903 \quad (\text{A-14})$$

The expression of Eq. (A-14) gives the value of the increment in the effective half width for the extreme case of very wide strips. It is now necessary to find an equation which will describe the increment in the effective half width for the intermediate range of wide strips. The dielectric boundary curve described in Eq. (A-10.b) can be approximated by an elliptic quadrant inscribed in the rectangle formed by $x'=a'$ and $y'=\pi$. The dimensions of the ellipse are chosen so that the ellipse crosses the boundary curve at the intersection with the diagonal of the ellipse. The area outside the ellipse is taken as an approximation of the area outside of the curve. The resulting effective width can be expressed in terms of a' :

$$s' = 0.732 [a' - \text{anti cosh} (0.358 \cosh a' + 0.953)] \quad (\text{A-15})$$

Comparing Eq. (A-15) for the very wide case with Eq. (A-14), a measure of the closeness of the approximation over the entire range is obtained.

$$(\text{A-15}) \quad \max s' = 0.732 \ln \frac{1}{0.358} = 0.752$$

$$(\text{A-14}) \quad \max s' = 2 \ln \frac{\pi}{2} = 0.903$$

Eq. (A-13) is more than 80% of the correct value for very wide strips, indicating that for the intermediate range including the square shape it will provide a very close approximation. Therefore Eq. (A-15) approximates the effective width in the intermediate range, while Eq. (A-14) approximates the effective width in the very wide range.

The area fraction, s'/a' , is found to have a maximum value near the square condition. From Eq. (A-15) this is found to be 0.201, which is only slightly less than the value of $1-\pi/4$ defined previously.

Having evaluated the effective width we can now look at the parallel component of the effective width, s'' . This is derived by considering the case for high ϵ_r where all the flux is in the dielectric. In this case, the effective half-width, $1/2.g''$, exceeds the actual half-width by Δa and Δa approaches a limit very rapidly as the shape ratio approaches and exceeds unity. The limiting value of Δa for very wide strips is 1.386, i.e.:

$$\Delta a = \frac{1}{2}g'' - a = 1.386 \quad (\text{A-16})$$

Referring to Fig. 4.5 the effective half-width is $g'-a'$. For a dielectric with a high dielectric constant, ϵ_r , as shown in figure 4.5, the effective half-width is modified to $1/2.g''$. The excess of the latter over the former corresponds to the parallel component of the effective width.

$$s'' = \frac{1}{2}g'' - (g' - a') = \left(\frac{1}{2}g'' - a \right) - (g' - a' - a) \quad (\text{A-17})$$

Substituting the following equations into Eq. (A-17), s'' can be expressed in terms of g' . Eq. (A-18) is derived from Wheeler².

$$a' = \ln 2 (g' - 1) \quad (\text{A-12})$$

$$\frac{1}{2}g'' - a = 1.386 \quad (\text{A-16})$$

$$a = (g' - 1) - \exp - a' - a' \quad (\text{A-18})$$

$$s'' = 0.386 - \frac{1}{2(g' - 1)} \quad (\text{A-19})$$

In the limit for very wide strips, the maximum value of the parallel component of the effective width, s'' , contributes less than half of the total effective width, s' , i.e.:

$$\max s'' = 0.386$$

$$\frac{\max s''}{\max s'} = \frac{0.386}{0.903} = 0.427$$

The parallel component of the area fraction, s''/a' , can be found from Eq. (A-19) for the complete range of wide strips. It has a maximum value of 0.125 near the square shape ratio, greater than one half of the total area fraction.

We can now find the serial component, $(s'-s'')/a'$, of the area fraction from the total and parallel components for the whole range of shapes.

From Wheeler², the effective half width of the strip, g' , is

$$g' = a + 1 + \ln 2\pi \left(\frac{a}{\pi} + 0.94 \right) \quad (\text{A-20})$$

This concludes the mapping operations required to find the effective dielectric constant, ϵ_{re} , for wide strips. For a given shape ratio, g' , can be calculated from Eq. (A-20); the effective half-width of the outer strip face, a' , can be calculated from Eq. (A-12); the increment in the effective width due to the presence of the dielectric sheet, s' , can be calculated from Eq. (A-15); the parallel component of s' , s'' , can be calculated from Eq.(A-17); the effective filling fraction, q , can be calculated from Eq. (A-3) and the effective dielectric constant, ϵ_{re} , can be calculated from Eq. (A-5). From Eq. (A-7) an explicit formula can be obtained for the analysis of the wave resistance in terms of the shape ratio. Since, at the beginning, the separation, b , was set to π and, hence, the shape ratio to a/π , the half width a , must be replaced by $a\pi/b$. Therefore :

$$\frac{R}{R_c} = \frac{\sqrt{\frac{1}{\epsilon_r}}}{\frac{a}{b} + \frac{1}{\pi} \ln 4 + \frac{\epsilon_r + 1}{2\pi \epsilon_r} \left[\ln \left(\frac{a}{b} + 0.94 \right) + 1.451 \right] + \frac{\epsilon_r - 1}{2\pi \epsilon_r^2} (0.082)} \quad (\text{A-21})$$

where R_c is the impedance of free-space wave, $120\pi \Omega$, and R is the wave impedance of the transmission line.

From Wheeler¹ the formula for synthesis is shown to be

$$\frac{a}{b} = \frac{1}{\pi}(g_{\epsilon} - 1) - \frac{1}{\pi} \ln(2g_{\epsilon} - 1) + \frac{k-1}{2\pi\epsilon_r} \left[\ln(g_{\epsilon} - 1) + 0.293 - \frac{0.517}{\epsilon_r} \right] \quad (\text{A-22})$$

where g_{ϵ} is the smaller value of the effective half-width that would be required if the space were entirely filled with the dielectric material.

$$g_{\epsilon} = \frac{\pi}{\sqrt{\epsilon_r}} \frac{R_c}{R}$$

A-3 Narrow strip derivation.

A similar approach is used for the analysis of narrow strips based on free-space formulas and the principles stated for the wide strips. It is useful to introduce some new parameters more relevant to the narrow strip case. The width parameter g is replaced by a separation parameter h . For narrow strips surrounded by free-space :

$$R_1 = R_c \frac{h'}{\pi}, \quad h' = \frac{\pi R_1}{R_c} = \frac{\pi^2}{g'} \quad (\text{A-23})$$

The average of the free-space and the separating sheet dielectric constants is ϵ_a :

$$\epsilon_a = \frac{\epsilon_r + 1}{2} \quad (\text{A-24})$$

If the space were filled completely with ϵ_a , the wave impedance R of the strip lines would be :

$$R = R_c \frac{h_a}{\pi \sqrt{\epsilon_a}} \quad (\text{A-25})$$

The free-space wave resistance for narrow strips is given, to a second approximation, by :

$$h' = \frac{\pi R_1}{R_c} = \ln \frac{4b}{a} + \frac{1}{8} \left(\frac{a}{b} \right)^2 \pm (\dots) \left(\frac{a}{b} \right)^4 \pm \dots \quad (\text{A-26})$$

This may be derived by substituting for each each strip a spaced pair of round wires, which is equivalent in the second-order far field.

$$\frac{b}{a} = \frac{1}{4} \exp (h') - \frac{1}{2} \exp (-h') \quad (\text{A-27})$$

The condition for narrow strips near to a square shape corresponds roughly to $R=R_c/\sqrt{k'}$ for which $h'=\pi/2$. In Fig. 4.3 the free-space flux line between points 3 and 7, the line which would terminate on the edge of the strip if the dielectric were not present, approaches the shape of a circular arc. Due to the presence of the dielectric, most of the energy is concentrated close to the strip and divided nearly equally between the inner and outer strip faces. For very narrow strips, the effective dielectric constant therefore approaches the lower limit :

$$\epsilon_{re} = \epsilon_a = \frac{\epsilon_r + 1}{2} \quad (\text{A-28})$$

The excess of ϵ_{re} over ϵ_a is caused by the shaded area in Fig. 4.3 and increases with the shape ratio. The total filling fraction, q' , and width parameter, g'' , have been shown by Wheeler² to be :

$$q' = \frac{1}{2} + \frac{\ln 2}{2\pi^2} g' = \frac{1}{2} + \frac{\ln 2}{2g'} \quad (\text{A-29})$$

and

$$g'' = g' + \frac{\ln \frac{\pi}{2}}{\pi^2} g'^2 \quad (\text{A-30})$$

From these expressions the parallel component of the filling fraction can be shown to be:

$$q'' = \frac{1}{2} \frac{g''}{g'} = \frac{1}{2} + \frac{\ln \frac{\pi}{2}}{2h'} \quad (\text{A-31})$$

The series component of the filling fraction is the difference between the parallel component of the filling fraction and the total filling fraction.

$$q' - q'' = \frac{\ln \frac{4}{\pi}}{2h'} \quad (\text{A-32})$$

The effective filling fraction can therefore be found from A-3

$$q = \frac{1}{2} + \frac{1}{2h'} \left(\ln \frac{\pi}{2} + \frac{1}{\epsilon_r} \ln \frac{4}{\pi} \right) \quad (\text{A-33})$$

From A-5 the effective dielectric constant is :

$$\epsilon_{re} = \frac{\epsilon_r + 1}{2} + \frac{(\epsilon_r - 1)}{2h'} \left(\ln \frac{\pi}{2} + \frac{1}{\epsilon_r} \ln \frac{4}{\pi} \right) \quad (\text{A-34})$$

The separation parameter may be expressed in terms of h_a :

$$h' = h_a + \frac{1}{2} \frac{(\epsilon_r - 1)}{(\epsilon_r + 1)} \left(\ln \frac{\pi}{2} + \frac{1}{\epsilon_r} \ln \frac{4}{\pi} \right) \quad (\text{A-35})$$

This allows the shape ratio to be determined for a specified wave resistance and dielectric constant. If the shape ratio is less than 1, the estimated error is less than 0.005.

For analysis, a second approximate formula for narrow strips can be shown to be

$$\frac{R}{R_c} = \frac{1}{\sqrt{\epsilon_a}} \frac{1}{\pi} \left[\ln \frac{4b}{a} + \frac{1}{8} \left(\frac{a}{b} \right)^2 - \frac{1}{2} \frac{\epsilon_r - 1}{\epsilon_r + 1} \left(\ln \frac{\pi}{2} + \frac{1}{\epsilon_r} \ln \frac{4}{\pi} \right) \right] \quad (\text{A-36})$$

The estimated relative error is less than 0.001 for all conditions of narrow strips.

References.

1. Wheeler H. A., "Transmission-line properties of parallel strips separated by a dielectric sheet." IEEE Trans. Microwave Theory Tech. **MTT-13**, 1965, pp 172-185.
2. Wheeler H. A., "Transmission-line properties of parallel wide strips by a conformal-mapping approximation." IEEE Trans. Microwave Theory Tech. **MTT-12**, 1964, pp 280-289.

Publications.

S. McMeekin and R. M. De La Rue, "Novel transverse electro-optic waveguide phase modulator realised in titanium-diffused and proton-exchanged LiNbO₃". Elec. Lett. **25**(13), June 1989, pp 853-854.

S. McMeekin and R. M. De La Rue, "A transverse electro-optic phase modulator". 5 th European Conference on Integrated Optics, Paris, April 1989.

S. McMeekin and R. M. De La Rue, " A transverse electrooptic phase modulator". SPIE Proc. **1141**, paper 41, 1989.

